Use of Uranium Decay Series
for Dating an Archaeological Smelting Site

by

Violetta Wolf

Submitted to the Department of Materials
Science and Engineering in Partial
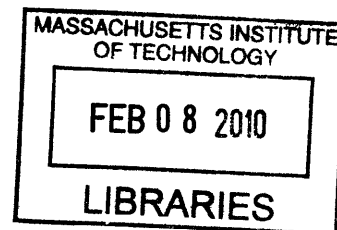Fulfillment of the Requirements for the
Degree of

Bachelor of Science

at the

Massachusetts Institute of Technology

June 2008

Signature of Author ....
Department of Materials Science and Engineering
May 19, 2008

Certified by ....
Dorothy Hosler
Professor of Archaeology and Ancient Technology
Thesis Advisor

Accepted by ....
Caroline A. Ross
Professor of Materials Science and Engineering
Chairman, Undergraduate Thesis Committee

Use of Uranium Decay Series
for Dating an Archaeological Smelting Site

by

Violetta Wolf

Submitted to the Department of Materials
Science and Engineering on May 19, 2008
in Partial Fulfillment of the Requirements
for the Degree of Bachelor of Science
in Archaeology and Materials

ABSTRACT

Through the identification of phases and their isotopic composition and variability, an assessment of the applicability of uranium decay series dating to El Manchon slags was made. El Manchon is the only Mesoamerican site to exhibit smelting technology. Uranium series dating is typically used on geologically old natural material, but the El Manchon slags were not suitable for other dating techniques. There are four requirements of uranium series dating: measurable presence of appropriate isotopes, cogenetic phases within the material, isotopic fractionation between phases, and the ability to physically separate the phases. This is the first attempt to date archaeological material with the uranium series dating method.

Petrographic reflected light microscopy was used to identify the phases in the slags. Electron beam microanalysis was used to identify the chemical composition of the identified phases. Ion beam microanalysis was used to assess the isotopic fractionation between the phases. Electron pulse disaggregation, hand-sorting, and magnetic separations were performed to separate the phases.

The slags are composed of four different phases: a silica-melt phase, a quartz-like phase, a copper phase, and a copper-iron-sulfide phase. These four phases are in abundant presence with sufficient isotopic fractionation to make the El Manchon slags suitable for uranium series dating.

Thesis Advisor: Dorothy Hosler
Title: Professor of Archaeology and Ancient Technology

Index of Tables

Index of Figures

7

Introduction

Problem Statement

My research goal is to determine if copper smelting slags from the archaeological site of El Manchon, Guerrero, Mexico are suitable for uranium series dating through isotopic and microstructural analysis. Uranium series dating is a radiometric dating method common to geochemistry. This research is the first application of this technique to archaeological material, specifically archaeological slags.

Uranium series dating of a material requires the presence in the material of uranium series isotopes, the existence of cogenetic phases in the material, isotopic fractionation between the cogenetic phases, and methods to separate the phases physically. These four criteria can be assessed only by rigorous chemical and physical analysis through use of techniques from materials science and geochemistry. Geologists use the uranium series dating method to date carbonates and lavas, but these materials are completely dissimilar to slags. Accurate dates of the El Manchon smelting slags will provide fundamental data by which to establish the chronology of Mesoamerican extractive metallurgy. If such dates can be acquired through uranium series dating, archaeology will be provided with a new method for dating slags, worldwide.

El Manchon is the only known site in Mesoamerica with evidence of ancient copper smelting. Professor Dorothy Hosler discovered the site in 1998 (Hosler 2003b, 2004) during her survey of the Balsas River drainage to locate preHispanic copper smelting sites. While there is clear archaeological evidence of metallurgical activities in preHispanic Mesoamerica (Hosler 1988a, 1988b, 1994, 2003a), the Spaniards and other Europeans also carried out smelting operations in the New World after the invasion of Mexico in 1521 (Hosler, personal communication, April 2008). Because El Manchon is a unique example of a physically discrete copper smelting

facility within a larger archaeological site, it is essential that evidence of the smelting technology be dated directly, rather than in association with other materials at the site.

Radiocarbon dates from the habitation areas at El Manchon agree with the chronology suggested by pottery types recovered from the site, these dates range from 1350 CE to 1550 CE[1.] (Hosler 2003b, 2004). Wood and charcoal samples from test pits and horizontal excavations in the habitation areas of the site were used to determine these carbon-14 dates. The pottery found in the habitation area is of the Yestla Naranjo type, dating to the middle Postclassic period (approximately 1300 CE). The organic material found in the smelting area has produced ambiguous and unreliable accelerated mass spectrometry (AMS) carbon-14 dates between 750 CE and 1850 CE (Hosler 2003b, 2004).

The carbon-14 dates from the smelting area of El Manchon, on average, appear to be several hundreds of years older than the carbon-14 dates from the habitation area (Hosler, personal communication, April 2008). The dates may be inaccurate as a result of carbon-12 contamination from the molten ores during the smelting process (Sims, personal communication, April 2008). While the molten ore was in contact with organic material within the furnace, carbon could have been exchanged between the two materials. The ores would have had a much lower carbon-14 to carbon-12 ratio than the organic material, as they are much older than the organic material. If carbon were exchanged, the organic material would have an artificially low carbon-14 to carbon-12 ratio. This could explain why the carbon-14 dates from the organic material are older than the true age of the samples. This explanation would not explain the determination of younger dates, however the smelting site was greatly disturbed by tree root activity, therefore younger organic material could have been buried at the same depth as the older smelting evidence even though it has no chronological correlation with the smelting material. In general, the carbon-14 determinations made on organic material found at the smelting site may be inaccurate because the organic material was not deposited along with the slag.

Apart from carbon-14 dating, there are no other quantitative dating techniques appropriate for a site of this age. Other radiometric dating techniques, such as potassium-argon dating, are applicable only to much older material (Hedman 2007). Thermoluminescence dating and electron spin resonance techniques are not yet calibrated to international standards. However, the geological dating technique known as uranium series dating may be used to date slags directly. Uranium series dating has never been applied to archaeological material, but it is well understood from studies carried out on geological forms such as lava flows (Cooper *et al* 2003). In the case of a slag, a uranium series date would correspond to when the slag solidified (Sims, personal communication; Macfarlane, personal communication to Hosler 2002).

Extractive Metallurgy: Smelting

In both the ancient Old World and New World, smelting was the primary process by which metal was extracted from ores. Both crucibles and furnaces served as the reaction vessels within which a charge of ore and fuel was reduced to metal.

The process of smelting involves (1) the chemical separation of the metal from the non-metallic components of the ore, and (2) the physical separation of the metal from the silicious gangue (host rocks) associated geologically with the ore.

Most of the ore samples retrieved archaeologically at El Manchon and analyzed at CMRAE (Sharp 2003) are oxides of copper, including malachite [$Cu_2(OH)_2CO_3$] and cuprite [Cu_2O]. Metallic copper was extracted from these ores by direct reduction methods in which the furnaces were charged with a mixture of comminuted ore and charcoal. Charcoal was identified archaeologically at El Manchon, admixed with slags and with the remains of disassociated furnaces (Hosler, personal communication, April 2008). The El Manchon furnaces were made of stone, but none was sufficiently intact to determine the presence or absences of any refractory lining material on the interior vessel walls (Hosler, personal communication).

11

A typical smelting direct reduction reaction for oxide ores of copper is given by the following equation (the mineral formula does not represent stoichiometric components).

$$CuCO_3 \quad + \quad CO\uparrow \quad heat \quad Cu \; + \quad 2CO_2\uparrow$$

copper	carbon	$\rightarrow$	copper	carbon
carbonate	monoxide		metal	dioxide
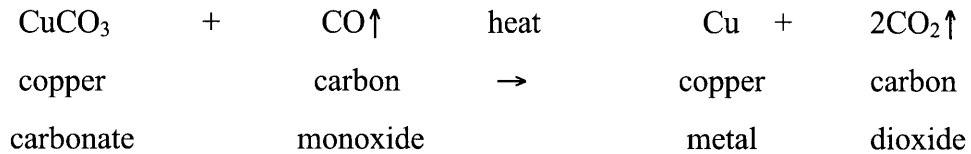
The carbon monoxide forms upon partial burning of the charcoal in the charge. Typically, the smelted copper falls through the low-density, molten slag and collects at he furnace bottom where it forms an ingot upon cooling.

Within the reaction vessel, smelting involves the physical separation of the smelted metal from the unwanted gangue that forms as a silicious melt, known as slag. If the temperature of the smelting operation is high enough to melt the slag so that it runs, the slag will float above the much denser metal and can be removed easily (Figure 1).
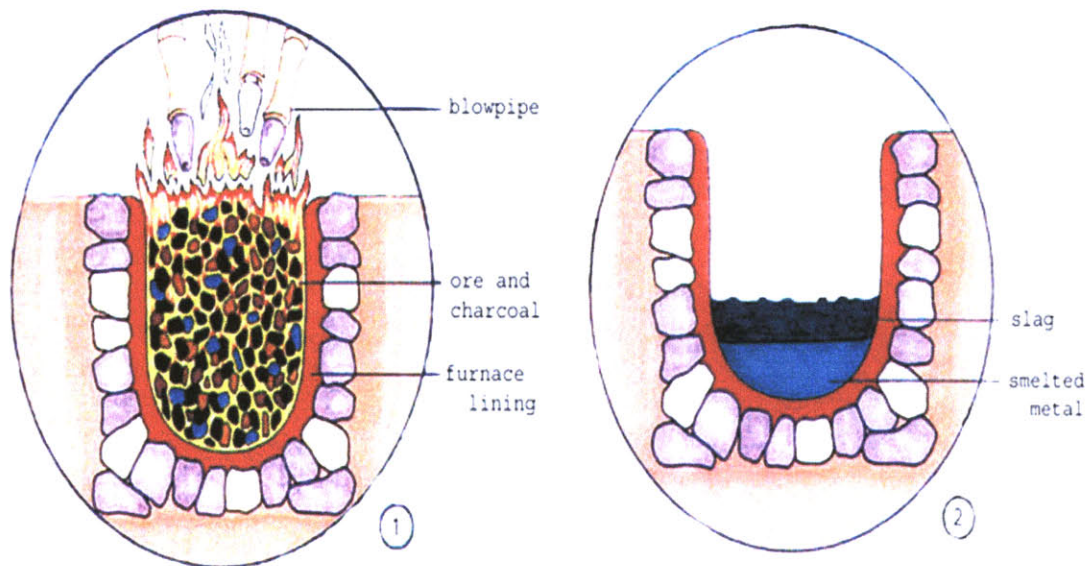
Figure 1. Simple bowl furnace of the type used in the Central Andes, before and after smelting operation (courtesy of Prof. Heather Lechtman).

Slags are important by-products of smelting. They function as scavengers, absorbing many of the non-metallic impurities present in the ore, sloughed off the furnace walls, or contributed by the charcoal ash (Bachmann 1982). Low-density, molten slags float above the smelted metal. Thus they serve not only to purify the metal but to shield it from oxygen present in the furnace environment so that is does not reoxidize.

Many of the slags accumulated in a large slag pile at El Manchon indicate that they were fully molten by the end of the smelting process (Figure 2). Rachel Sharp's calculations of the melting temperatures of the slags, based on their bulk chemical analyses, indicated a range that ran from 1150° to 1200°C (Sharp 2003). Her experimental determinations, based on reheating samples of the slags, showed that they began to slump at 1150°C, although even at a temperature of 1250°C many of the slags did not run freely. At El Manchon, strong prevailing winds may have provided sufficient oxygen to bring the internal furnace temperature to the 1200°C range.

Figure 2. Rough slag Sample 15 from El Manchon.

Slags are oxides formed by the fusion of silica [SiO_2] with metallic oxides present in the ore that is being smelted. Fayalite [$2FeO \cdot SiO_2$] is one of the most common constituents of ancient smelting slags. It is desirable, because it forms at a relatively low temperature (ca. 1178°C), the eutectic temperature of the SiO_2-FeO (wüstite) system. Electron beam microanalysis of the El Manchon slags determined them to be fayalitic, composed of crystalline fayalite and a glassy phase (Sharp 2003; Figure 3).
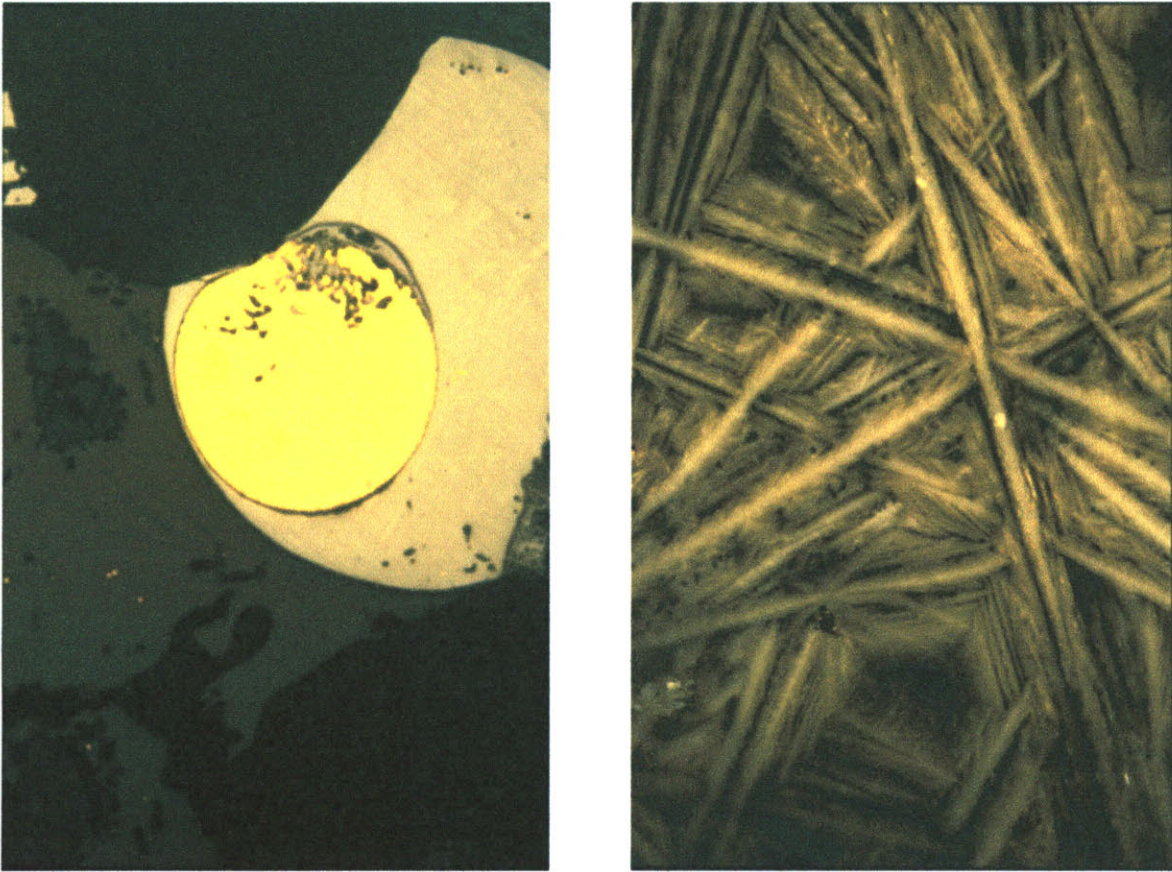
Figure 3. MIT 5258-A: Opaque section micrographs copper prill and matte (left) and crystalline fayalite (right). (Sharp 2003).

West Mexican Metallurgy

Though virtually nothing is known about the technology of Mesoamerican copper smelting, the metalworking traditions of the region are well documented. Metallurgy was introduced to West Mexico from Andean South America at about 700 CE, after complex sociopolitical organization had developed in Mexico (Hosler 1986, 1988a, 1988b, 1988c, 1990, 1994, 2003, 2005). By dating the El Manchon slags accurately, this research can offer a firm date for the only smelting technology identified in this complex technological history.

The metallurgy of West Mexico was not an indigenous development in there, but was introduced from two separate regions of South America: the Andean area including Ecuador and Peru and an area that included Colombia and lower Central America (Hosler 1986, 1988a, 1988b, 1988c, 1990, 1994, 2003, 2005). There is substantial evidence that contacts and technological exchanges between northern Andean South America and West Mexico were occurring long before metallurgy arrived in West Mexico. The oldest evidence derives from ceramic styles and a unique style of tomb construction that dates to 200 BCE (Hosler 1994).

Andean and Colombian metallurgies were most likely transferred to West Mexico through technological exchange by means of a maritime route (Hosler 1986, 1994). Evidence of the South American style of metalworking found in West Mexico is not present in any land area between the two localities. In addition, the balsa log rafts that would have been used to conduct maritime trade have been proven capable of such a voyage (Dewan 2008). While the West Mexican metallurgical tradition clearly originated in South America, West Mexican metallurgy did not replicate the metallurgies of the Andean zone, but integrated the two different technologies into a unique metallurgical tradition. Hosler has divided this tradition into two periods (Hosler 1986, 1988a, 1988b, 1988c, 1990, 1994, 2003, 2005). The first ranges from 600 CE to 1200/1300 CE, and the second period ranges from 1200/1300 CE to the Spanish invasion in 1521 CE.

During the first period of West Mexican metalworking, few tools were produced. Metal was used primarily to make elite objects (Hosler 1994). Smiths worked in gold, silver, copper, and a copper-arsenic alloy to make fishhooks, awls, bells with wirework decoration, needles, rings, and tweezers (Hosler 1994). Copper was the most common metal used for these artifacts (Hosler, personal communication, March 2008). Bells were made by lost wax casting in the Colombian tradition, while all the other objects were produced by cold-working metal blanks in the Andean tradition (Hosler 1994). Smiths focused on the production of bells, as the sound-making properties of metal were unique in the suite of materials technologies practiced by the Mesoamericans (Hosler 1994).

The second period of West Mexican metallurgy is marked by a radical increase in the number of alloys employed, which allowed for the redesign of many artifacts (Hosler 1986, 1988a, 1988b, 1988c, 1990, 1994, 2003, 2005). These new designs took full advantage of the material properties of the alloys and pushed them to their mechanical limits. Tweezers began to appear with a stylistic shell shape design (Hosler 1994). Several new artifact types also appeared: axes, axe-monies, and sheet metal ornaments (Hosler 1994). Metalworkers used copper-arsenic-silver, copper-arsenic-tin, copper-gold, copper-silver, copper-tin, copper-silver-gold, and a wider range of copper-arsenic alloys (Hosler 1994). These new alloys are notable as they allowed for refinement of design, and gave smiths control over the colors of the artifacts they produced (Hosler 1994). The ability to manipulate the colors of metal artifacts was an important development in the ritual use of metal, as the color engineering of these artifacts was purely an aesthetic choice. In addition to using previously developed techniques, West Mexican smiths began to hot work their products (Hosler 1986, 1988a, 1988b, 1988c, 1990, 1994, 2003, 2005).

El Manchon: A West Mexican Metal Smelting Site

The most distinguishing feature of el Manchon is that it is the only smelting site thus far located, mapped, and partially excavated in Mesoamerica, a region where extensive metalworking complexity has been identified and studied (Hosler 1986, 1988a, 1988b, 1988c, 1990, 1994, 2003, 2005). The site lies within the West Mexican Metalworking Zone, a zone that has a high density of copper ore deposits (Figure 4).

Figure 4. Map of location of El Manchon and topographic map of Mesoamerica, showing the limits of the West Mexican Metalworking Zone (Hosler 1994).

Because the site shows clear evidence of an area devoted to copper smelting, archaeologists believe the primary activity at El Manchon was exploitation of metal resources (Hosler, personal communication, March 2008). Though the site is located near many copper ore deposits, the location of the deposit that was mined has not yet been identified. El Manchon must have depended on outside resources for its subsistence base, as the area surrounding the site has a shallow level of eroded soil that would not have supported agriculture (Hosler, personal communication, March 2008).

Professor Dorothy Hosler of the Massachusetts Institute of Technology located and began to excavate the site of El Manchon in 1998, during her survey of the municipio of Coyuca de Catalán, Guerrero (Hosler, 1999, 2001-2003). El Manchon is located on a small tributary of the Balsas River at an elevation of 1400 m above sea level. The site itself consists of one large smelting area with two adjacent living areas (Figure 5).

18
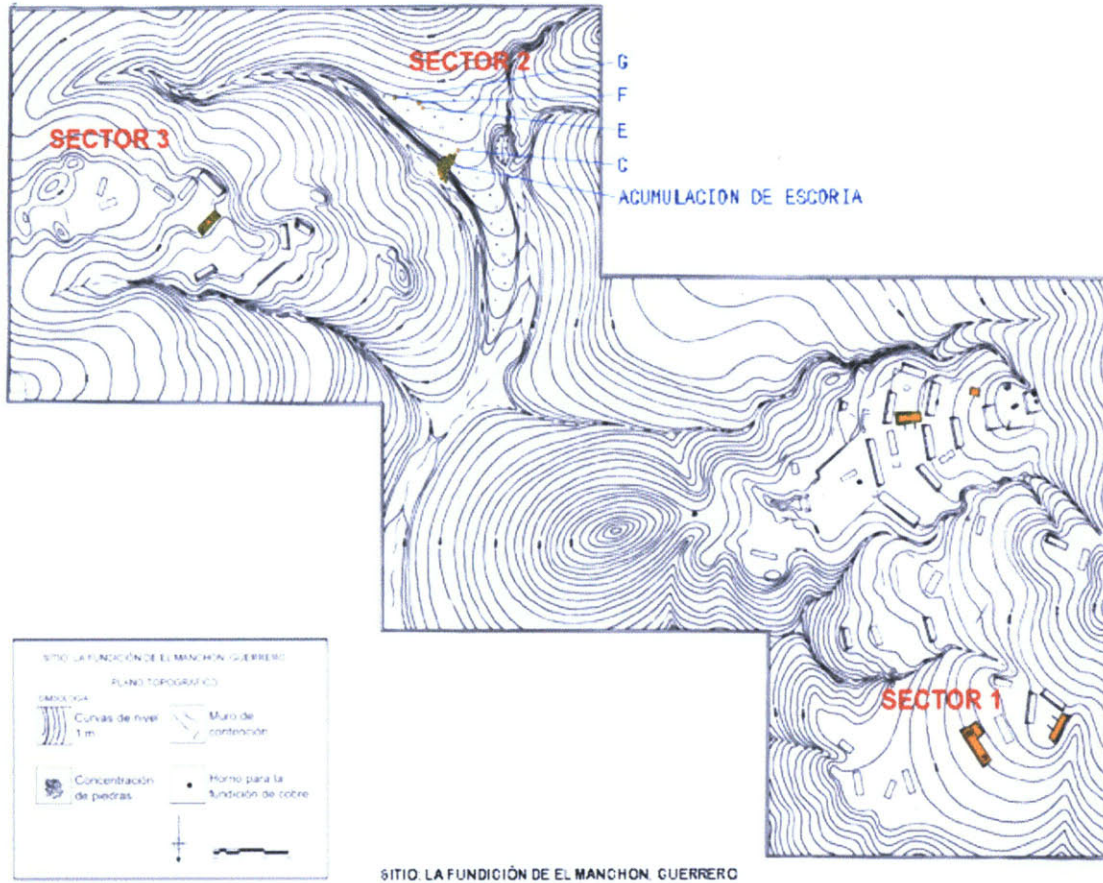
Figure 5. A map of El Manchon from unpublished fieldwork by Prof. Dorothy Hosler. Sectors 1 and 3 are habitation areas. Sector 2 is the smelting area.

The smelting sector measures 40 X 50 m^2 (Hosler, personal communication April 2008). Seven smelting furnaces have been excavated within the smelting area, but the slag samples studied in this thesis were found in another feature. They were collected from a slag pile that was eroding down a ravine (Figure 6).

Figure 6. Photograph of the slag pile at El Manchon courtesy of Prof. Dorothy Hosler.

An undergraduate DMSE-MIT thesis by Rachel Sharp in 2001 was the first work undertaken to analyze el Manchon slags and ores, prior to this thesis. Sharp's initial characterization of the slags was the starting point of this investigation. In her work, she carried out bulk analyses of the slags and developed a morphological classification system for the slag. She divided the slags into two main categories: smooth and rough, based on their surface morphologies (Sharp 2001). The most relevant result of Sharp's work for this thesis was that the slags were self-fluxing (Sharp 2001), indicating that no extraneous materials had been added to the ores to facilitate smelting. This allowed me to assume that the smelting furnaces were closed systems.

---

[1] Currently many archaeologists use the designations BCE (before the common era), to replace B.C., and CE (the common era), to replace A.D.

Methods

The Uranium Decay Series

^{238}U decays to ^{206}Pb through a series of alpha and beta decays with a half-life of 4.47 billion years (Figure 7), (Ivanovich and Harmon 1982; Faure and Mensing 2005). This overarching decay chain consists of several radioactive daughter isotopes with highly variable half-lives. These daughter isotopes and the parent isotope ^{238}U exist as trace elements in almost all materials. The isotopes are usually present only as minor impurities and do not affect the structure or chemical properties of a material significantly.

238-U Decay Series

Secular Equilibrium:
$A_{230Th} = A_{226Ra}$

$A = N\lambda$

$\lambda = \dfrac{\ln(2)}{t_{1/2}}$

Key
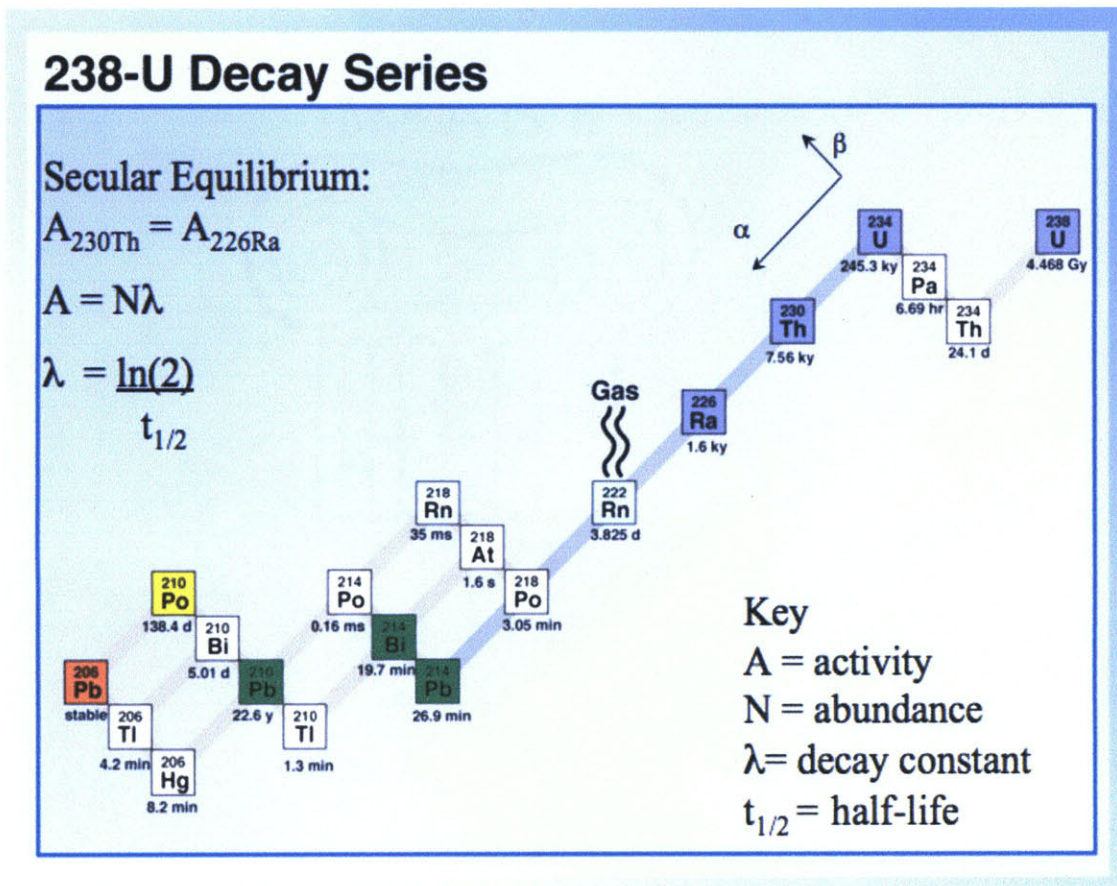A = activity
N = abundance
λ = decay constant
$t_{1/2}$ = half-life

Figure 7. A schematic of the uranium decay series, courtesy of Dr. Kenneth Sims

21

^{234}U, ^{230}Th, and ^{226}Ra are the longest-lived daughter isotopes of ^{238}U with half-lives on the order of thousands of years. The shortest lived isotopes, such as ^{218}Rn and ^{214}Po, have half-lives of a few microseconds. These quickly decaying isotopes are not practical for experimental measurements, as analytical error quickly outweighs the abundances of the isotopes. For experimental dating, ^{234}U, ^{230}Th, and ^{226}Ra are used because of their relatively long half-lives. In the case of the El Manchon slags, ^{230}Th and ^{226}Ra are used for dating. (For more information regarding isotopic choice, please refer to the chapter on Methods, section on Four Criteria).

Secular Equilibrium

Uranium series dating is based on the fact that the decay chain reaches an equilibrium state of decay after sufficient time has passed (Ivanovich and Harmon 1982; Faure and Mensing 2005). Before the decay reaches equilibrium it is in a state of disequilibrium, the degree of which can be measured to determine the age of the material being dated.

This type of equilibrium is known as secular equilibrium, in which the activity of the daughter isotope is equal to that of the parent isotope (Equation 1). The activity (Equation 2) of an isotope is equivalent to its abundance (how much of the isotope is present) multiplied by its decay constant (Equation 3) (the rate at which the radioactive isotope is decaying) (Figure 7).

(1) $\quad A_{230Th} = A_{226Ra}$

(2) $\quad A = N\lambda$

(3) $\quad \lambda = \dfrac{\ln(2)}{t_{1/2}}$

A = activity
N = abundance
λ = decay constant
$t_{1/2}$ = half-life

Because ^{238}U has such a long half-life, the abundance of ^{238}U is considered infinite even though no new ^{238}U is being created. The half-life of ^{238}U is 4.47 billion years, while ^{226}Ra has a half-life of 1,602 years and ^{230}Th has a half-life of 7,520 years (Ivanovich and Harmon 1982; Faure

and Mensing 2005). It takes about six half-lives for an isotope to achieve a low enough degree of disequilibrium with its daughter isotope so as to be measurably in secular equilibrium (Sims, personal communication, April 2008). Thus, the simple presence or absence of disequilibria can put limits on the age of a material. For example, if the material being analyzed has a measurable excess of ^{230}Th relative to its parent ^{238}U, then the age of the material is less than 450,000 years. Similarly, if the sample has a significant excess (or deficit) of ^{226}Ra relative to ^{230}Th, then its age is less than 8,000 years.

The Internal Isochron

Tighter constraints can be placed on the age of a material by using an internal isochron method. The isotopes ^{230}Th and ^{226}Ra provide an example. If the normalized activities of ^{230}Th and ^{226}Ra are plotted against one another, the plot results in a straight line known as the equiline (Figure 8).
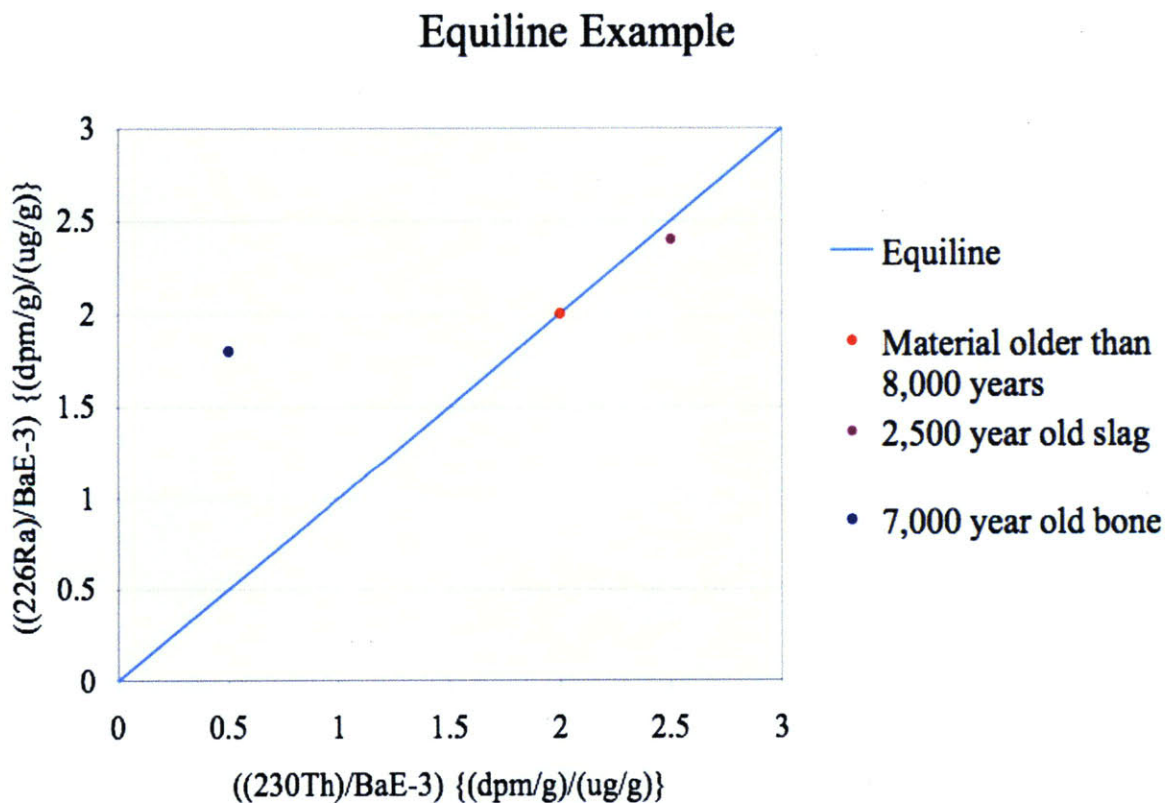
Equiline Example

Figure 8. An example of a secular equilibrium condition plotted on isotope ratio space.

The activities of the two isotopes are normalized with the stable isotope ^{138}Ba, which, as a geochemical proxy for radium, allows one to account fro any radium in a material that is not associated with the decay of ^{230}Th (Cooper *et al* 2003). The normalized ratios of these two isotopes within a material will lie along the equiline if they have achieved secular equilibrium. If the isotope ratios of a material 8,000 years or older were plotted as a single point on Figure 8, the point would lie somewhere on the blue equiline because it takes 8,000 years for ^{226}Ra and ^{230}Th to achieve secular equilibrium. If the isotope ratios of a material younger than 8,000 years were plotted on Figure 8, the point could lie anywhere but on the equiline. For example, the blue point in Figure 8 could represent a piece of 7,000-year-old hominid bone, and the maroon point could represent a sample of 2,500-year-old metallurgical slag.

As time passes and the isotopes continue to decay, the data points approach the equiline by moving in a predictable way in the y-direction. Because ^{230}Th has a much longer half-life than ^{226}Ra, the abundance of ^{230}Th is considered to remain constant during the time it takes ^{226}Ra to achieve secular equilibrium. Therefore, as time passes, the activity of ^{226}Ra (which is plotted on the y-axis) changes, but the activity of ^{230Th} (which is plotted on the x-axis) does not change. Thus, in uranium series dating, the y-axis is a proxy for time.

The direction that data points move is dependent on whether the material is rich or poor in the ^{226}Ra. If the material is ^{226}Ra-rich, this means that there is more ^{226}Ra compared to its parent isotope, ^{230}Th, than if the material were to be in secular equilibrium. If the material is ^{226}Ra-poor, this means that there is less ^{226}Ra compared to ^{230}Th than if the material were to be in secular equilibrium. Thus, in Figure 8, the dark blue data point would move up towards the blue equiline and the maroon data point would move down towards the blue equiline. Despite the predictability of the decay of isotopes in disequilibria, it is impossible to date a single data point without knowing the isotopic composition of the material at the time of its formation. In geological materials, predicting the isotopic ratio at the time of formation is difficult. In archaeological materials, including the El Manchon slags, it is not possible. In geological situations, one can make assumptions about the isotopic composition at the time of formation

based on geochemical understanding of the origin of the material. This is clearly not the case for metallurgically-produced slags.

Cogenetic Phases

Although a single phase cannot be dated using uranium decay series, a set of cogenetic phases can be dated. When a material is in a liquid or gas phase, the uranium decay series isotopes are free to mix evenly throughout the material. In such a case, measurement of the isotopic composition of the single phase material would yield only one data point plotted on $((^{226}Ra)/Ba$ vs. $(^{230}Th)/Ba)$ space. When the material solidifies, however, if several solid phases form the isotopes will fractionate into these phases because of the different chemical behaviors of both the isotopes and the solid phases (Ivanovich and Harmon 1982). For example, uranium and thorium both have larger ionic radii than radium, which impedes them from being included in crystalline structures (Ivanovich and Harmon 1982). Uranium and thorium move preferentially into amorphous phases because of their large radii, which results in fractionation of these isotopes (Figure 9).
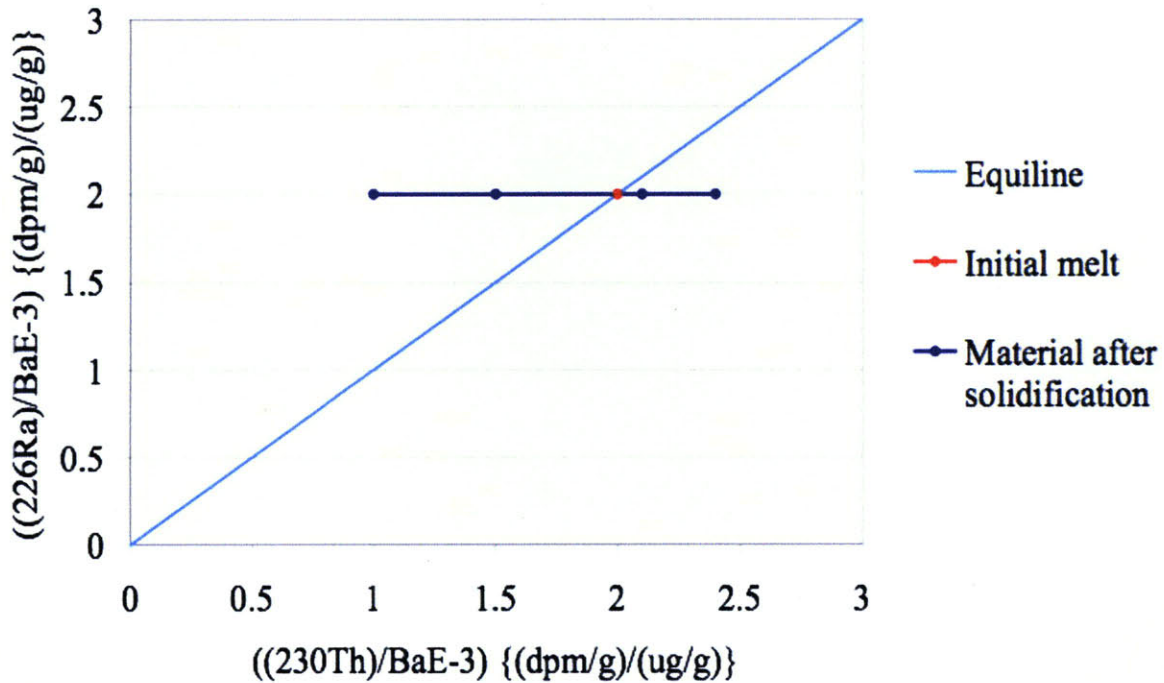
Fractionation

Figure 9. The isotope ratio space of a material that fractionated after melting and subsequent solidification. The red data point represents the initial single phase melt. Each blue data point represents a phase in the multiphase solidified material, such as a solid metallurgical slags.

Immediately after fractionation, the activities of the isotopes in the fractionated phases must always add up to the initial activities of the melt. Since no new isotopes are formed when a material melts, the existing isotopes simply mix freely. Fractionation results in phases all of which are the same age but that are not all in secular equilibrium. Because they are constrained to the same age (the y-direction in Figure 9), the fractionated phases all lie on a horizontal line that intercepts the point on the equiline for the initial melt (the red point in Figure 9). As the isotopes decay through time, each isotopic ratio will move parallel to the y-axis towards the blue equiline. This behavior is the same as that described in Figure 8. In Figure 9 however, individual values of different phases in the same material are changing, as distinct from the case shown in Figure 8, where the bulk values for two different materials are changing.

26

As noted above, the ^{226}Ra/Ba ratios of phases that are ^{226}Ra-rich will always change towards lower values of this ratio, whereas the ^{226}Ra/Ba ratios of phases that are ^{226}Ra-poor will always change towards higher values of the ratio. Like all radioactive decay, the decay of ^{226}Ra is exponential. After one half-life has passed, half of the initial abundance of the isotope remains. By plotting the normalized activities of isotopes in disequilibrium through several half-lives, it becomes clear that the data points for a multiphase material will always lie on a line that passes through the initial melt point (Figure 10).

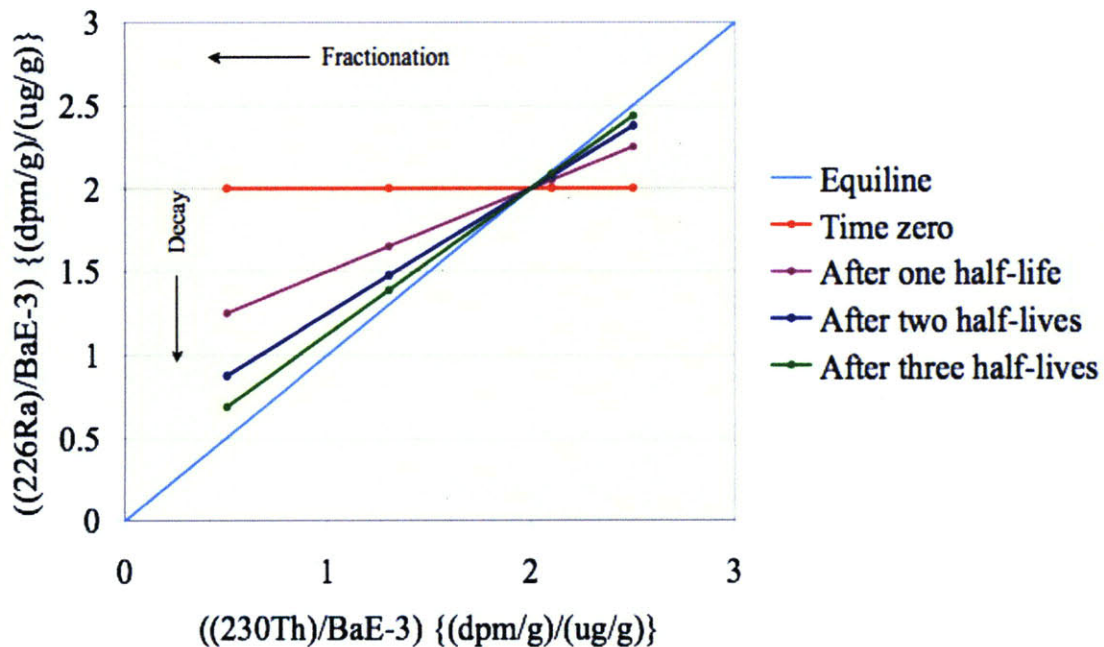## Isochron: Half-Life Decay

Figure 10. The decay of cogenetic phases through four half-lives. The normalized activities of the phases will continue to along a line with the passage of time. This line, the isochron, changes slope from a slope of zero at the time of formation, until the isotopes achieve secular equilibrium and lie on the equiline.

The line defined by the isotopic compositions of a set of cogenetic phases at a single time is known as an isochron (which means "equal time" or "same time"). In radiometric analysis, the isochron is a line of best fit due to analytical error and deviation from ideal behavior (Figure 11).

27

Because the decay rates of ^{226}Ra and ^{230}Th are known, the slope of the isochron changes in a predictable way through time. This allows the age of a sample to be calculated from the slope of the isochron. The specific relationship is

$$(4) \quad m = 1 - e^{-\lambda t}$$

m = slope of the isochron
λ = decay constant of ^{226}Ra
t = time

For a full derivation of this equation, please refer to appendix A.

Experimentally Derived Isochron

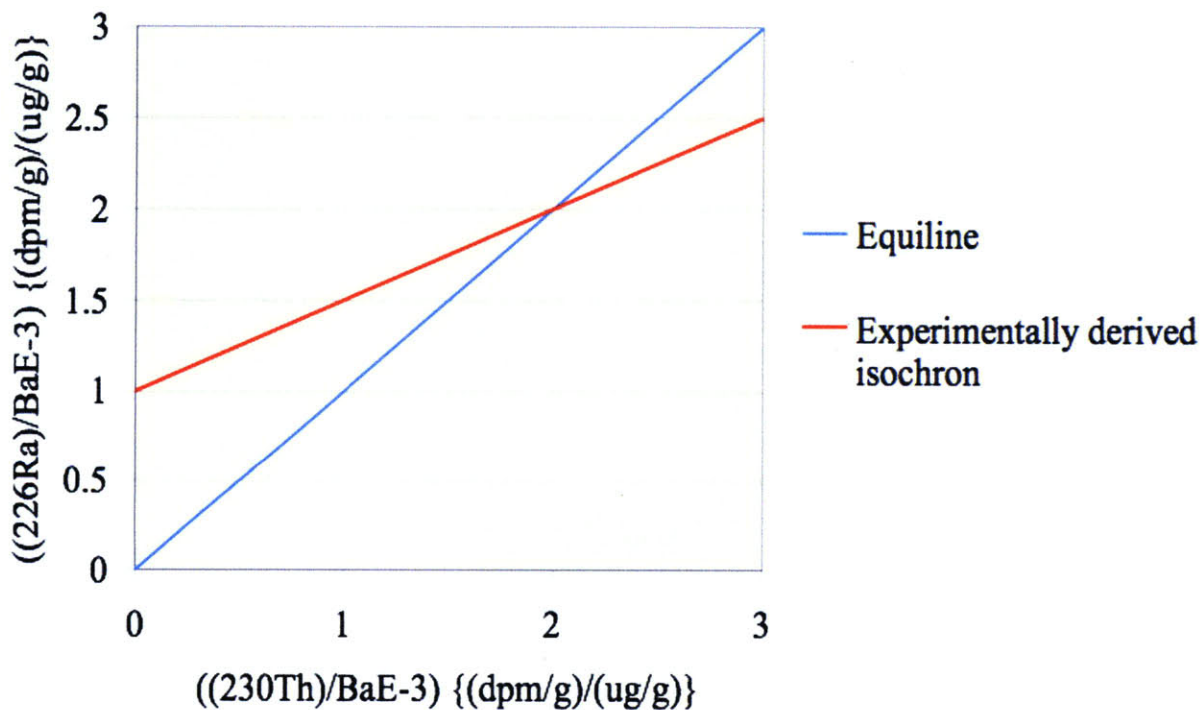Figure 11. Example of an isochron derived from experimental data.

Four Criteria

The metallurgical slags must meet four criteria to be eligible for dating by the uranium decay series method: (1) measurable presence of appropriate isotopes; (2) cogenetic phases within the slag; (3) isotopic fractionation between phases; (4) the physical separability of the phases. Work done by Christian Miller, a graduate student at WHOI, under the supervision of Dr. Kenneth Sims of the Department of Geology and Geophysics at WHOI, determined that the El Manchon slags contain measurable presences of the appropriate isotopes. I used petrographic reflected light microscopy and electron beam microanalysis to assess the presence of phases within the slags. Using an ion beam microprobe, I assessed the isotopic variation between the phases. By separating the phases experimentally through electron pulse disaggregation, hand sorting, and magnetic separations, I determined the relative ease of phase separations.

(1) Measurable Presence of Appropriate Isotopes

While uranium and its daughter elements are present as traces in most materials, the isotopes used in this study had to be present in quantities sufficient to be measured by mass spectrometry. Christian Miller demonstrated that there are sufficient abundances of the uranium series isotopes in the El Manchon slags to permit measurements, but his most important conclusion was determining which parent and daughter isotope should be used in this research.

The isotope space used to produce an isochron is determined by estimating the age of the material. From the archaeological evidence at El Manchon, the slags are estimated to be approximately 500 to 700 years old. Miller used quantitative isotope counts to confirm this age range. He demonstrated that ^{210}Pb was in secular equilibrium and that ^{226}Ra was not. ^{210}Pb has a half-life of 22 years and takes about 100 years to achieve secular equilibrium. Miller compared the activity of ^{210}Pb to the activity of its parent ^{226}Ra (refer to Figure 7 for a schematic of the uranium decay chain). ^{226}Ra is not the direct parent of ^{210}Pb, but it is the youngest parent of ^{210}Pb with a half-life longer than three days. Because the activities of ^{210}Pb and ^{226}Ra were equal, the slags had to be older than 100 years. Miller also compared the activity of ^{226}Ra with

the activity of its parent, ^{230}Th. ^{226}Ra has a half-life of 1600 years and takes approximately 8,000 years to achieve secular equilibrium. Miller's work showed that the activities of ^{226}Ra and ^{230}Th were unequal, therefore the two isotopes were not in secular equilibrium. Because ^{226}Ra and ^{230}Th are not in secular equilibrium, they can be used to construct an isochron for the El Manchon slags.

(2) Cogenetic Phases

The second criterion for dating the slags by the uranium decay method is that they contain cogenetic phases. Cogenetic phases are phases that share the same parent material and time of formation. The parent material for the El Manchon slags was the smelted ore of which the slag is a byproduct. If the slags contain only one phase, yielding a single set of isotopic ratios, no isochron can by plotted. To generate a multi-point isochron, the slag sample must have multiple phases. Each phase would determine a point on the isochron. The more data points present, the better the linear fit and error calculation between the experimental and ideal isochrons.

(3) Isotopic Fractionation

Even though cogenetic phases produce a more accurate isochron, they must also fulfill the third criterion, that they exhibit isotopic fractionation. Even if the cogenetic phases are present, if the phases do not exhibit fractionation, the isochron will still consist of only a single point. As discussed in the uranium series background section, since uranium isotopes have different chemical properties they tend to fractionate among the phases within a multiphase material. A more probable issue would arise if some of the phases exhibited almost no isotopic presence. For example, some materials, such as quartz, have internal structures that accommodate very little of the uranium series isotopes (Sims, personal communication, March 2008).

(4) Physical Separation of Cogenetic Phases

The final requirement for dating the El Manchon slags by the uranium series method is the physical separability of the cogenetic phases. In order to measure the abundances of isotopes

within different phases, the phases must be physically separate from one another. Ideally, the phases would be separated perfectly. In reality, the separation of phases is rarely complete. This will not affect the age derived from the resulting isochron, however, as the mixed phases will lie on the same isochron as the one generated by fully separated phases (Figure 12).
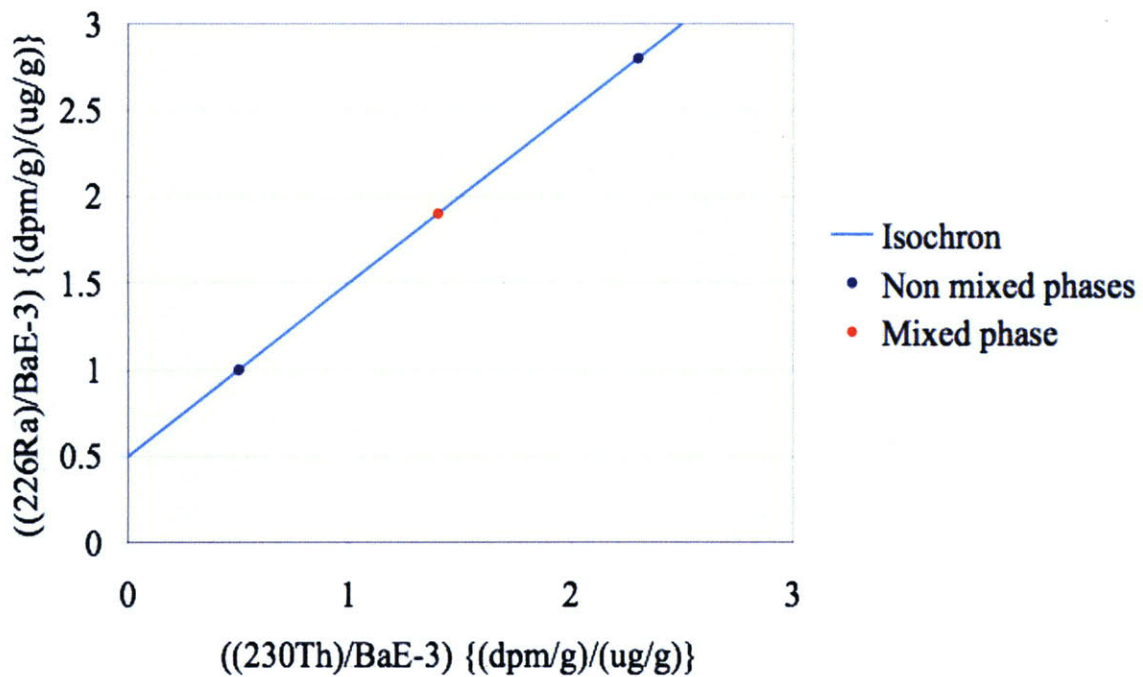
Isochron Generated by Mixed Phases

Figure 12. The blue line represents the isochron with the theoretical unmixed phases at either end. The red dot shows where a sample consisting of half of each of the phases at either end of the blue isochron.

The mixing of phases will not affect the age calculated from the isochron, but individual data points that represent the mixed phases will lie closer together than if the phases had been unmixed. Referring to Figure 12, it is clear that the two blue end points, each of which represents a pure phase, are the farthest apart they can be along the isochron line. Any mixtures of the two pure phases will locate closer together along the isochron than the two pure phases.

Phase separations that consist of multiple phases will yield the same age as will pure phases but the result is an isochron that consists of closely clustered data points, making the linear fit more uncertain.

Sectioning and Photomicrography

Table 1. Summary of initially selected slag samples.

Sample Number	Type	Site Location El Manchon 2001 Sector 2 (smelting area) Quadrant S2, E1	Photo-micrographed
1	Smooth	Slag Pit Level 3, Bag 1	
2	Rough	Slag Pit Level 3, Bag 1	
3	Rough	Slag Pit Level 3, Bag 1	
4	Smooth	Slag Pit Level 3, Bag 1	X
5	Smooth	Slag Pit Level 3, Bag 1	
6	Smooth	Slag Pit Level 3, Bag 2	X
7	Smooth	Slag Pit Level 3, Bag 2	
8	Smooth	Slag Pit Level 3, Bag 2	
9	Rough	Slag Pit Level 3, Bag 2	X
10	Rough	Slag Pit Level 3, Bag 2	X
11	Rough	Slag Pit Level 3, Bag 2	
12	Smooth	Slag Pit Level 4, Bag 3	
13	Smooth	Slag Pit Level 4, Bag 3	
14	Rough	Slag Pit Level 4, Bag 3	X
15	Rough	Slag Pit Level 4, Bag 3	X
16	Rough	Slag Pit Level 4, Bag 3	
17	Smooth	Slag Pit Level 4, Bag 3	
18	Rough	Slag Pit Level 4, Bag 3	
19	Smooth	Slag Pit Level 4, Bag 3	
20	Rough	Slag Pit Level 4, Bag 3	
21	Smooth	Slag Pit Level 3, Bag 2	
22	Rough	Slag Pit Level 3, Bag 2	
23	Rough	Slag Pit Level 3, Bag 2	
24	Rough	Slag Pit Level 3, Bag 2	
25	Rough	Slag Pit Level 3, Bag 2	

An initial collection of 25 different slags were selected from the material excavated from the slag pile in the smelting sector of El Manchon (Figure 6). Slags that would be classified as rough, smooth, or were not easily classifiable under the Sharp classification were selected (Sharp 2003). Overall, the sample collection was chosen to be representative of the slags excavated from El Manchon (refer to Appendix B). These slags were washed, sketched, and photographed with a CoolPix 5400 digital camera set to macro mode, with 5M pixel proportions and high quality. The photographs had a background of ground glass over white paper. In order to investigate the internal morphology of Samples 4, 6, 9, 10, 14, and 15 sections were prepared for petrographic reflected light microscopy. Samples 9, 10, and 15 were large enough to be sectioned twice.

The samples were sectioned with a diamond saw in the Ceramics Facility of the Center for Materials Research in Archaeology and Ethnography at MIT. The samples were cut to fit into 1" diameter round aluminum rings. They were mounted in the aluminum rings with epoxy. Using an automatic sample polisher, the samples were polished with 240 grit silicon carbide until the sample and epoxy were flush with the sample mount. The samples were then polished with 320 grit silicon carbide for five minutes, 400 grit silicon carbide for five minutes, 5 micron alumina for thirty minutes, 1 micron alumina for thirty minutes, and finally 0.02 micron colloidal silica for thirty minutes. This polishing created a smooth surface with sufficient relief to make the internal microstructure clearly visible with a microscope. Photomicrographs were then taken of samples 4, 6, 9, 10, 14, and 15 at magnifications of 100x, 200x, and 400x. These photomicrographs (Figure 13 is an example) were used to characterize the phases present in the slags (refer to the chapter on Results, section on Identification of Cogenetic Phases Through Photomicrography). Four phases were identified in all the slag samples: (1) a silicon-melt phase, (2) a quartz-like phase, (3) a copper phase, and (4) a copper-iron-sulfide phase (refer to Appendix C for more examples of photomicrographs of the El Manchon slags).
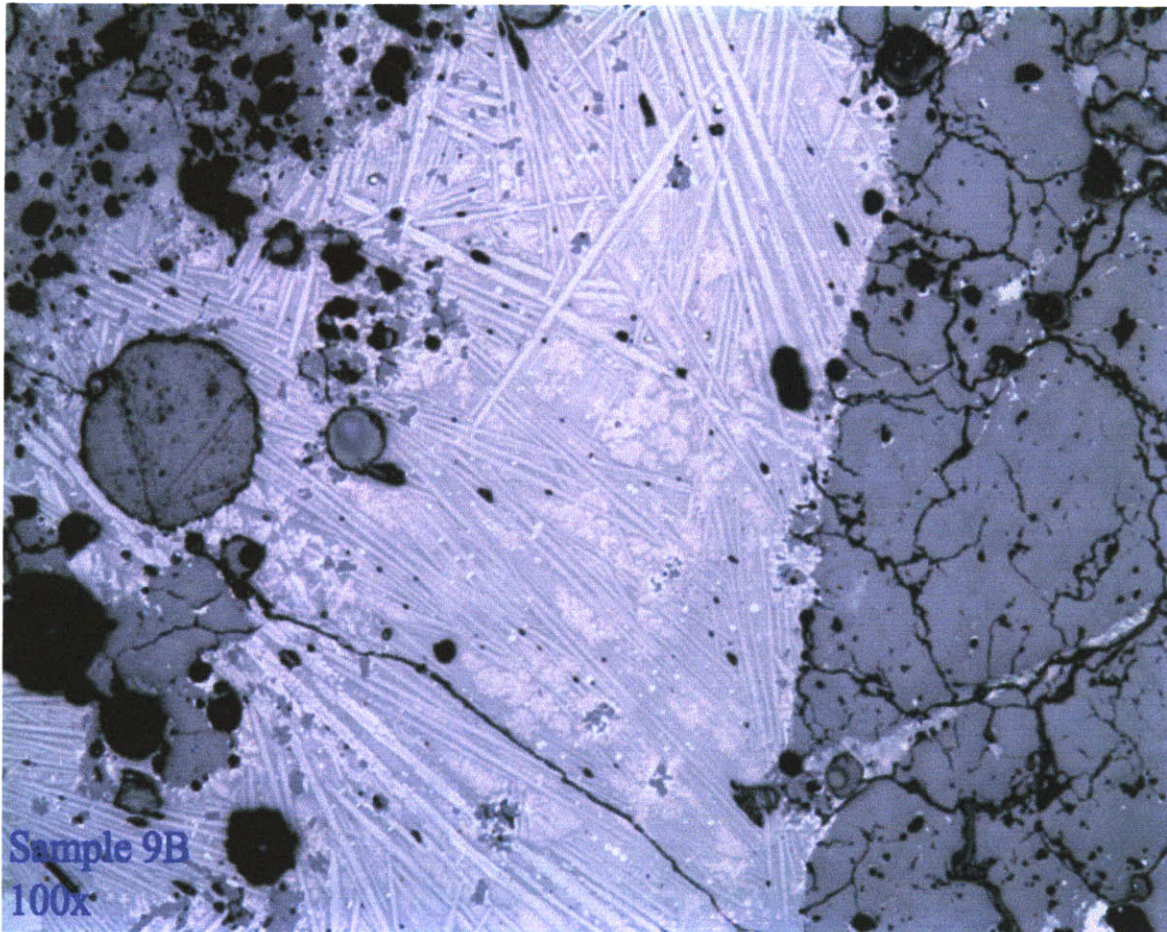
Figure 13. A photomicrograph of sample 9B.

Electron Beam Microanalysis

Electron beam microanalysis was performed on samples 22, 23, 24, and 25 (see Table 1 in the chapter on Methods, section on Sectioning and Photomicrography) to determine the elemental compositions of the four phases identified. Electron beam microanalysis uses a finely focused beam of electrons to probe a semi-spherical volume on the surface of a sample. The electron beam causes the sample to emit characteristic x-radiation that can be used to identify the elemental composition. A scanning electron microscope (SEM) images the surface of the sample so that the electron beam can be focused on a particular point (N. Chatterjee, EAPS/MIT, personal communication, August 2007). In this work electron beam microanalysis was used to

gather energy-dispersive spectra (EDS) which determine a qualitative analysis of the composition present at a particular point. The electron probe from the Earth, Atmospheric, and Planetary Science Department of the Massachusetts Institute of Technology was used. This electron probe is a JEOL-JXA-733 Superprobe manufactured by JEOL Ltd.

Dr. Nilanjan Chatterjee of MIT's Department of Earth, Atmospheric, and Planetary Science and Dr. Glenn Gaetani of the Department of Geology and Geophysics at the Woods Hole Oceanographic Institute supervised my work with the electron probe.

The same 1" round mounts used for photomicrography were also used for electron beam microanalysis. However, the 1" rounds had to be coated with a thin layer, approximately 20 nm thick, of carbon in order to prevent charge accumulation during probing (Gaetani, personal communication, August 2007). (Please see the chapter on Results, Electron Beam Microanalysis and Appendix D for details of the SEM images and EDS spectra).

Ion Beam Microanalysis

Ion beam microanalysis was performed on samples 24 and 25 (see Table 1 in the chapter on Methods, section on Sectioning and Photomicrography) to quantify the abundances of different isotopes in the four phases identified. Ion beam microanalysis uses an ion beam to produce a plasma on a roughly circular area tens of microns in diameter on the surface of a sample. The plasma is then passed through an energy filter and induced into a mass spectrometer, which separates and counts the isotopes (N. Shimizu, personal communication, October 2007). Ion beam microanalysis uses an SEM to image the surface of the sample being analyzed, which allows the user to target specific areas of the sample. I used the Cameca IMS 3f ion probe at the Woods Hole Oceanographic Institute Northeast Nation Ion Microprobe Facility to carry out this research.

This work was performed under the supervision of Dr. Nobumichi Shimizu of the Department of Geology and Geophysics at WHOI. The same 1" round sample mounts used for electron beam

microanalysis and photomicrography were used for ion beam microanalysis. The carbon coating that had been applied for electron beam microanalysis was polished off with 0.02 micron colloidal silica on an automatic polisher for 10 minutes. Before the samples could be analyzed, they had to be coated with a layer of gold about 20 nm thick.

The ion beam microprobe was calibrated to measure ^{238}U, ^{232}Th, ^{138}Ba, and ^{208}Pb. ^{138}Ba was set as the measurement reference isotope because of its high concentration in the phases, yielding 8200 counts/sec, more than four times the count rate of the other isotopes. The primary beam current was set to 3 nanoamps, which produces a probe beam of about 20 microns in diameter. The silica-rich phase and the quartz-like phase were analyzed in both slag samples. The two metal phases -- the copper and copper-iron-sulfide phases -- were indistinguishable from one another, therefore the data obtained cannot be attributed to either metal. In addition, the prills were typically smaller than the 20 micron beam size, so that the surrounding phases affected the data for the metal phases. (Please refer to the chapter on Results, section on Demonstration of Fractionation for details of the ion probe data).

Physical Separation of Cogenetic Phases

The first step in separating the phases of the slag samples was to break the slags apart. For this step, I used an electron pulse disaggregator (EPD). This is a rare machine that was custom-built by the lab technicians at WHOI. It consists of a series of capacitors connected to two steel plates that are connected to ground. The capacitors are set up in series in a bath of mineral oil to prevent oxidation. The steel plates are contained in a Teflon housing filled with water. The two steel plates are oriented at a 45° angle to each other with an adjustable gap between them.

The sample is placed in between the two plates. The ten capacitors are then charged and subsequently discharged to the steel plates. Because the plates do not touch, but the sample provides the physical connection between them, and the electric pulse forces its way through the sample. This high voltage travels along the grain boundaries in the sample, because they are the

path of least resistance. This in turn causes the sample to expand differentially and to break along the grain boundaries (B. Peucker-Ehrenbrink, personal communication, November 2007). As the sample breaks apart, the pieces fall through the gap between the two plates and into a reservoir. If the entire sample has fallen through the two plates, the water provides a sufficiently conducting medium for the electricity to jump between the two plates. Dr. Bernhard Peucker-Ehrenbrink of the Department of Marine Chemistry and Geochemistry at WHOI runs the EPD. For this work, we set the EPD to a voltage of 30 V at 1 Hz. Fifty shots were fired per round at a period of 8 shots per second. The gap was set to its smallest size: 1/8". Samples 24 and 25 were completely disaggregated.

The disaggregated grains of Samples 24 and 25 were examined by petrographic reflected light microscopy to determine into what categories the grains could be hand separated. Hand separation is a straightforward but time consuming process. Using fine tweezers and some kind of magnifying lens or microscope, I separated the grains based on visual distinctions between the sorting categories into five portions: metallics, purities, impurities, grains-with-inclusions, and fines. Metallics are categorized according to their unique, round morphologies that would be observed only in metallic material. Purities are grains composed of the characteristic dark bulk of the slags, consisting mostly of the silicon-melt phase. Impurities are grains other than metallics or purities. They included grains of white to reddish color that may be protolith or pieces of the smelting furnace lining. Grains-with-inclusions are grains that are composed of more than a single phase. The fines category is composed of grains too small to be hand-sorted with tweezers. (For more information on the hand-sorted portions refer to the chapter on Results, section on Physical Separation of Cogenetic Phases).

The final separation method I used was magnetic separation. For this work, a Frantz electromagnetic dry separator was used. The magnetic separator consists of an adjustable electromagnet whose magnetic field influences an aluminum trough that divides into two channels. The trough is set up on an incline so that the grains poured down the trough pass by the magnet. The magnet pulls the magnetic grains into one channel of the trough. The non-magnetic grains run down the other channel. I performed magnetic separations on Sample 24

under the supervision of Mr. Jerzy Blusztajn of the WHOI Plasma Mass Spectrometer Facility. (Please refer to the chapter on Results, section on Physical Separation of Cogenetic Phases for a full discussion the magnetic separation).

Results

Initial Slag Selection

Before the slag samples were modified in any way, they were photographed to document their condition directly after excavation. I categorized the slags following Rachel Sharp's 2003 classification: rough (Figure 1) or smooth (Figure 2). (For a full catalogue of the slag samples used in this work, refer to Appendix B).

Figure 14. An example of a smooth slag.
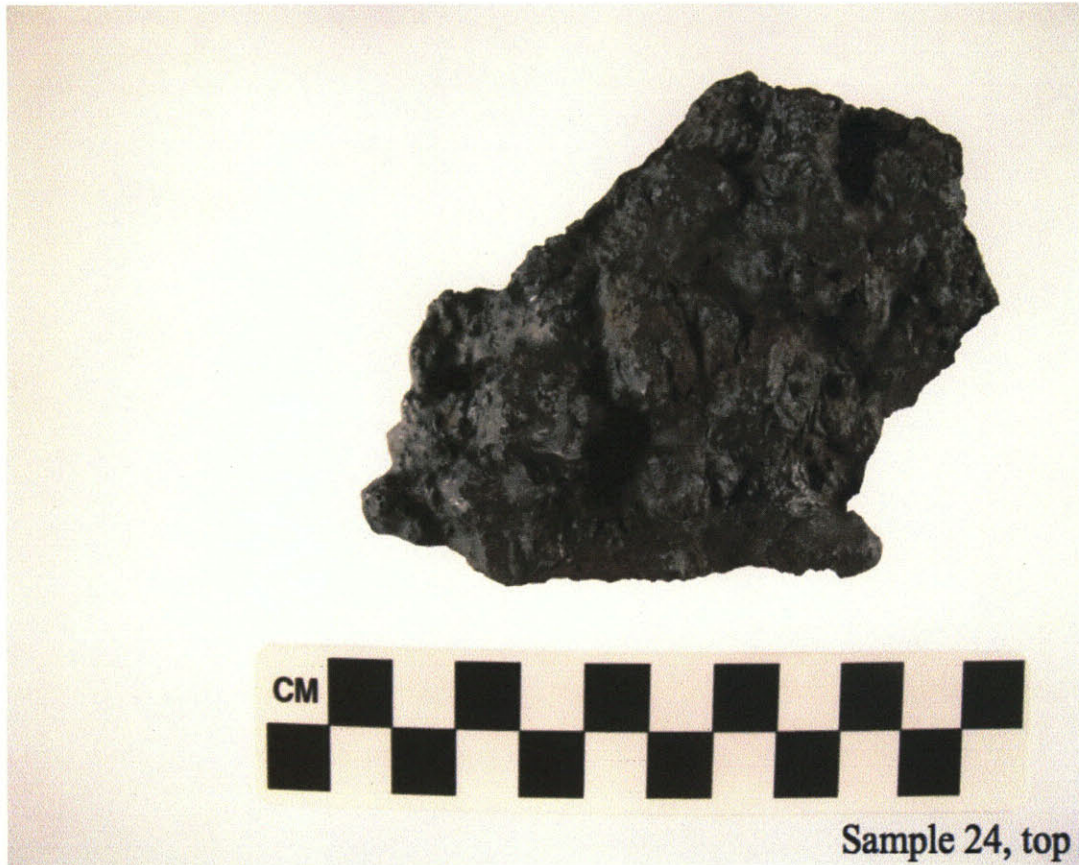
Figure 15. An example of a rough slag.

Sample Sectioning

The sectioning of the slag samples was carried out to facilitate mounting in 1" aluminum rounds. I sectioned some of the larger samples twice (Table 2). Of the initial collection of 25 slags, only 10 of the samples were sectioned and mounted successfully. During the process, some of the samples and mounts were damaged or were unsuitable for preparation with an automatic polisher. Samples that could not be polished automatically were set aside because hand polishing would have been too time consuming for the scope of this work. However, the mounted samples still form a representative selection of smooth and rough slags from El Manchon.

Table 2. Summary of sample sections.

Sample Number	Sharp's Categorization	Number of Sections
4	Smooth	1
6	Smooth	1
9	Rough	2
10	Rough	2
14	Rough	1
15	Rough	2
22	Rough	1
23	Rough	1
24	Rough	1
25	Rough	1

Identification of Cogenetic Phases Through Photomicrography

Using photomicrography, I identified four cogenetic phases in the El Manchon slags: a silicon-melt phase, a quartz-like phase, a copper phase, and a copper-iron-sulfide phase. These phases were consistent in their morphologies between both the rough and smooth slag samples, but they varied in their relative amounts within each sample. The smooth slag samples are composed primarily of the silicon-melt phase; the other phases are present in small amounts. This internal homogeneity gives rise to the even texture of the smooth slags. The rough slags exhibited a much more heterogeneous internal composition, which causes the external rough texture of these slags.

The first phase identified is the silicon-melt phase. This phase is the primary constituent of both the rough and smooth slags, although it is present in smaller amounts in the rough slags. This phase is composed of crystalline needle-like growths as well as amorphous zones (Figure 16). The degree of crystallinity in the silicon-melt phase varies between slag samples as a function of their different cooling rates. Slower-cooled examples of the silicon-melt phase exhibit a higher degree of crystallinity, as the slow-cooling crystals had more time to grow (Figure 17). The needle-like crystal growths are characteristic of iron silicates and were identified as fayalite ($2FeO \cdot SiO_2$) by Rachel Sharp (Sharp 2003).

41
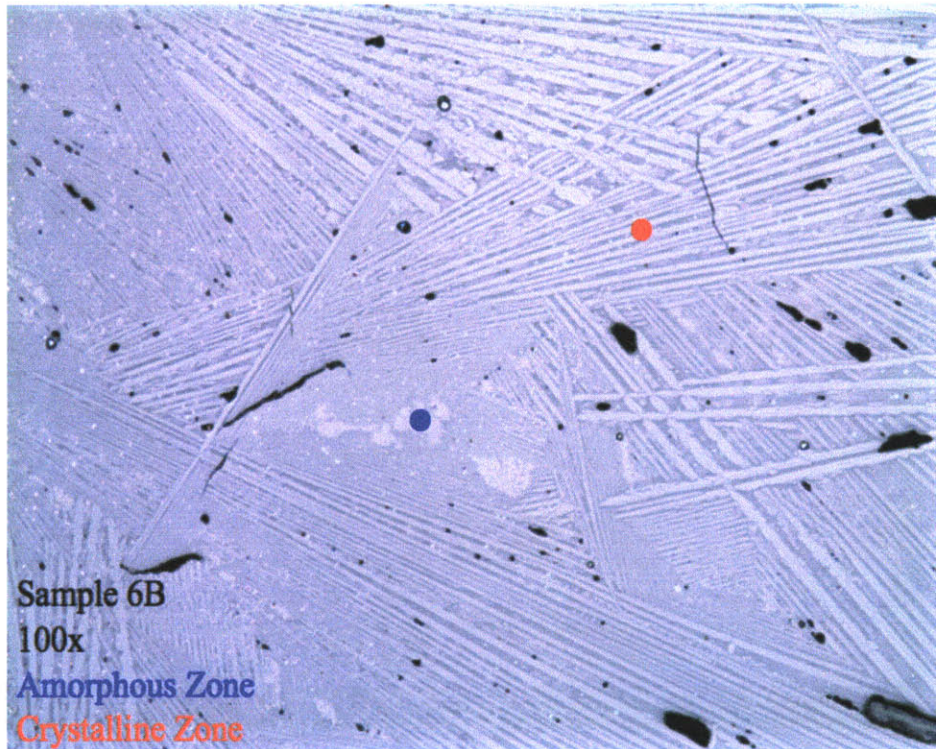
Figure 16. A photomicrograph of the silicon-melt phase, showing amorphous and crystalline zones.
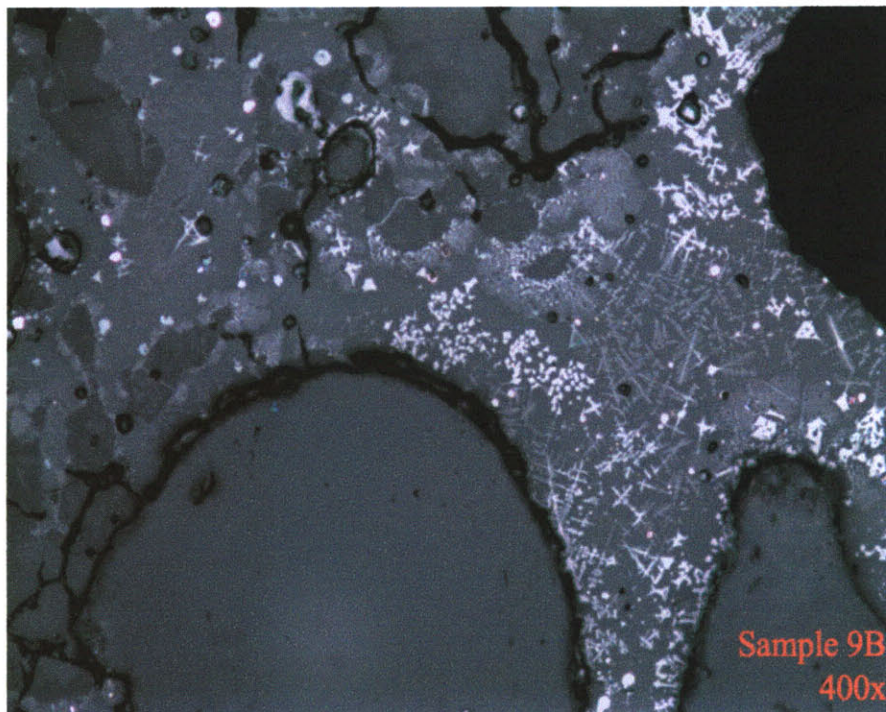
Figure 17. A photomicrograph of dendritic growth in the silicon-melt phase. Dendritic growth is characteristic of crystalline phases. This slag likely cooled sufficiently for crystalline growth to begin, then solidified before crystal growth was complete.

The second phase identified is a quartz-like phase, so-called because of its resemblance to quartz in section (Figure 18). The quartz-like phase is present in the rough slags in much greater quantity than in the smooth slags, where it is present as only a minor constituent.
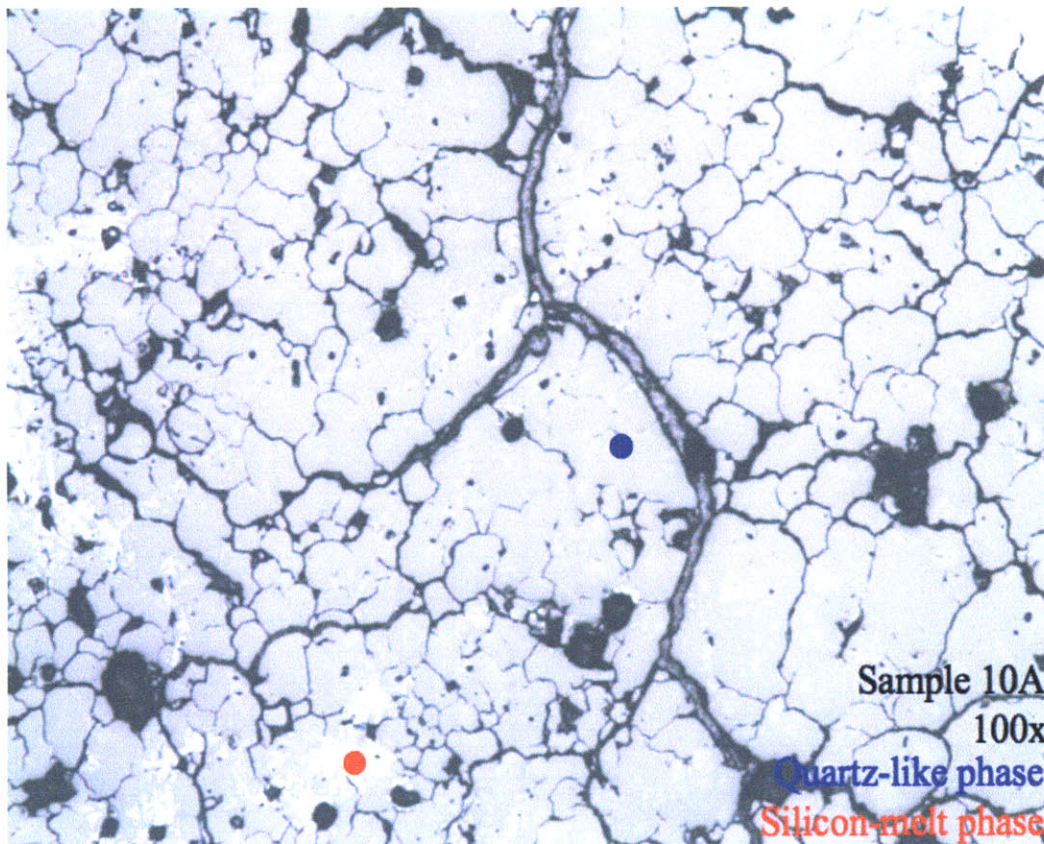
Figure 18. A photomicrograph of the quartz-like phase. The silicon-melt phase is present in the voids in the quartz-like phase.

The other two phases identified are metallic phases: a copper phase and a copper-iron-sulfide phase (metallurgical matte) (Figures 19 and 20). Both of these phases exist as round bodies, referred to as prills, embedded in the silicon-melt phase. A matte is a phase formed during metallurgical processing which contains copper, iron, and sulfur. The matte is a sulfide phase and can be present as prills or in irregular shapes. The copper-iron-sulfide phase (matte) also exists in irregularly shaped forms. Both of these phases exist only as minor components of the slag samples. The copper phase has a rosy color unique to metallic copper. Many examples of the copper phase also exhibited greenish internal surface corrosion characteristic of copper

carbonate or copper chloride corrosion products. The copper-iron-sulfide matte has a silvery color, making it possible to distinguish the two metal phases visually.
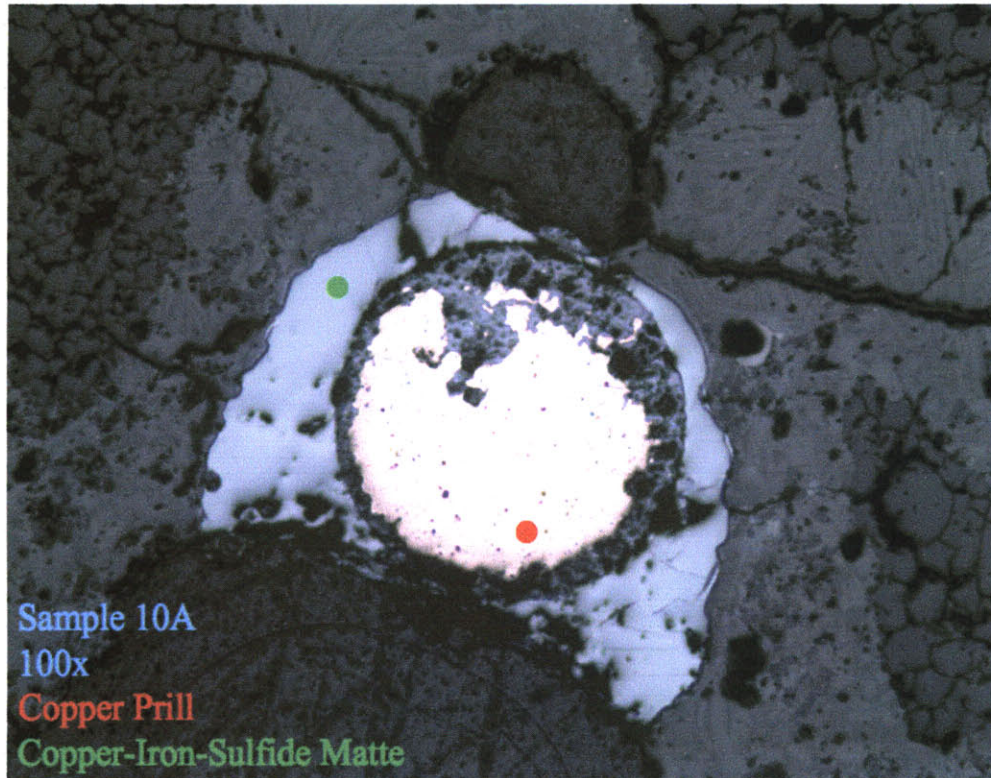
Figure 19. A photomicrograph showing a copper prill and surrounding copper-iron-sulfide matte.
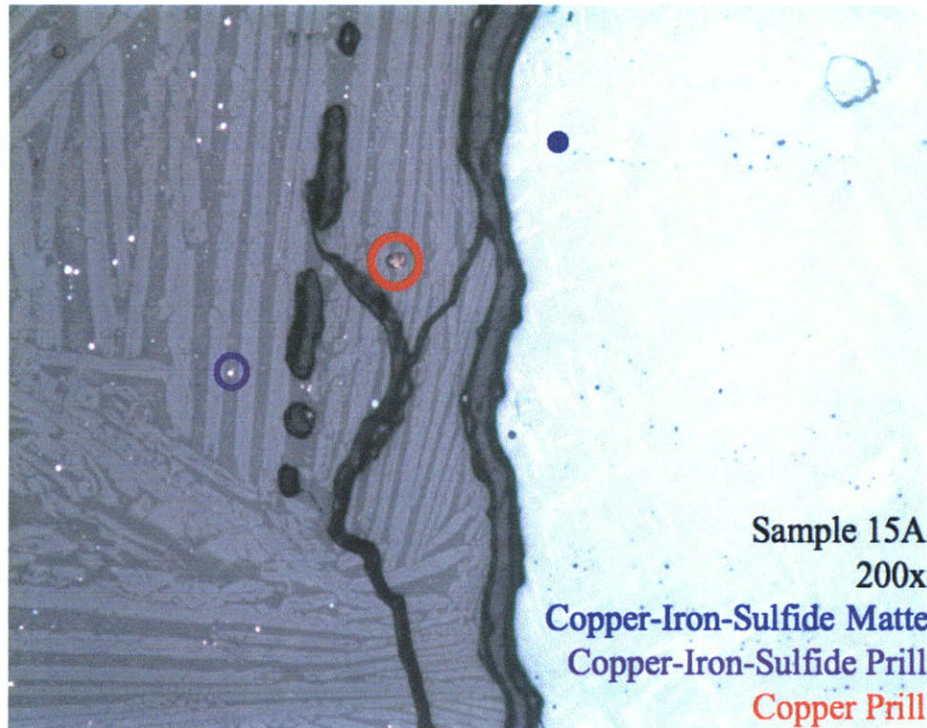
Figure 20. A photomicrograph showing an atypically large example of a copper-iron-sulfide matte. Copper and copper-iron-sulfide prills are also visible in the silica-melt phase.

Compositional Analysis of Cogenetic Phases

I used electron beam microanalysis to characterize the qualitative element compositions of the four cogenetic phases in samples 22, 23, 24, and 25. The elemental compositions of the four phases determined by electron microanalysis were consistent between samples, which allowed for elemental characterization of each phase. Some elements cannot be measured with the electron microprobe; oxygen is an example of one such element. Table 3 indicates the number of points analyzed in each slag sample, the phase analyzed, and the beam size, in microns.

Table 3. Summary of data points taken by electron beam microanalysis.

Probe Sample Number	Phase Probed	Beam Size (microns)
22.1.1	Copper-Iron-Sulfide Phase	1
22.2.1	Silicon-melt Phase	20
22.2.2	Silicon-melt Phase	10
22.2.3	Silicon-melt Phase	30
22.2.4	Quartz-like Phase	10
22.2.5	Quartz-like Phase	30
22.3.1	Epoxy Bubble	10
22.3.2	Epoxy Bubble	20
22.4.1	Copper-Iron-Sulfide Phase	1
22.5.1	Copper-Iron-Sulfide Phase	1
23.1.1	Silicon-melt Phase	10
23.1.2	Silicon-melt Phase	20
23.1.3	Copper-Iron-Sulfide Phase	1
23.2.1	Copper-Iron-Sulfide Phase	1
23.2.2	Quartz-like Phase	10
23.2.3	Quartz-like Phase	30
24.1.1	Copper Phase	1
24.1.2	Silicon-melt Phase	10
24.1.3	Quartz-like Phase	10
24.1.4	Quartz-like Phase	30
24.2.1	Copper-Iron-Sulfide Phase	1
24.3.1	Copper-Iron-Sulfide Phase	1
25.1.1	Silicon-melt Phase	10
25.1.2	Copper Phase	1
25.1.3	Quartz-like Phase	10
25.2.1	Copper-Iron-Sulfide Phase	1
25.2.2	Copper Phase	1

The elemental composition of the silicon-melt phase consists primarily of silica with a substantial presence of iron and smaller amounts of other elements (Figure 8).
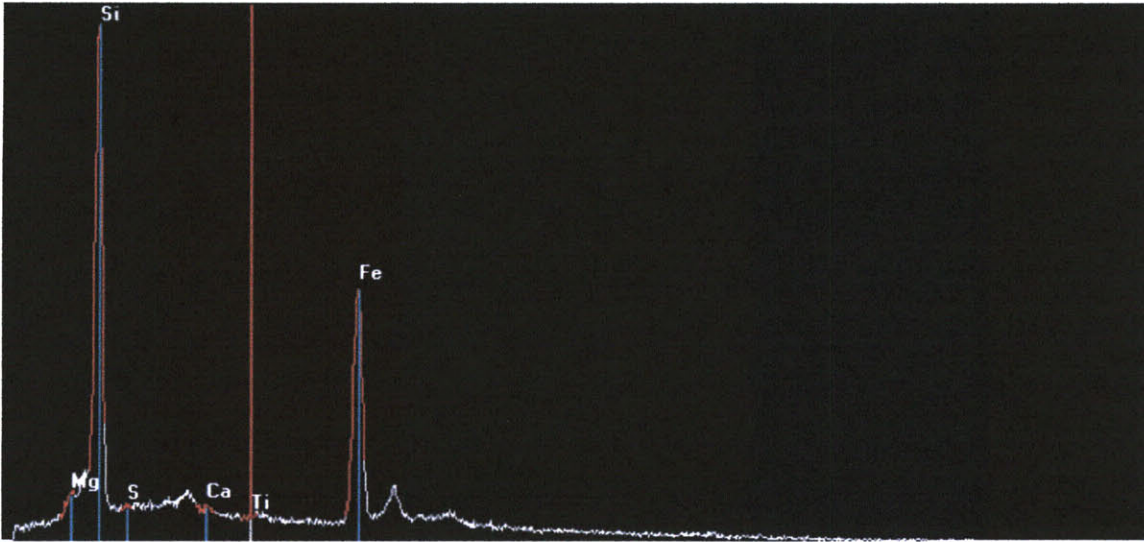
Figure 21. The EDS spectrum for point 22.2.1. This is an example of a characteristic spectrum for the silicon-melt phase.

The EDS spectra of the quartz-like phase showed the presence of only silica (Figure 22). Presumably, oxygen is a primary constituent as well, but oxygen cannot be detected on EDS spectra.
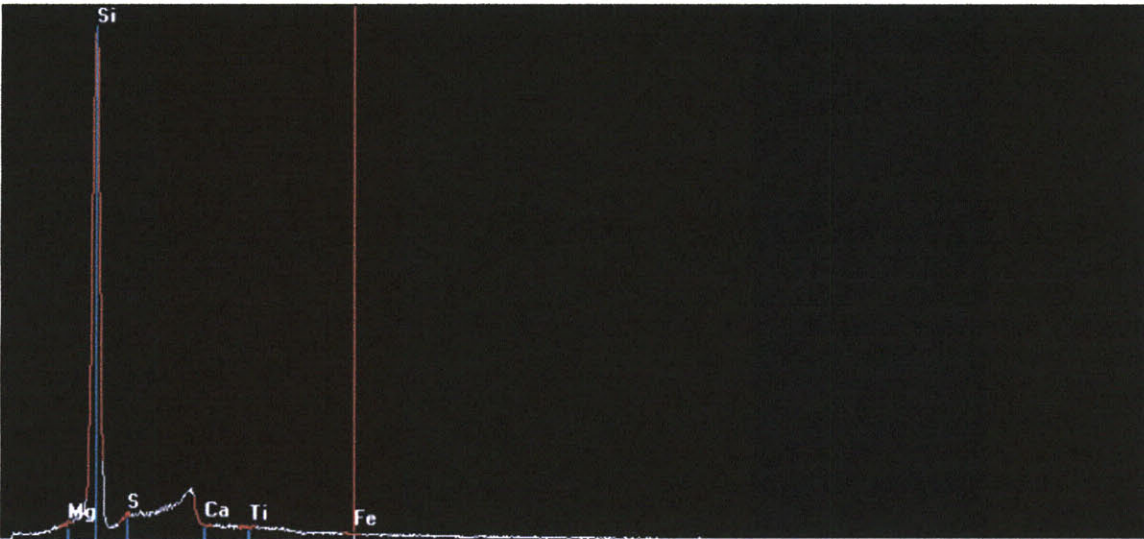
Figure 22. The EDS spectrum for point 23.2.2. This is an example of a characteristic spectrum for the quartz-like phase.

During electron beam microanalysis, the backscattered electron images used to direct the electron beam did not distinguish readily between the copper and copper-iron-sulfide phases. However, the EDS spectra for the metal phases revealed two different compositions consistent with my initial identification (Figures 23, 24, and 25).
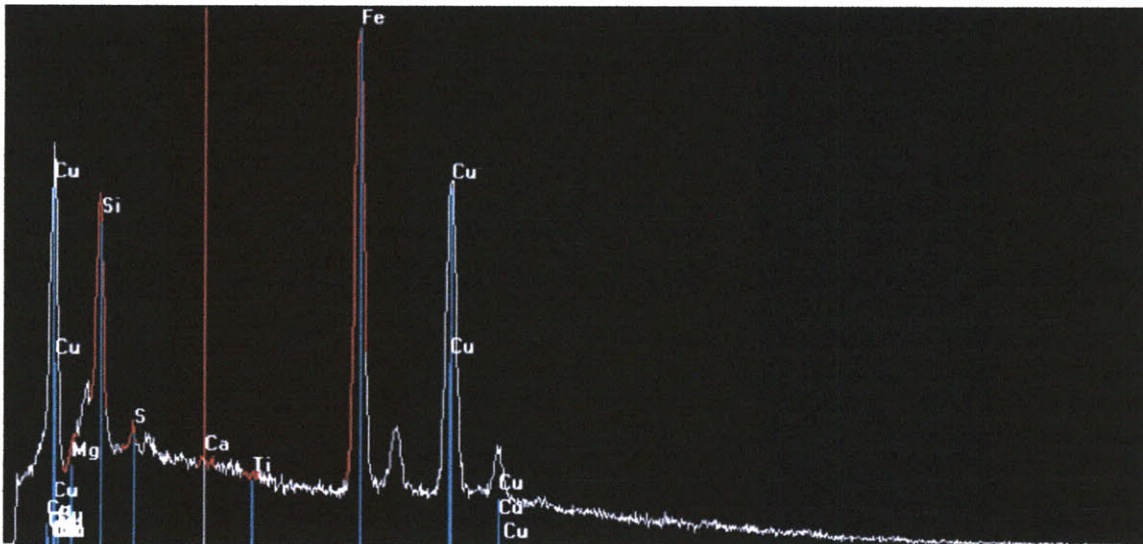
Figure 23. The EDS spectrum from point 25.2.1 with copper and iron peaks identified. This is a characteristic spectrum for the copper-iron-sulfide phase. Readings of silicon probably come from the silicon-melt phase surrounding the prill.
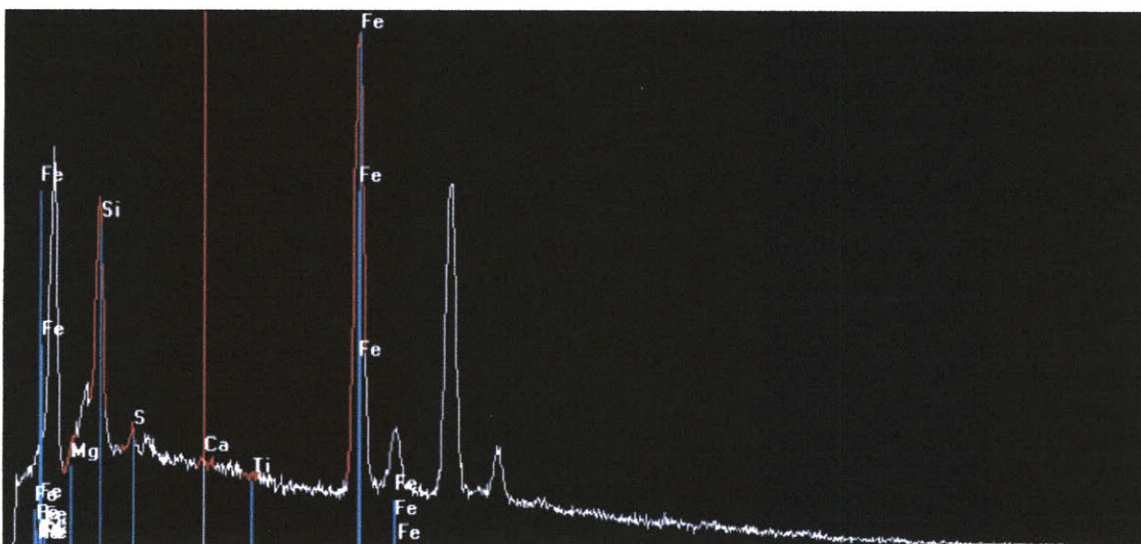
Figure 24. The EDS spectrum from point 25.2.1 with iron peaks identified. This is a characteristic spectrum for the copper-iron-sulfide phase. Readings of silicon probably come from the silicon-melt phase surrounding the prill.
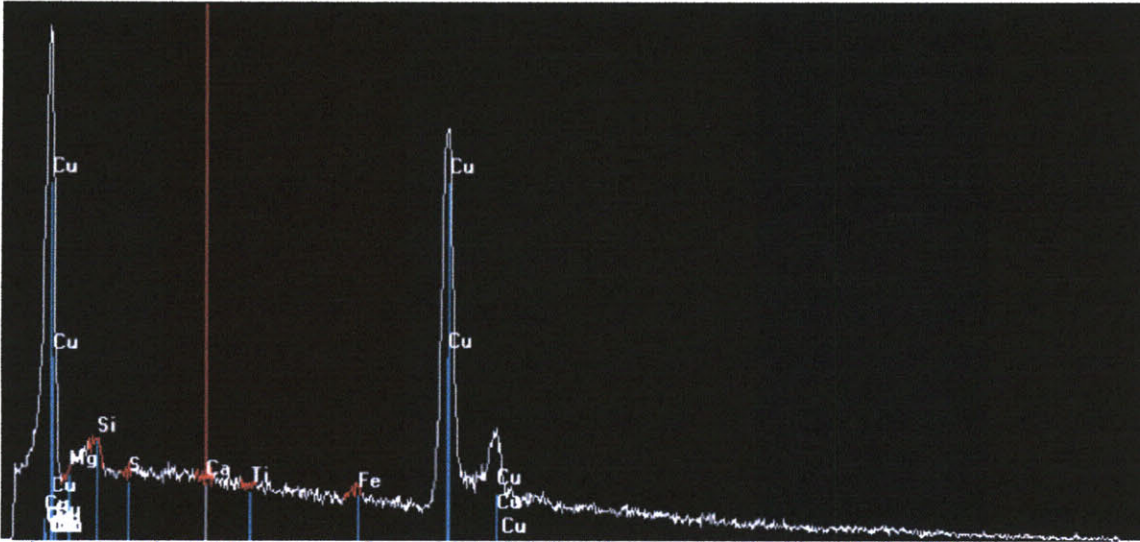
Figure 25. The EDS spectrum from point 25.1.2 with copper peaks identified. This is a characteristic spectrum for the copper phase. Readings of silicon probably come from the silicon-melt phase surrounding the prill.

Demonstration of Fractionation

Ion beam microanalysis was used to evaluate the degree of fractionation among the cogenetic phases in Samples 24 and 25. The ion probe was calibrated to measure ^{238}U, ^{232}Th, ^{208}Pb, and ^{138}Ba. Stable ^{232}Th would behave chemically in the same manner as radioactive ^{230}Th, one of the isotopes that I use to construct an isochron for the El Manchon slags. ^{226}Ra is the isotope of radium of interest in this work, but it is not measurable by ion beam microanalysis, because the concentration of radium is too low. Therefore ^{138}Ba is measured in its place. ^{138}Ba is a stable isotope that is not part of the uranium decay chain, but it is assumed to behave chemically like radium. ^{208}Pb is not a daughter isotope of the uranium decay chain, but it behaves chemically in the same manner as the isotopes of lead that are part of the uranium decay chain.

The backscattered electron images, which were acquired on the MIT electron microprobe, were used to select the regions for analysis with the ion beam microprobe. These images showed insufficient contrast between the metallic phases, therefore, the copper and copper-iron-sulfide phases were classified as one category for ion beam microanalysis.

49

Table 4 records the fractionation of thorium and barium (i.e. radium) in the various phases of Samples 24 and 25. The abundances of each element were normalized to the abundance of ^{138}Ba; therefore the intensity of the ^{138}Ba readings is shown in the table.

Table 4. Summary of data points gather be ion beam microanalysis.

Probe Sample Number	^{232}Th/^{138}Ba	^{238}U/^{232}Th	^{138}Ba/^{208}Pb	Average Intensity of Ba (Kcps)
24.SiMelt.1	0.00079	2.5443	29.9850	
24.SiMelt.2	0.00095	2.6842	26.5534	
24.SiMelt.average	**0.00087**	**2.6207**	**28.1650**	290
24.Quartz.1	0.00479	1.6117	78.9889	7
24.Metal.1	0.00076	2.6842	37.6648	260
25.SiMelt.1	0.00103	2.6408	114.2857	
25.SiMelt.2	0.00106	2.6887	106.9519	
25.SiMelt.3	0.00116	2.6897	93.1966	
25.SiMelt.average	**0.00108**	**2.6738**	**104.0583**	250
25.Quartz.1	0.00123	2.6098	89.0472	
25.Quartz.2	0.00134	2.4925	100.6036	
25.Quartz.3	0.00142	2.4014	97.5610	
25.Quartz.average	**0.00133**	**2.4962**	**95.4806**	180
25.Metal.1	0.00092	2.4565	108.3424	
25.Metal.2	0.00097	2.4742	102.3541	
25.Metal.average	**0.00095**	**2.4656**	**105.2632**	240

Fractionation occurred in both samples. Sample 24 shows a greater degree of fractionation than Sample 25. A larger degree of fractionation in a sample indicates that the data points from that sample, shown on a plot of the isotopic ratios ^{226}Ra/^{138}Ba vs ^{230}Th/^{138}Ba will exhibit a large spread along the x-axis, leading to a better linear fit for the isochron. However, both samples exhibit sufficient fractionation to be suitable for uranium series dating (Table 5).

Table 5. Fractionation in Samples 24 and 25.

Probe Sample Number	^{232}Th/^{138}Ba	^{238}U/^{232}Th	^{138}Ba/^{208}Pb	Average Intensity of Ba (Kcps)
24.SiMelt.average	0.00087	2.6207	28.1650	290
24.Quartz.1	0.00479	1.6117	78.9889	7
24.Metal.1	0.00076	2.6842	37.6648	260
25.SiMelt.average	0.00108	2.6738	104.0583	250
25.Quartz.average	0.00133	2.4962	95.4806	180
25.Metal.average	0.00095	2.4656	105.2632	240

Physical Separation of Cogenetic Phases

After the samples were disaggregated by electron pulse dissaggregation (see the chapter on Methods, section on Physical Separation of Cogenetic Phases for a discussion of EPD), the grains were hand-sorted. Because of the time intensity of hand-sorting, only Sample 24 was hand-sorted completely. I used hand-sorting to divide the sample into five portions: metallics, purities, impurities, grains-with-inclusions, and fines. Metallics are categorized according to their unique, round morphologies that would be observed only in metallic material. Purities are grains composed of the characteristic dark bulk of the slags, consisting mostly of the silicon-melt phase (Figure 26). Impurities are grains other than metallics or purities (Figure 27). They included grains of white to reddish color that may be protolith or pieces of the smelting furnace lining. Grains-with-inclusions are grains that are composed of more than a single phase (Figure 28). The fines category is composed of grains too small to be hand-sorted with tweezers.
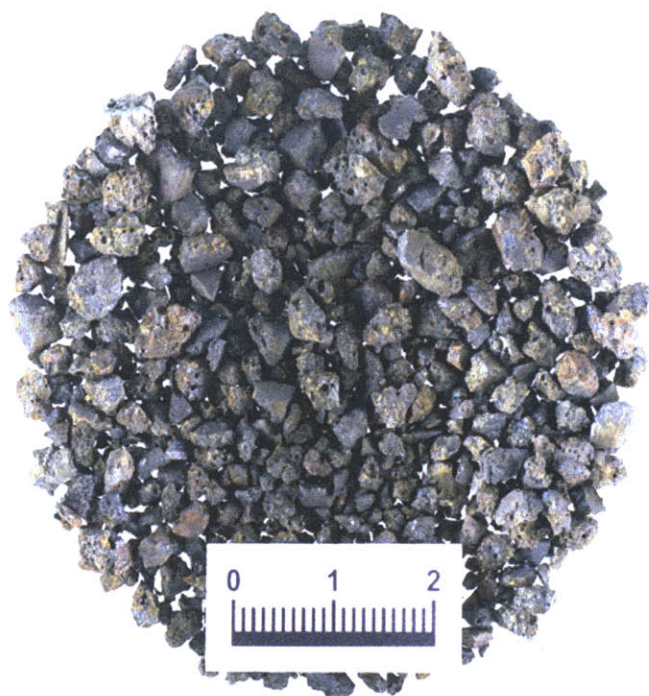
Figure 26. A portion of the purity separation of Sample 24.
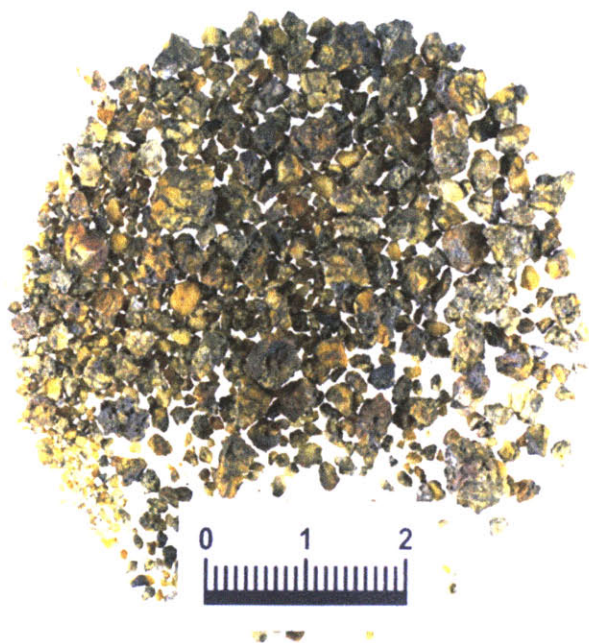
Figure 27. A portion of the impurities separation of Sample 24.
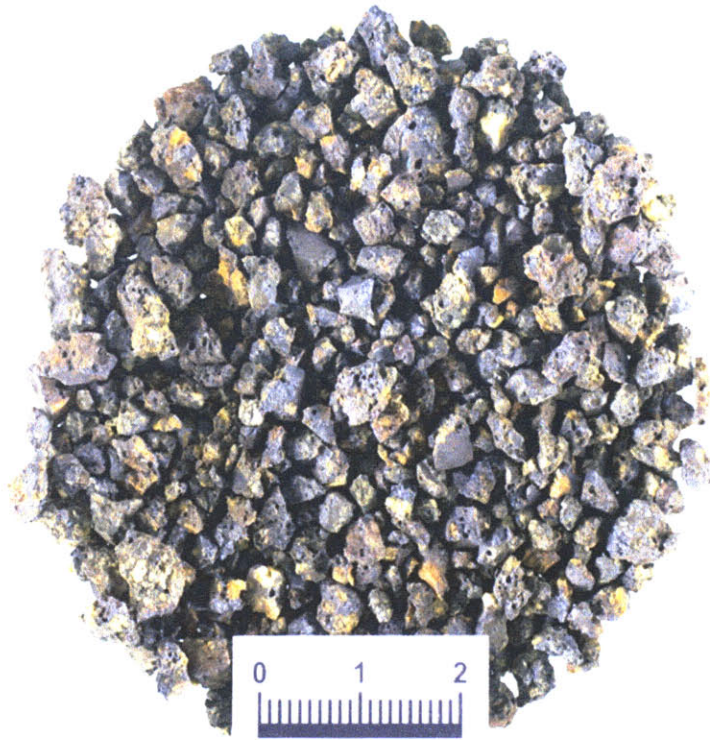
Figure 28. A portion of the grains-with-inclusions separation of Sample 24.

I sorted the fines by magnetic separation with a Frantz electromagnetic dry separator. This enabled me to group the fines into three degrees of magnetism. The entire bulk of the fines was separated with a current setting of 0.1 amps. The non-magnetic portion of this first separation was labeled Vial 1. The remaining magnetic portion was then separated with a current setting of 0.02 amps. The non-magnetic portion of this separation was labeled Vial 2, and the magnetic portion was labeled Vial 3. Using a hand-magnet, the contents of Vial 3 and the hand-sorted metallics were separated into magnetic and non-magnetic portions.

Through this combination of techniques, I sorted Sample 24 into a total of nine separate portions (Table 6). The isotopic ratios of each of these separations will constitute a data point that I will use to construct the isochron for this slag sample. Therefore, the physical separations of the El Manchon slags are sufficient to produce a multipoint isochron.

Table 6. Summary of the physical separations of grains in Sample 24.

Sample Number	Composition	Weight (grams)
V24-1	Vial 1 (non-magnetic fines)	2.962
V24-2	Vial 2 (non-magnetic fines)	5.399
V24-3	Vial 3, magnetic portion of fines	36.051
V24-4	Metallics, non-magnetic portion	0.250
V24-5	Metallics, magnetic portion	0.247
V24-6	Inclusions	1.450
V24-7	Vial 3, non-magnetic portion of fines	1.057
V24-8	Powdered purities portion	2.411
V24-9	Powdered impurities portion	2.717

Conclusion

Archaeological Utility of Uranium Series Dating

This thesis is the first attempt to apply uranium series dating to any kind of archaeological material. In demonstrating that uranium series dating can be used to provide a date for the El Manchon slags directly, this work also demonstrates that uranium series dating can be used with any archaeological smelting or refining slag provided that it meets the four criteria required by the analytical regime. Uranium series dating would offer a new method by which archaeologists can determine the dates of sites with evidence of ore smelting or metal refining. Of course, the use of this new tool is still in an experimental stage. Analysis of a variety of slags with the same rigor that characterizes the research reported in this thesis will determine if uranium series dating is universally applicable to slag samples.

Dating the El Manchon Slags

The primary goal of this thesis has been to develop a method for determining whether the smelting technology at El Manchon was preHispanic or postHispanic in date. At El Manchon, archaeological dating methods, such as radiocarbon (absolute method) or pottery typing (relative method), proved inadequate to date the smelting technology directly. In addition, radiocarbon dates determined for other areas of the site yielded an age range that spans both preHispanic and postHispanic eras (ca. 750 to 1850 CE). If the geological technique known as uranium series dating can be adapted in order to provide dates for the El Manchon slags, it will be possible to date directly the smelting technology that was performed at El Manchon.

The overall goal of uranium series dating is to produce an isochron experimentally. An isochron is a plot of the normalized activities of two measurable radioactive isotopes in the cogenetic phases of a slag sample that takes the form of a straight line (Figure 29).

Theoretical Isochron
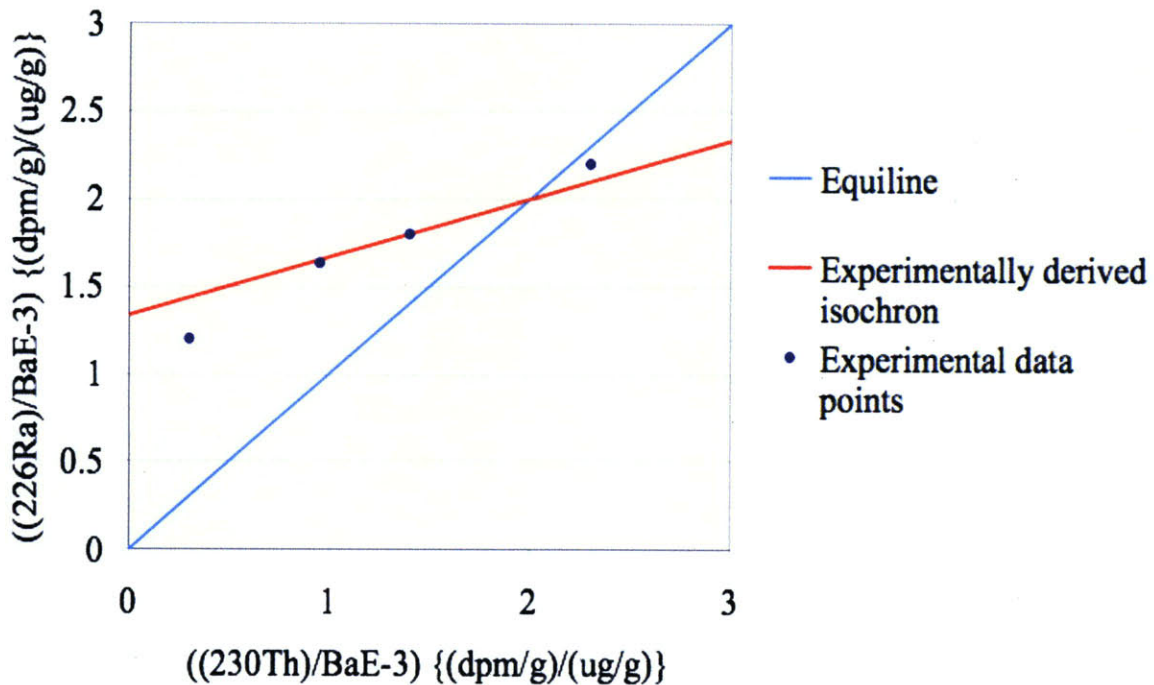
Figure 29. An example of theoretical data points in dark blue, with a constructed isochron line in dark red. By comparing the slope of the isochron with the slope of the equiline, a date can be determined for the sample.

By comparing the isochron to the equiline, the age of the slag sample can be determined. The equiline is the plot of the normalized activities of two measurable radioactive isotopes in the cogenetic phases of a material that has aged enough to achieve secular equilibrium between the two isotopes. Because the rate at which isotopes decay to secular equilibrium is well understood, a comparison between the isochron and the equiline allows an age to be calculated for a sample.

This thesis evaluated four criteria to determine whether or not uranium series dating through the experimental establishment of an isochron would be appropriate for dating the El Manchon slags: (1) measurable presence of appropriate isotopes in the slags; (2) cogenetic phases within the slags; (3) isotopic fractionation between cogenetic phases; and (4) the physical separatability of the cogenetic phases. The work of Dr. Kenneth Sims and Dr. Christian Miller at the Woods Hole Oceanographic Institute demonstrated that adequate, measurable abundances of the isotopes ^{230}Th and ^{226}Ra, the isotopes of interest for this study, are present in the El Manchon slags.

My thesis research went further to demonstrate that the slags contain four distinct cogenetic phases: a silicon-melt phase, a quartz-like phase, a copper phase, and a copper-iron-sulfide phase. Measurements of the ^{226}Ra/^{138}Ba vs ^{230}Th/^{138}Ba normalized activities within these phases would yield an isochron with at least four points, sufficient to determine the date of the slags. I measured the extent of isotopic fractionation within each of the four phases through ion beam microanalysis. Finally, I separated slag Sample 24 experimentally into nine portions that represent the four cogenetic phases, demonstrating that the El Manchon slags can be physically separated successfully.

My research demonstrates that the El Manchon slags meet the four criteria established by geochemistry and that they would be good candidates for uranium series dating. The age determined for a piece of El Manchon slag provides the date when the slag solidified, thereby effectively dating the smelting technology directly. While both rough and smooth slags excavated at El Manchon met all four criteria, the rough samples are better suited to uranium series dating. The smooth slags are almost homogenously composed of one phase, whereas the rough slags contain greater quantities of the four phases. The presence of ample amounts of each phase facilitates the analysis.

Further Research

I have begun the next step in my research, which involves the dissolution of El Manchon slag Sample 24 in preparation for the column chemistry necessary to measure quantitative isotope abundances in each phase separation. The column chemistry serves to purify the elements of interest, in this case uranium, radium, thorium, and lead. Once the elements have been purified, mass spectrometry will quantify the abundances of the isotopes of each of the elements. This work is being carried out at WHOI under the supervision of Dr. Kenneth Sims, Department of Geology and Geophysics. The calculation of a date for El Manchon slag Sample 24 will demonstrate the pre- or postHispanic nature of the smelting carried out at El Manchon.

My results will offer archaeologists a new dating method central to the interpretation of extractive metallurgical technologies of pre-industrial and prehistoric societies.

Appendix A: Mathematical Derivation of Isochron Slope

Let us consider a decay chain:
$$^{230}Th \rightarrow\ ^{226}Ra$$
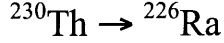
^{230}Th decays exponentially into its daughter isotope ^{226}Ra. For the time frame of the isochrons used for the El Manchon slags, ^{230}Th is not significantly replenished, therefore ^{230}Th decay is as follows,

$$\frac{-dN_{230Th}}{dt} = \lambda_{230Th}\, N_{230Th} \tag{1}$$

^{226}Ra decays exponentially as well, but is being replenished by ^{230}Th,

$$\frac{dN_{226Ra}}{dt} = \lambda_{230Th}\, N_{230Th} - \lambda_{226Ra}\, N_{226Ra} \tag{2}$$

The amount of ^{230}Th through time,

$$N_{230Th} = N^{\circ}_{230Th}\, e^{-\lambda_{230Th}\, t} \tag{3}$$

Substituting (3) into (2),

$$\frac{dN_{226Ra}}{dt} = \lambda_{230Th}\, N^{\circ}_{230Th}\, e^{-\lambda_{230Th}\, t} - \lambda_{226Ra}\, N_{226Ra} \tag{4}$$

Setting (4 = 0),

$$\frac{dN_{226Ra}}{dt} - \lambda_{230Th}\, N^{\circ}_{230Th}\, e^{-\lambda_{230Th}\, t} + \lambda_{226Ra}\, N_{226Ra} = 0 \tag{5}$$

Solving (5) for N_{226Ra}

$$N_{226Ra} = \frac{\lambda_{230Th}}{\lambda_{226Ra} - \lambda_{230Th}}\ N^{\circ}_{230Th}\, (e^{-\lambda_{230Th}\, t} - e^{-\lambda_{226Ra}\, t}) + N^{\circ}_{226Ra}\, e^{-\lambda_{226Ra}\, t} \tag{6}$$

Assuming there is no initial ^{226}Ra ($N^{\circ}_{226Ra} = 0$), (6) becomes:

$$N_{226Ra} = \frac{\lambda_{230Th}}{\lambda_{226Ra} - \lambda_{230Th}}\ N^{\circ}_{230Th}\, (e^{-\lambda_{230Th}\, t} - e^{-\lambda_{226Ra}\, t}) \tag{7}$$

Assume that
$$\lambda_{226Ra} - \lambda_{230Th} = \lambda_{226Ra},$$
and
$$e^{-\lambda_{230Th}\,t} = 1$$
because the decay constant of ^{230}Th is sufficiently low.
This makes (7)

$$N_{226Ra} = \frac{\lambda_{230Th}}{\lambda_{226Ra}}\, N^{\circ}_{230Th}\,(1 - e^{-\lambda_{226Ra}\,t}) \tag{8}$$

Multiplying (7) by λ_{226Ra}

$$\lambda_{226Ra\,v}N_{226Ra} = \lambda_{230Th}\, N^{\circ}_{230Th}\,(1 - e^{-\lambda_{226Ra}\,t}) \tag{9}$$

Substituting in activities,

$$A_{226Ra} = A_{230Th}\,(1 - e^{-\lambda_{226Ra}\,t}) \tag{10}$$

From (3), for initially present ^{226}Ra

$$A_{226Ra} = A^{\circ}_{226Ra}\, e^{-\lambda_{226Ra}\,t} \tag{11}$$

Now let us assume, there is decay of initially present ^{226}Ra as well as decay of ^{226}Ra produced by ^{230}Th,

$$A_{226Ra} = A^{\circ}_{226Ra}\, e^{-\lambda_{226Ra}\,t} + A_{230Th}\,(1 - e^{-\lambda_{226Ra}\,t}) \tag{12}$$

Normalizing (12) by A_{138Ba},

$$\frac{A_{226Ra}}{A_{128Ba}} = \frac{A^{\circ}_{226Ra}}{A_{128Ba}}\, e^{-\lambda_{226Ra}\,t} + \frac{A_{230Th}}{A_{128Ba}}\,(1 - e^{-\lambda_{226Ra}\,t}) \tag{13}$$

In a linear graph of (A_{226Ra}/A_{138Ba}) against (A_{230Th}/A_{138Ba}), an isochron, the slope of the line will be :

$$(1 - e^{-\lambda_{226Ra}\,t}) \tag{14}$$

Because λ_{226Ra} is known, an age can be calculated from the slope of an isochron.

Appendix B: Initial Slag Sample Collection

All photographs were taken with a CoolPix 5400 digital camera set to macro mode, with 5M pixel proportions and high quality. The photographs had a background of ground glass over white paper.

Table 7. Summary of the slag samples used in this work.

Sample No.	Type	Dimensions (cm)	Shown Here
1	Smooth	5.5 x 4 x 0.25	
2	Rough	6 x 4 x 3	
3	Rough	4 x 4 x 3	
4	Smooth	2.5 x 3 x 0.7	X
5	Smooth	2.5 x 3 x 2.5	
6	Smooth	4.5 x 6 x 0.5	X
7	Smooth	3 x 4 x 0.5	
8	Smooth	4 x 4 x 0.4	
9	Rough	2 x 3.5 x 2	X
10	Rough	3 x 5 x 2.5	X
11	Rough	2.5 x 3 x 2.5	
12	Smooth	3.5 x 5.5 x 0.5	
13	Smooth	4 x 6.5 x 0.5	
14	Rough	2.5 x 5.25 x 3	X
15	Rough	4.5 x 4.5 x 1	X
16	Rough	4 x 3.5 x 2.5	
17	Smooth	1.5 x 3 x 1.5	
18	Rough	3.5 x 7 x 2.5	
19	Smooth	6.5 x 7 x 0.5	
20	Rough	3 x 3 x 2.5	
21	Smooth	16 x 18 x 1	X
22	Rough	8 x 7 x 2	
23	Rough	7 x 9 x 2	
24	Rough	6 x 8 x 2	X
25	Rough	7 x 9 x 2	X

Figure 30. Sample 4, top view

Sample 31. Sample 6, bottom view.

Figure 32. Sample 9, top view.

Figure 33. Sample 10, side C.

Figure 34. Sample 14, side C.
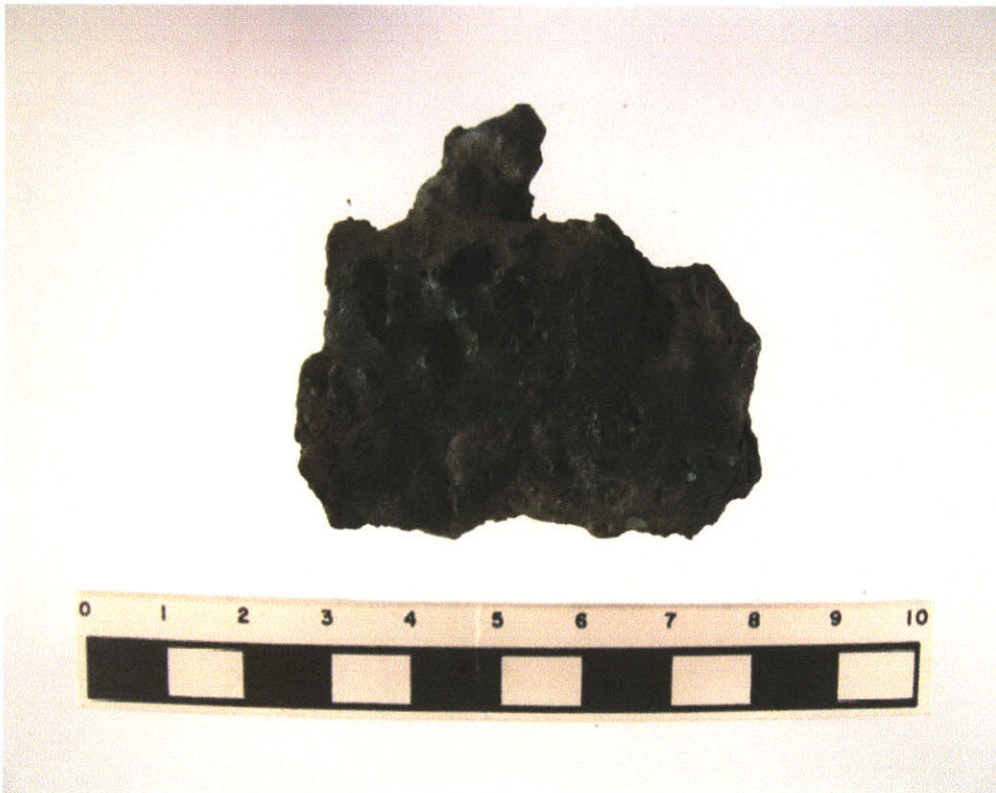
Figure 35. Sample 15, bottom view.

Figure 36. Sample 21, top view.

Figure 37. Sample 24, top view.

Figure 38. Sample 25, top view.

Appendix C: Slag Sample Photomicrographs

This appendix provides a selection of photomicrographs from the El Manchon slags used in this research.
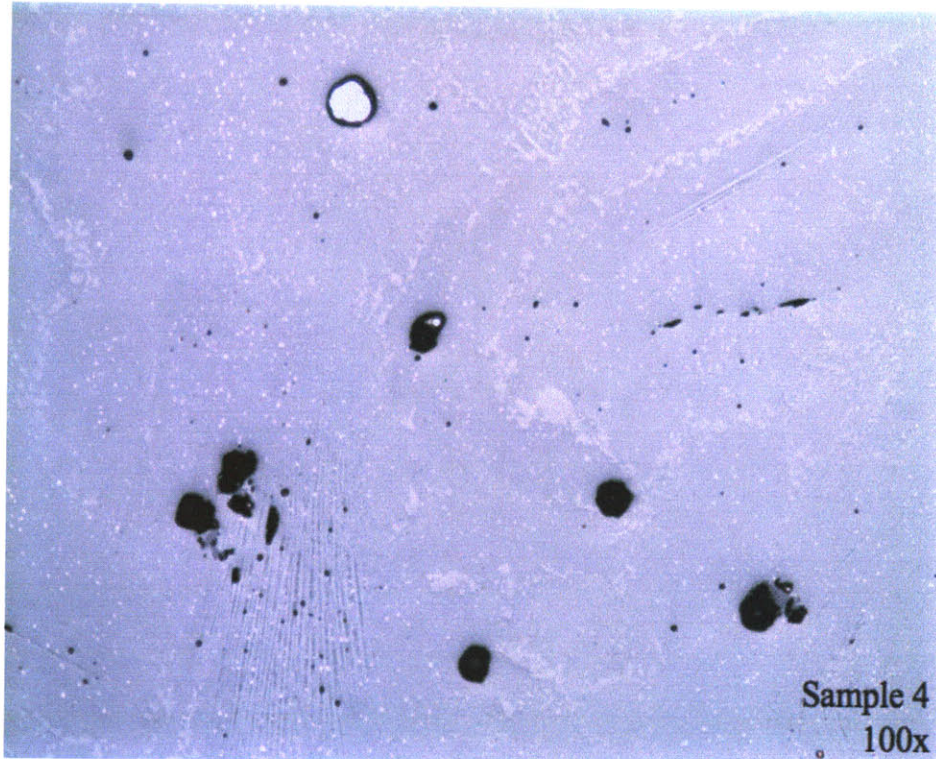
Figure 39. A photomicrograph of a smooth slag. The main phase present is the silicon-melt phase.
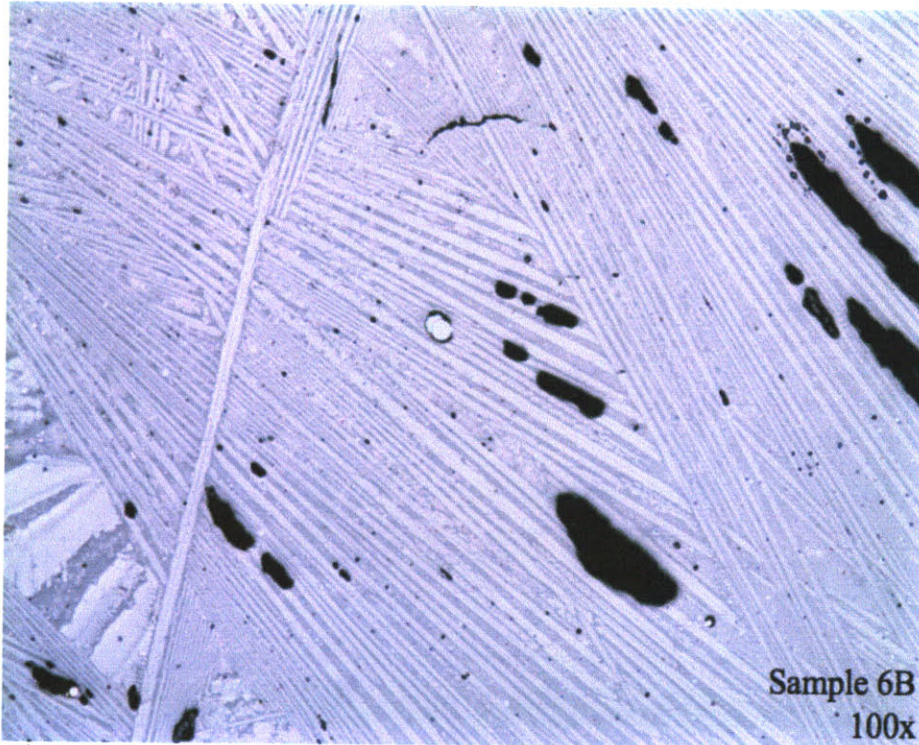
Figure 40. A photomicrograph of a smooth slag. The main phase present is the silicon-melt phase.
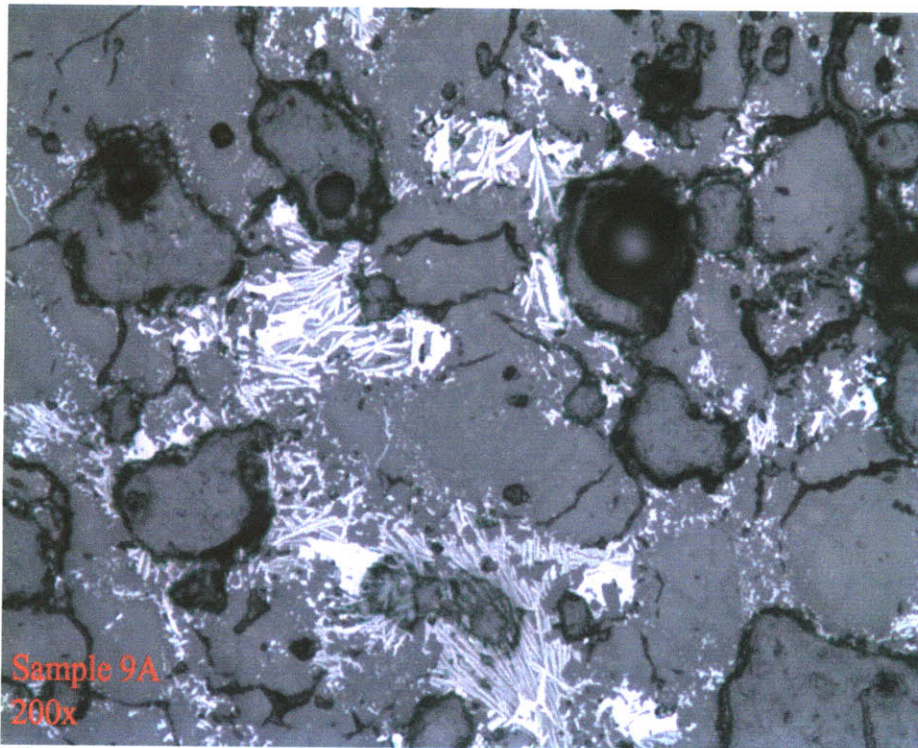
Figure 41. Photomicrograph of a rough slag. The cracks of the quartz-like phase are filled with silicon-melt phase.
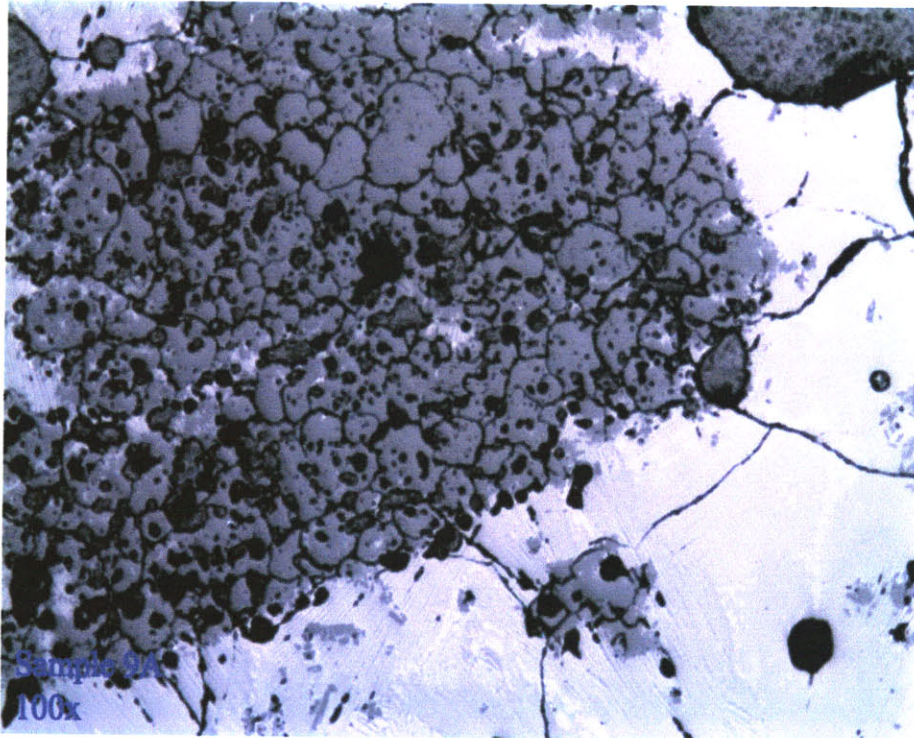
Figure 42. Photomicrograph of a rough slag. The quartz-like phase and the silicon-melt phase are present.
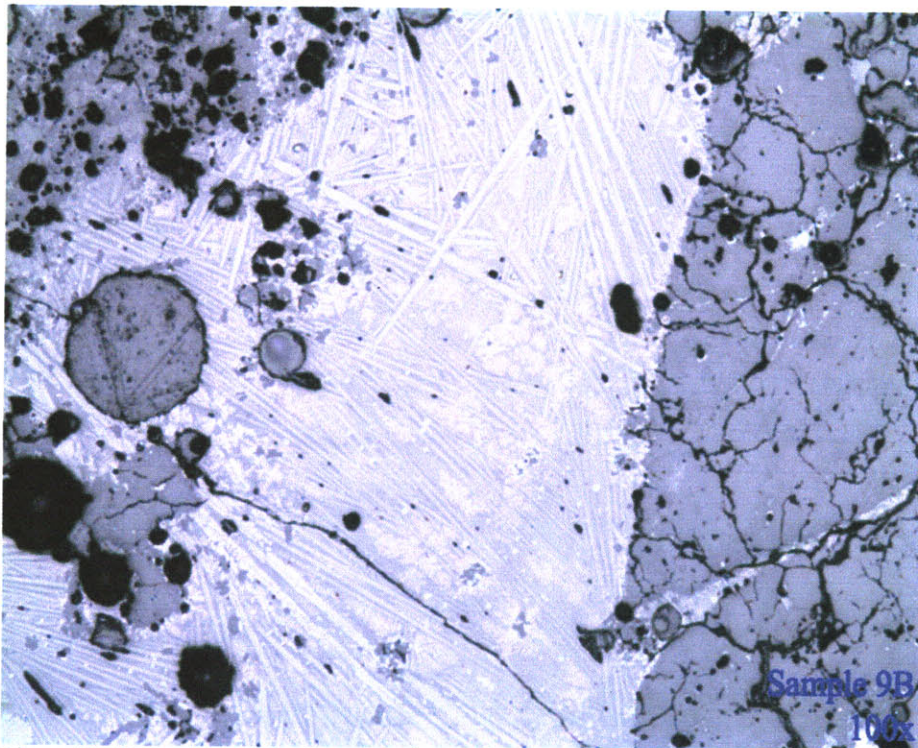
Figure 43. Photomicrograph of a rough slag. Silicon-melt phase and quartz-like phase present.
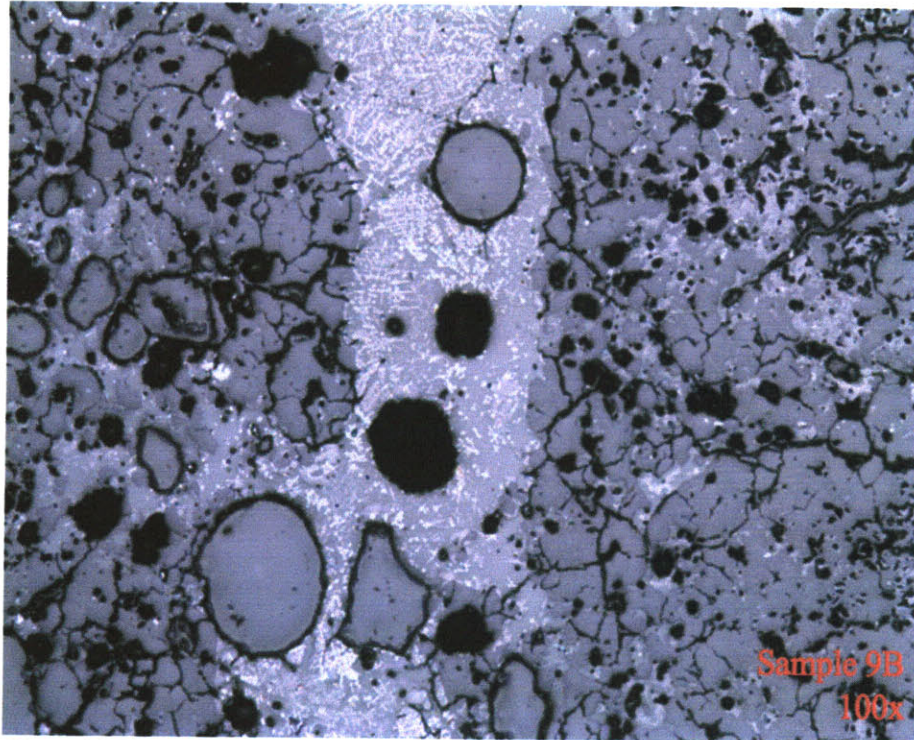
Figure 44. Photomicrograph of a rough slag. Dendritic growth is visible in the silicon-melt phase.
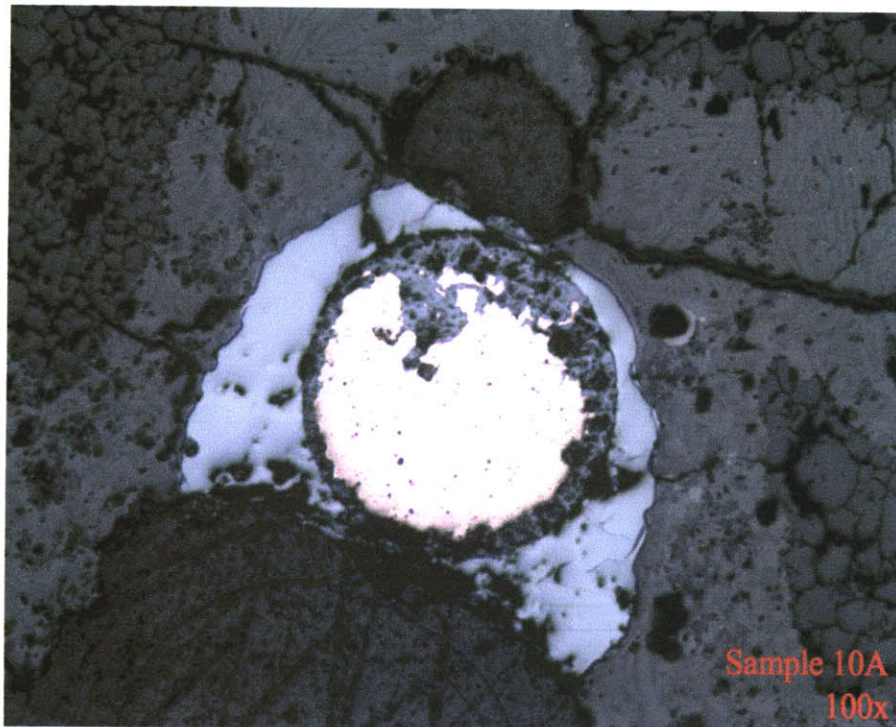
Figure 45. Photomicrograph of a rough slag. This sample has a predominant copper prill and surrounding copper-iron-sulfide matte.

70
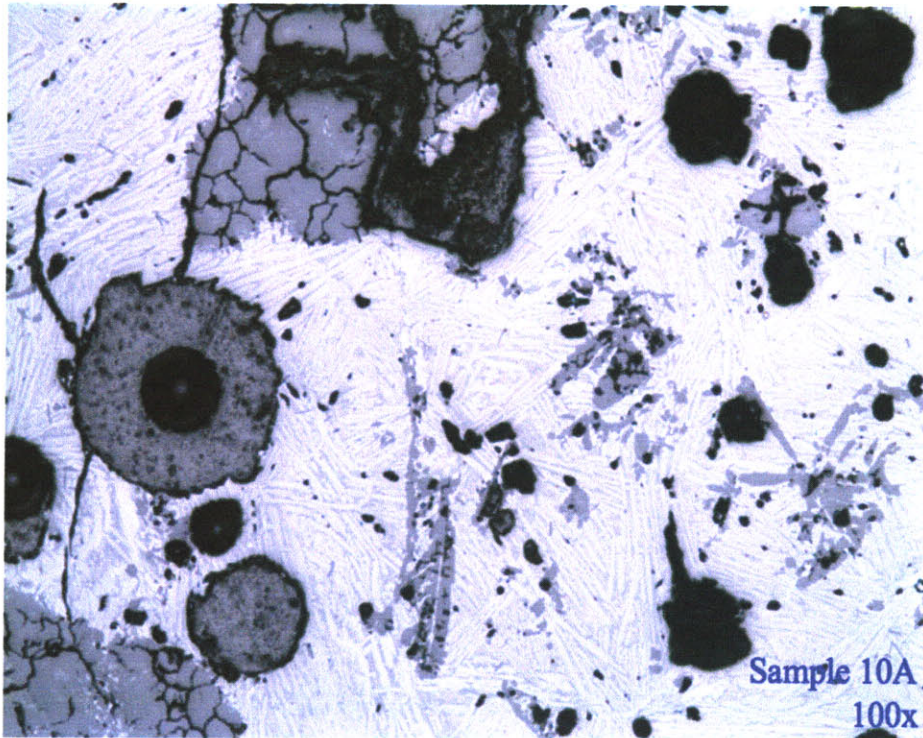
Figure 46. Photomicrograph of a rough slag. The silicon-melt phase and quartz-like phase are prominent.
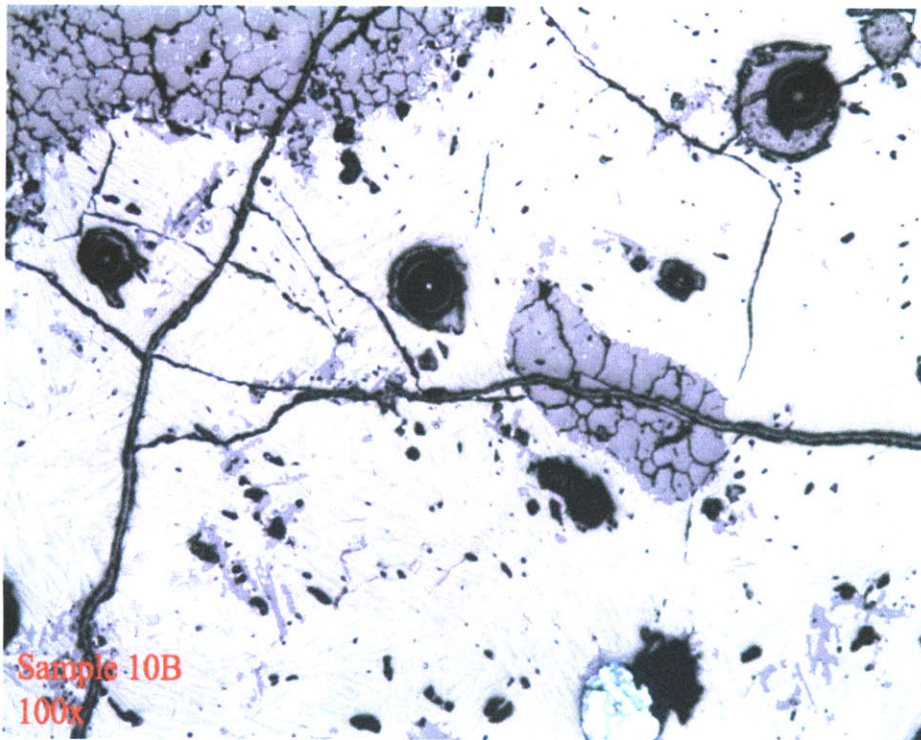
Figure 47. A photomicrograph of a rough slag. A copper-iron-sulfide prill is visible in the lower right.
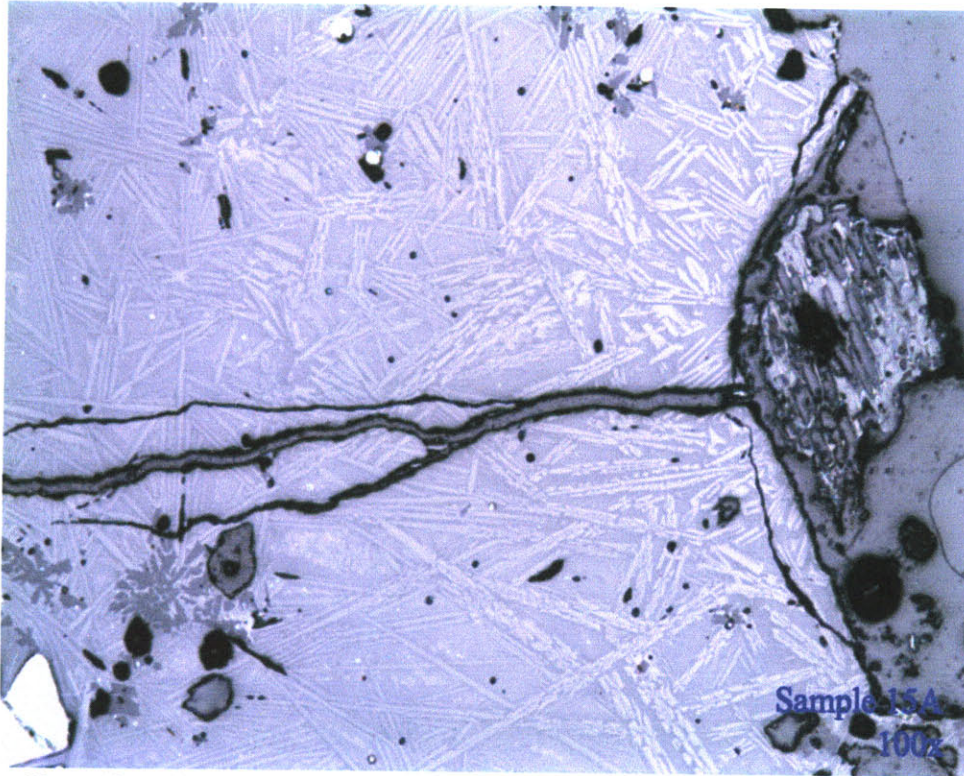
Figure 48. A photomicrograph of a rough slag. The silicon-melt phase is prominent.
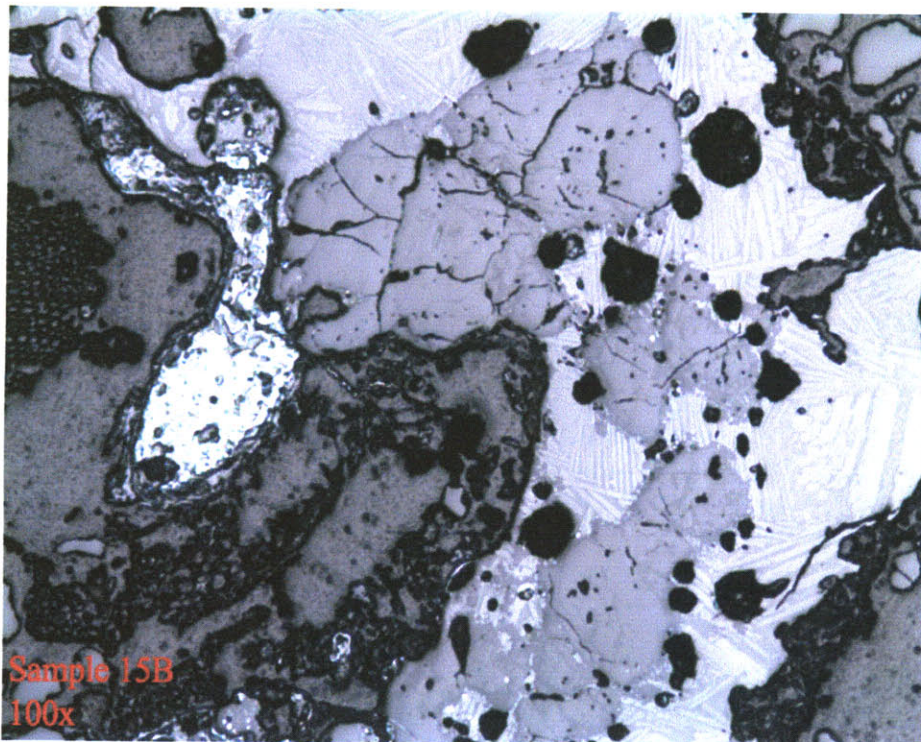
Figure 49. A photomicrograph of a rough slag, showing the quartz-like phase, silicon-melt phase, and copper-iron-sulfide phase.
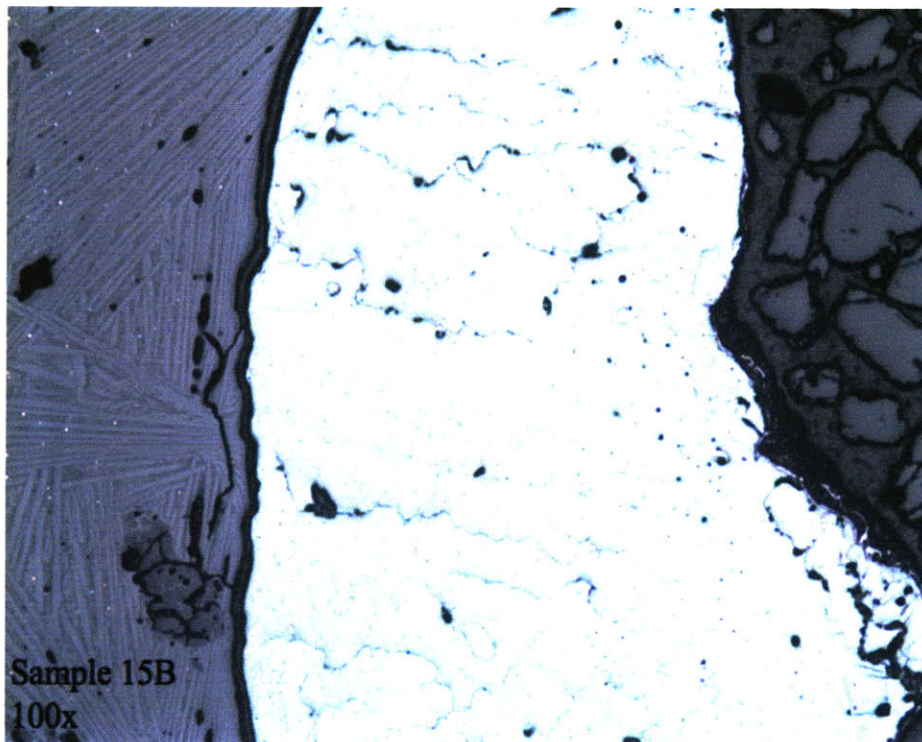
Figure 50. Photomicrograph of a rough slag. An usually large copper-iron-sulfide phase is visible.

Appendix D: Electron Beam Microprobe Data

Table 8. Summary of data points analyzed by electron beam microprobe.

Probe Sample Number	Phase Analyzed	Beam Size (microns)
22.1.1	Metal Phase	1
22.2.1	Silicon-melt Phase	20
22.2.2	Silicon-melt Phase	10
22.2.3	Silicon-melt Phase	30
22.2.4	Quartz-like Phase	10
22.2.5	Quartz-like Phase	30
22.3.1	Epoxy Bubble	10
22.3.2	Epoxy Bubble	20
22.4.1	Metal Phase	1
22.5.1	Metal Phase	1
23.1.1	Silicon-melt Phase	10
23.1.2	Silicon-melt Phase	20
23.1.3	Metal Phase	1
23.2.1	Metal Phase	1
23.2.2	Quartz-like Phase	10
23.2.3	Quartz-like Phase	30
24.1.1	Metal Phase	1
24.1.2	Silicon-melt Phase	10
24.1.3	Quartz-like Phase	10
24.1.4	Quartz-like Phase	30
24.2.1	Metal Phase	1
24.3.1	Metal Phase	1
25.1.1	Silicon-melt Phase	10
25.1.2	Metal Phase	1
25.1.3	Quartz-like Phase	10
25.2.1	Metal Phase	1
25.2.2	Metal Phase	1

30μm
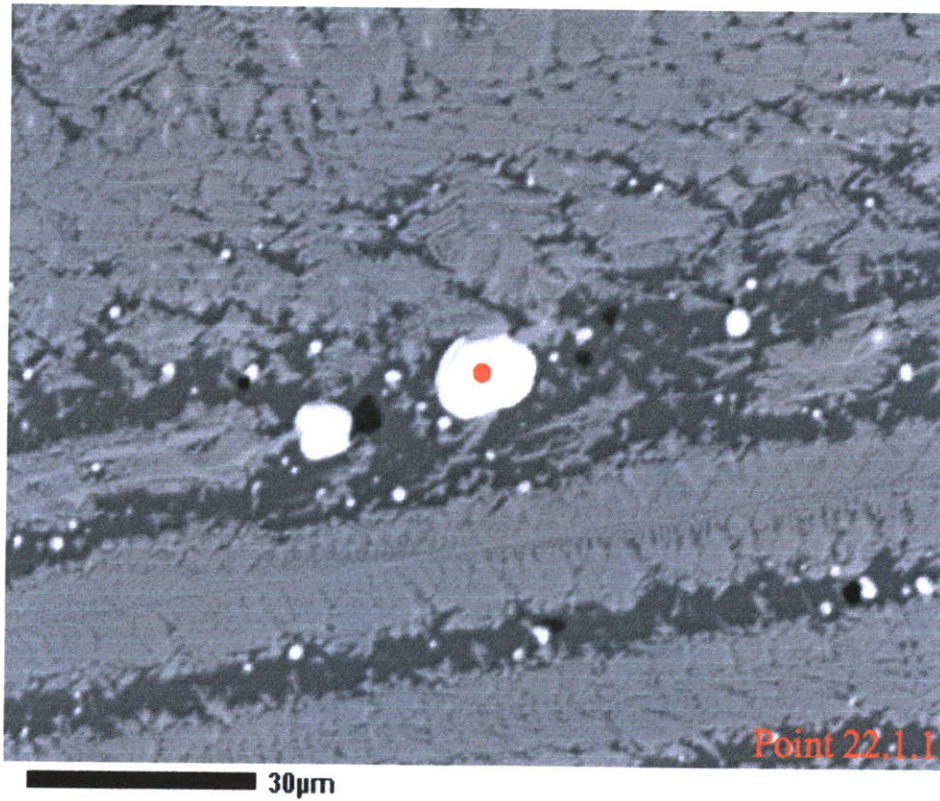
BSE spot22p1

Figure 51. Photomicrograph of Sample 22, frame 1. Copper-iron-sulfide phase identified by red point.
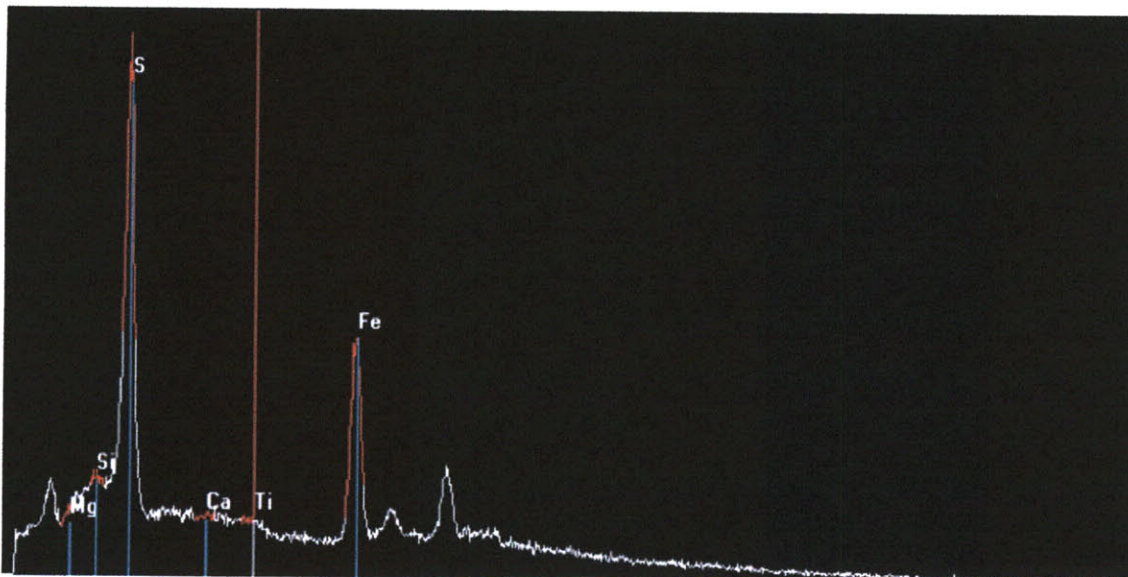
Figure 52. EDS spectrum for Point 22.1.1. Sulfur, copper, and iron are the major constituents.
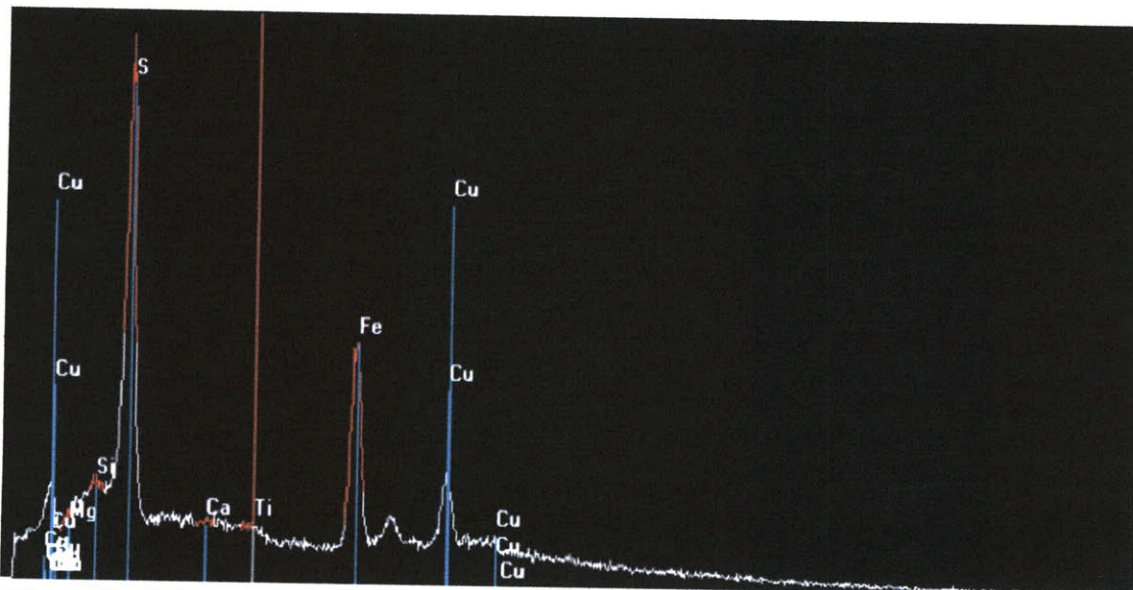
Figure 53. EDS spectrum of Point 22.1.1 with characteristic Cu peaks identified.
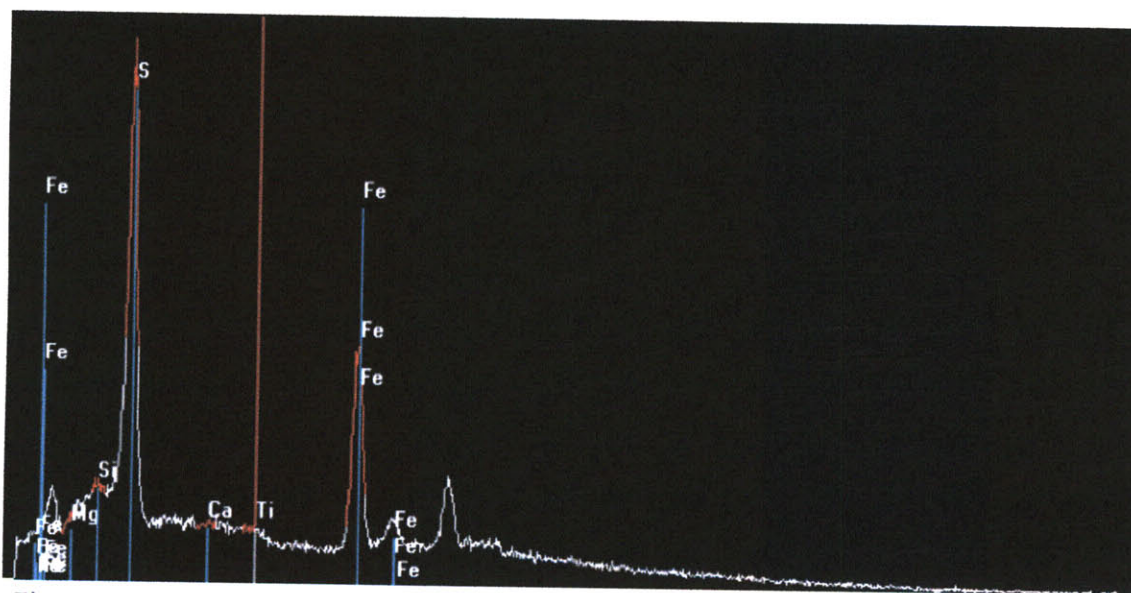
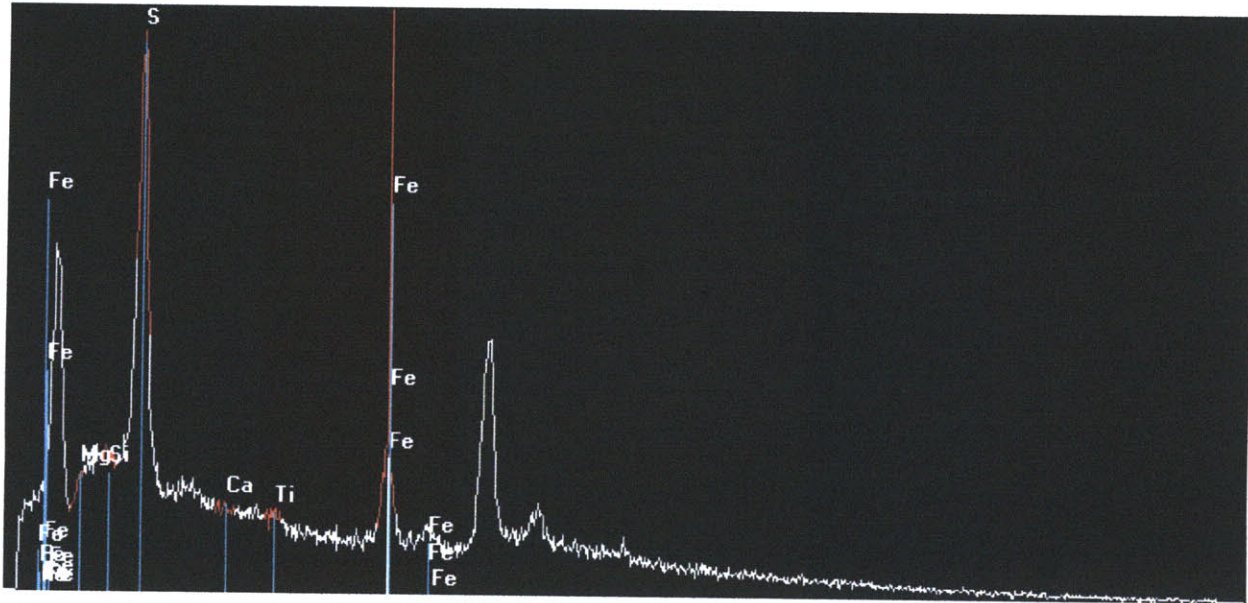Figure 54. EDS spectrum of Point 22.1.1 with characteristic Fe peaks identified.
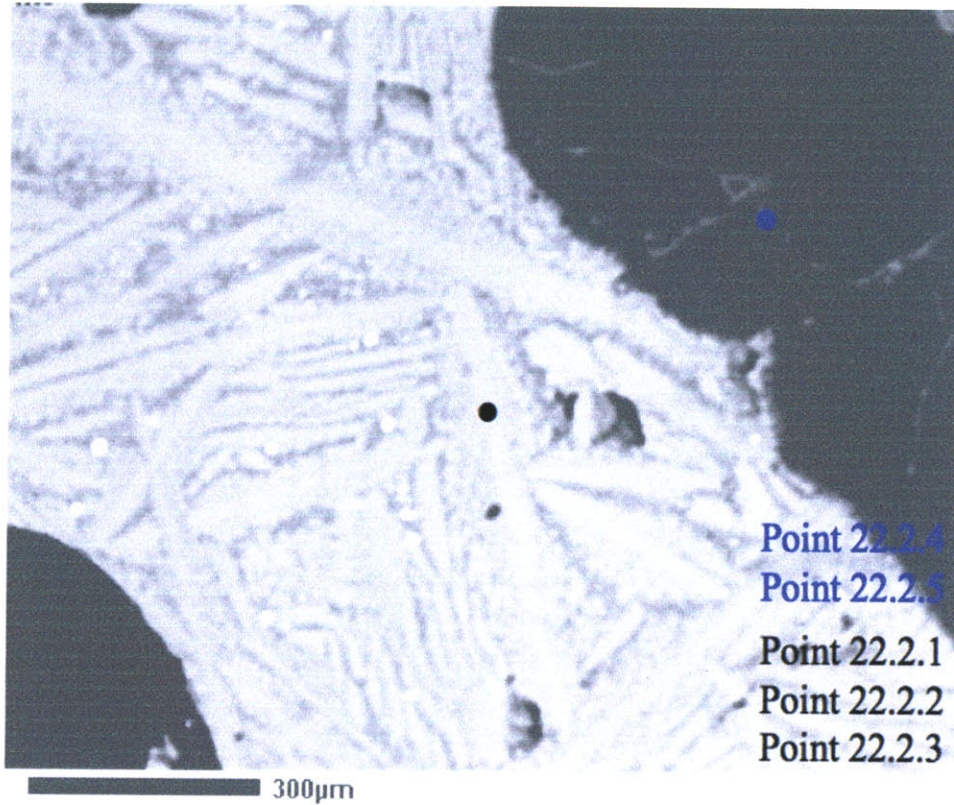
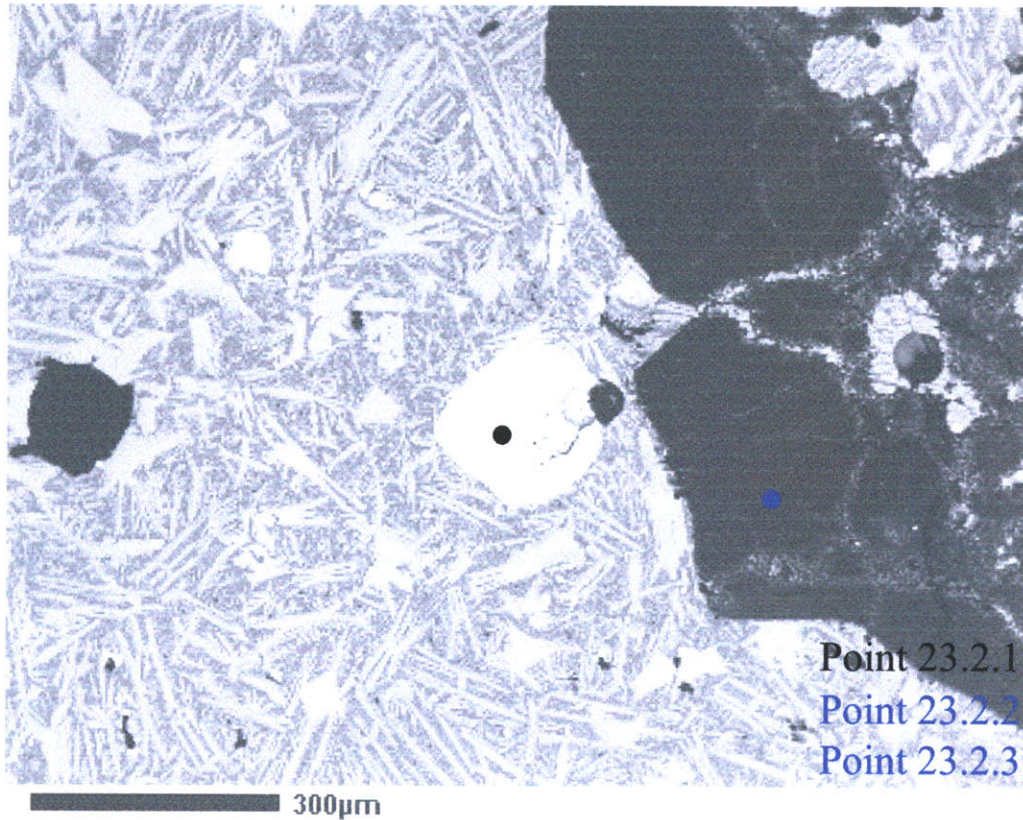BSE spot22p2

Figure 55. Photomicrograph of Sample 22, frame 2. Silicon-melt phase
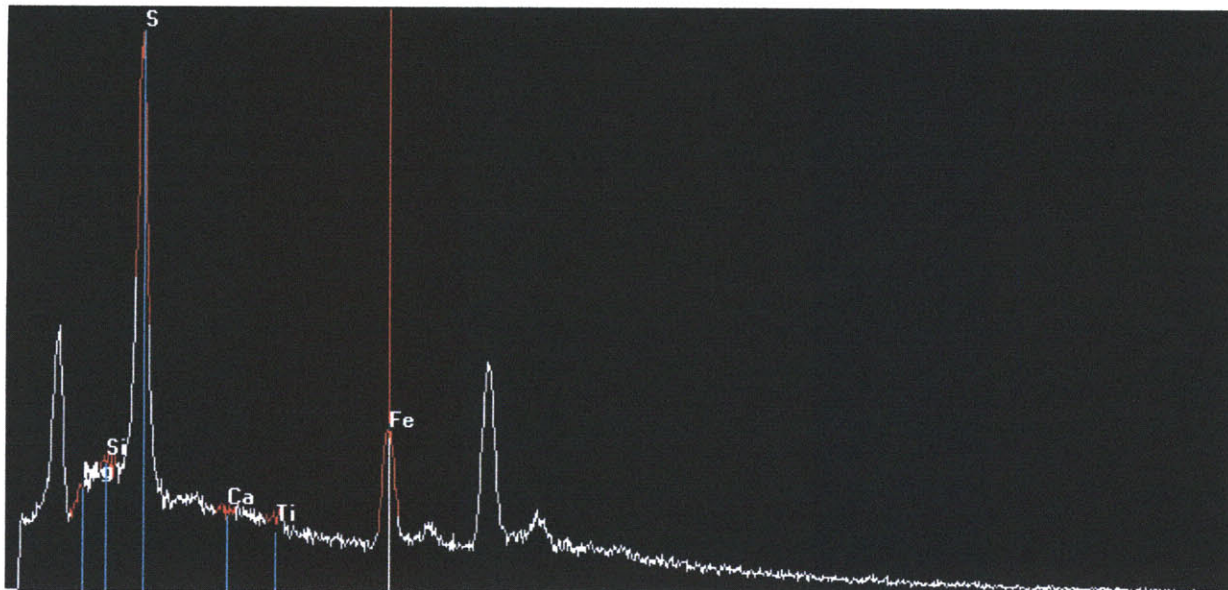identified by black point; quartz-like phase identified by blue point.
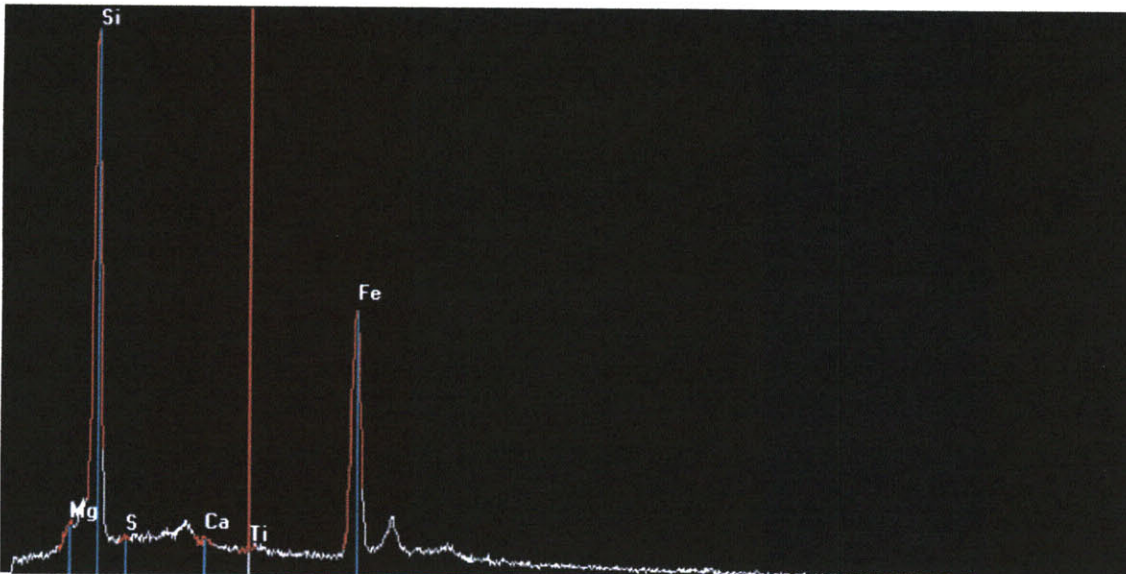
Figure 56. EDS spectrum of Point 22.2.1. Silicon and iron are the main constituents.
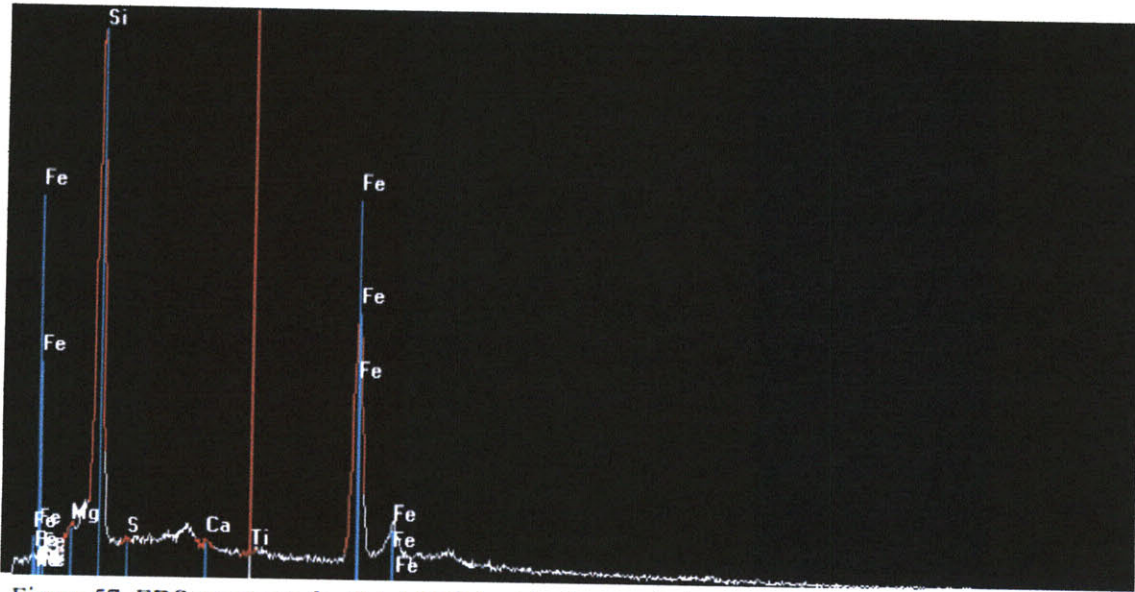
Figure 57. EDS spectrum for Point 22.2.1 with characteristic Fe peaks identified.
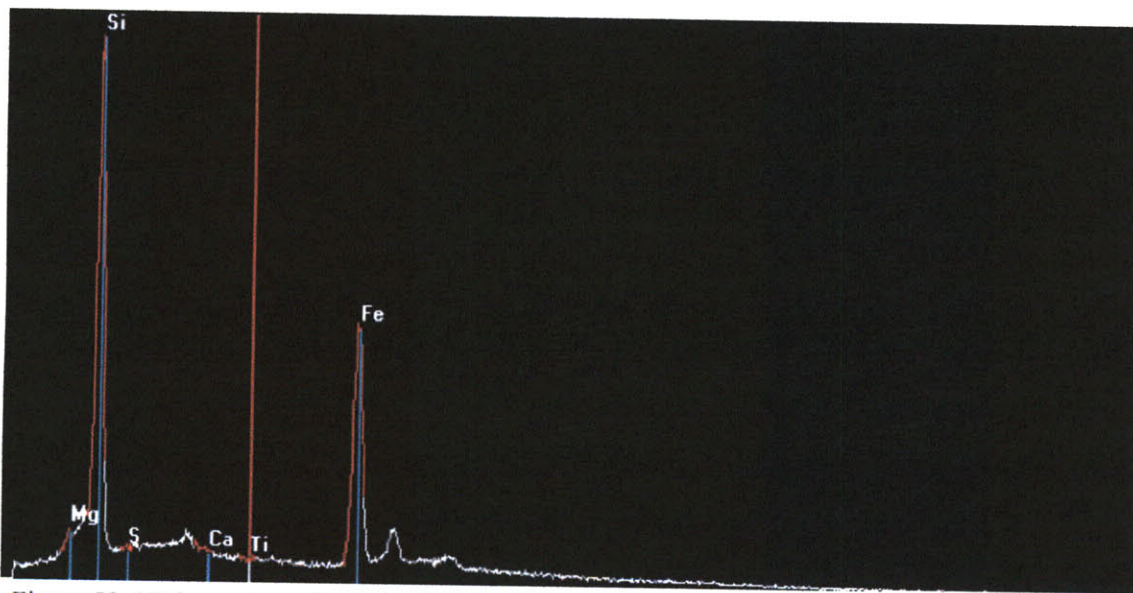
Figure 58. EDS spectrum for Point 22.2.2. Silicon and iron are the main constituents.
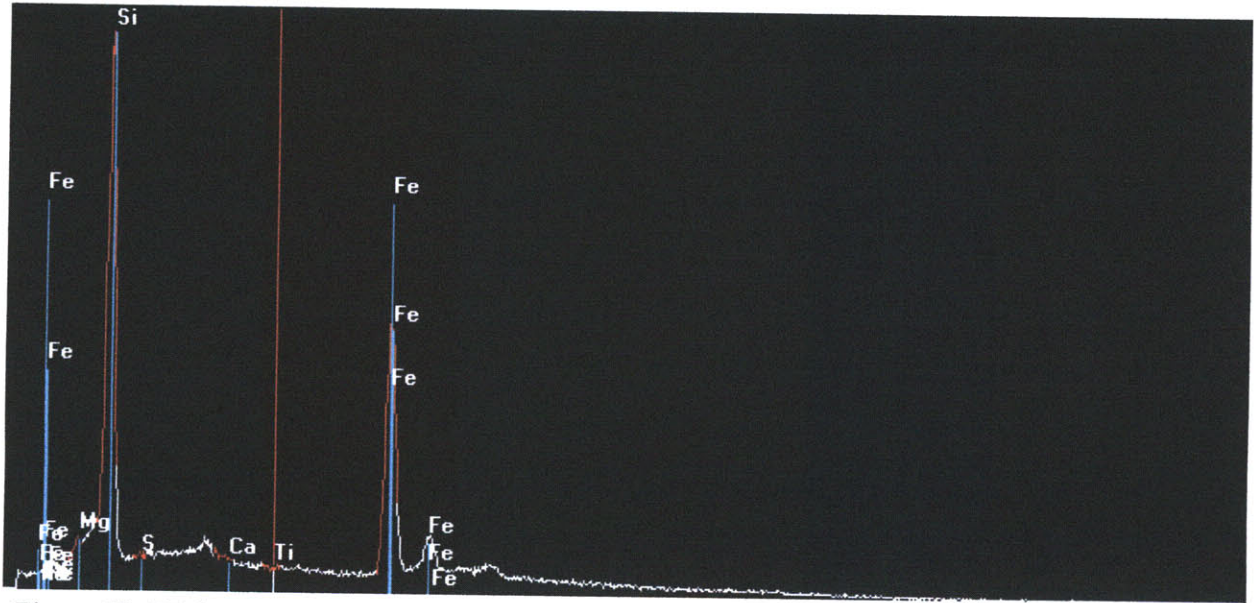
Figure 59. EDS spectrum for Point 22.2.2 with characteristic Fe peaks identified.
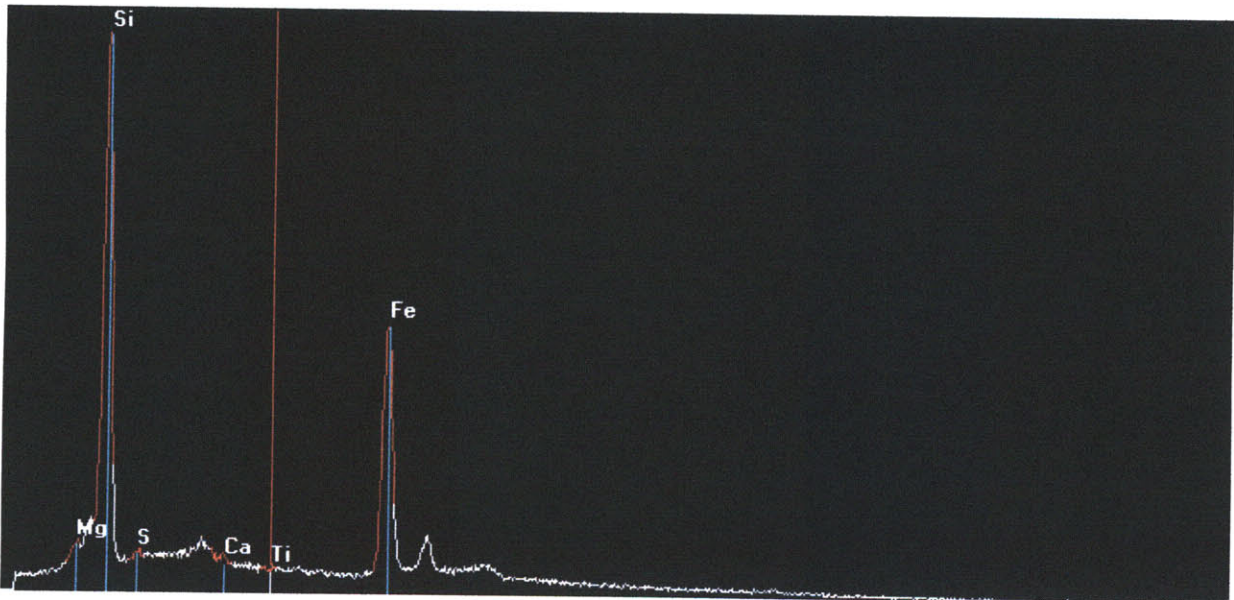
Figure 60. EDS spectrum for point 22.2.3. The main constituents are silica and iron.
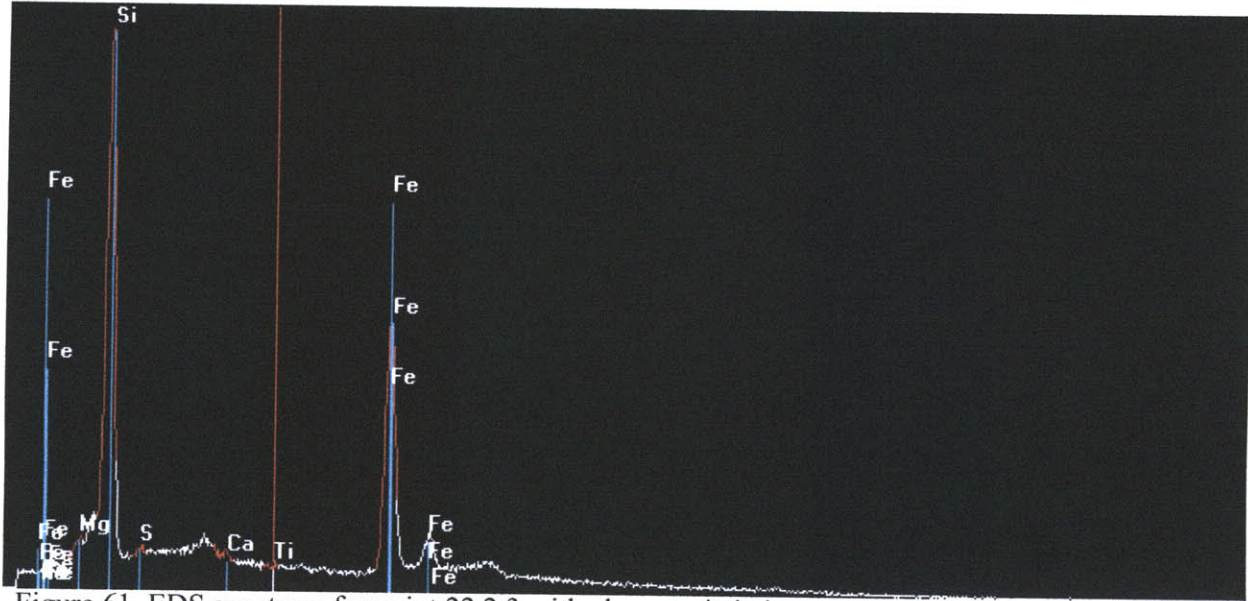
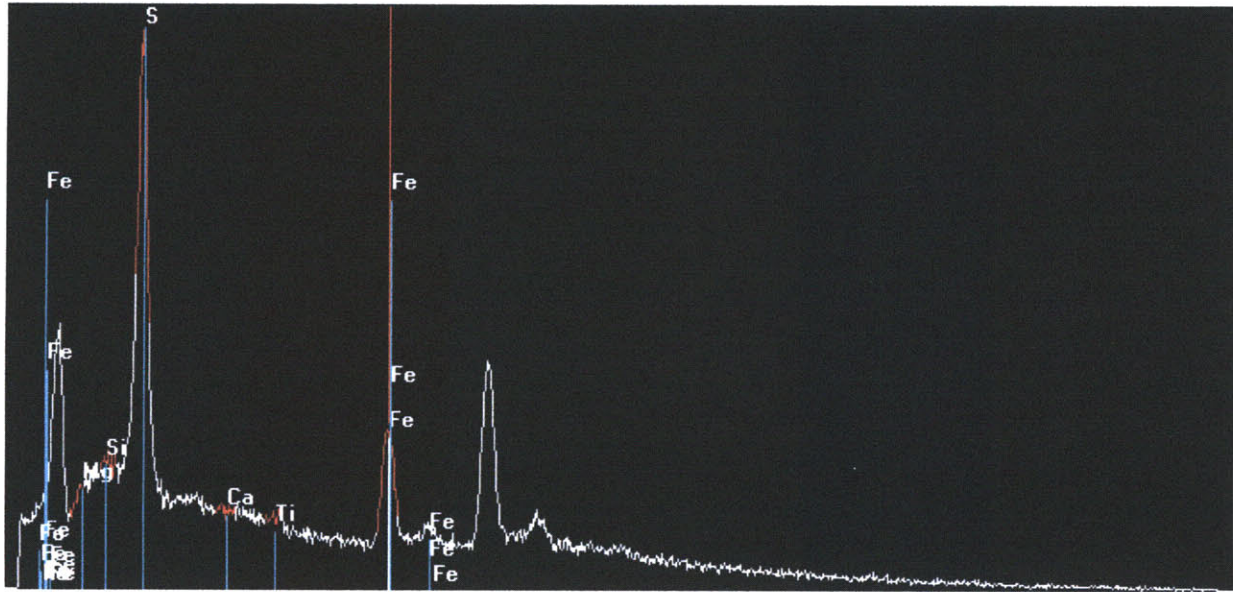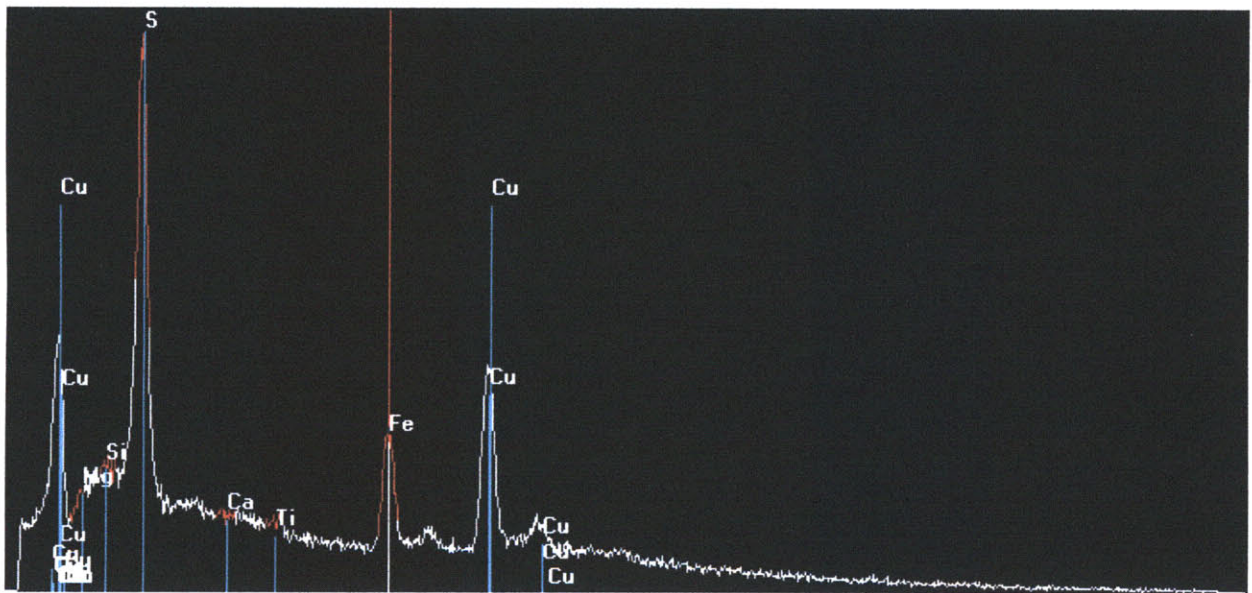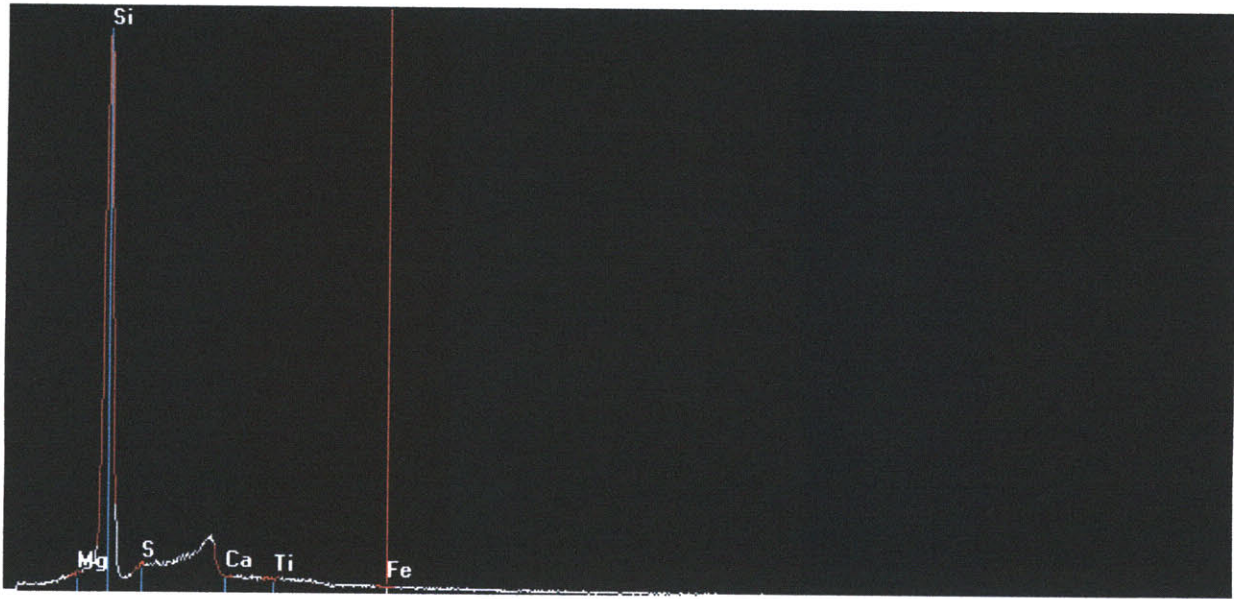Figure 61. EDS spectrum for point 22.2.3 with characteristic iron peaks identified.
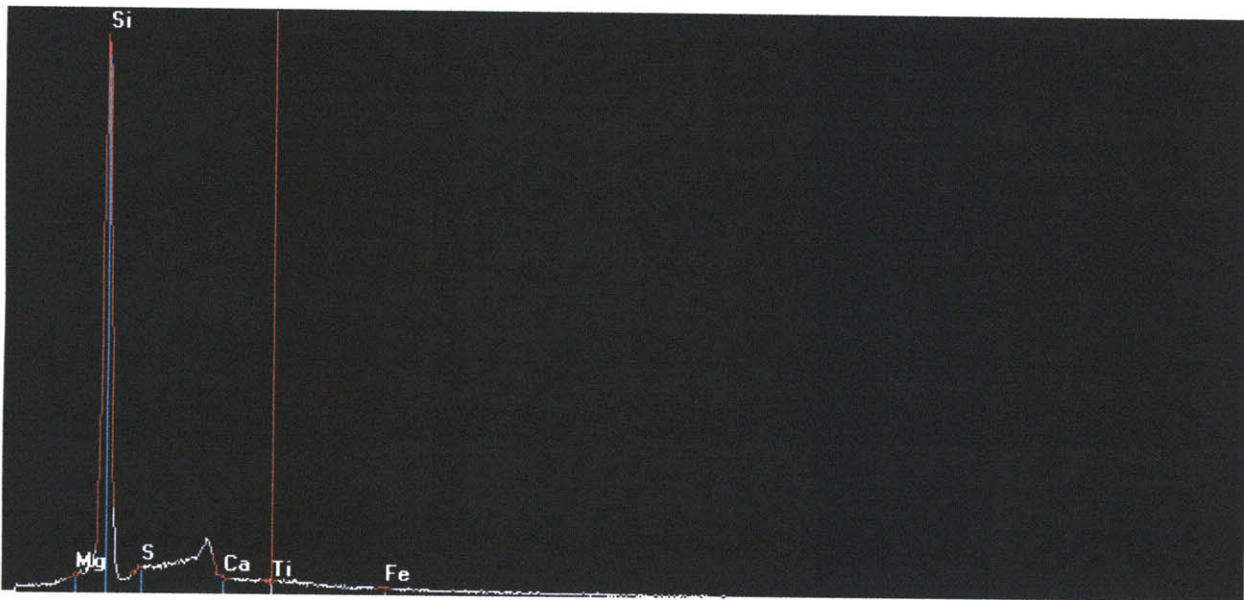
Figure 62. EDS spectrum for point 22.2.4. The primary constituent is silica.
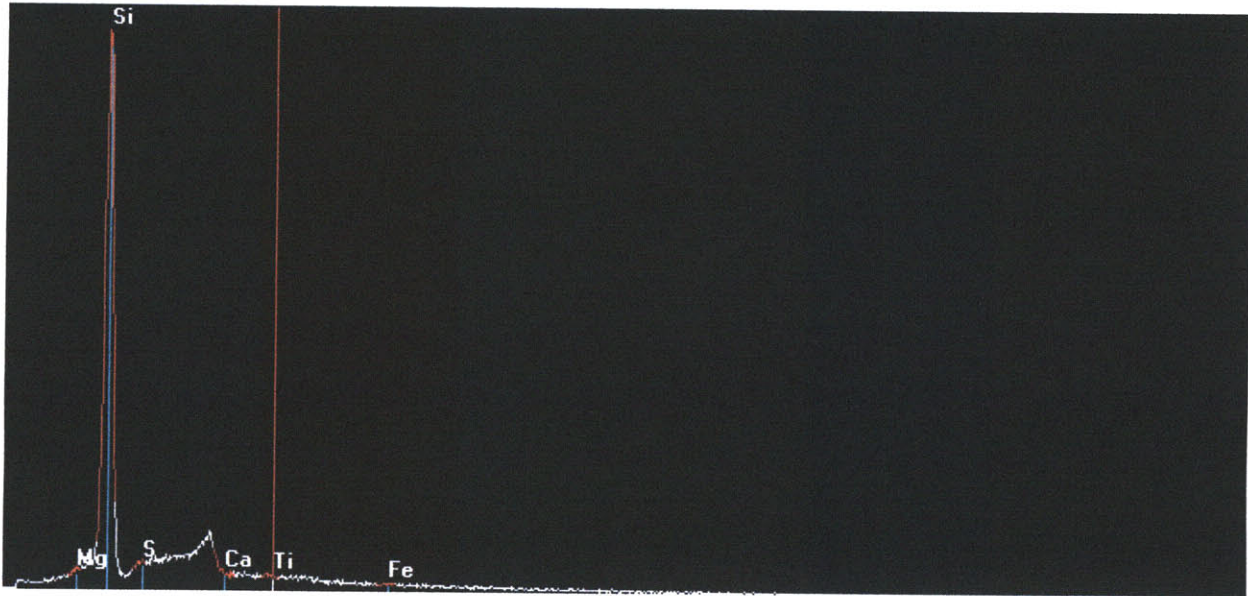
Figure 63. EDS spectra for point 22.2.5. The primary constituent is silica.
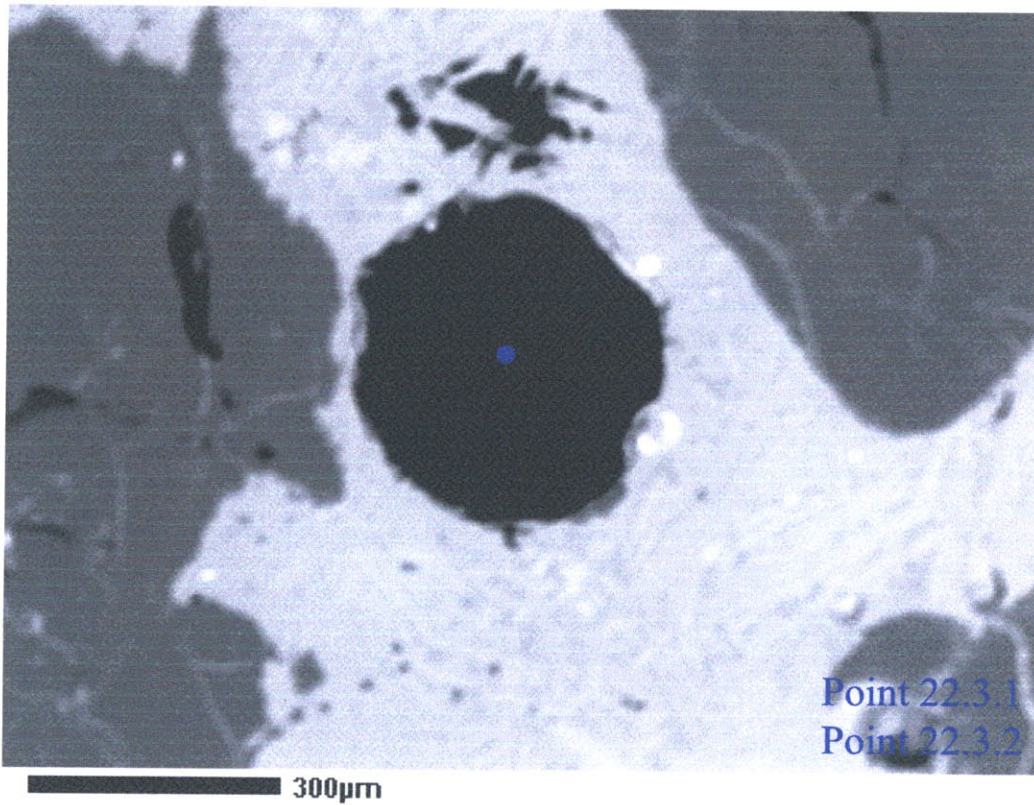
BSE spot22p3

Figure 64. Photomicrograph of Sample 22, frame three. An epoxy zone is identified by the blue point.
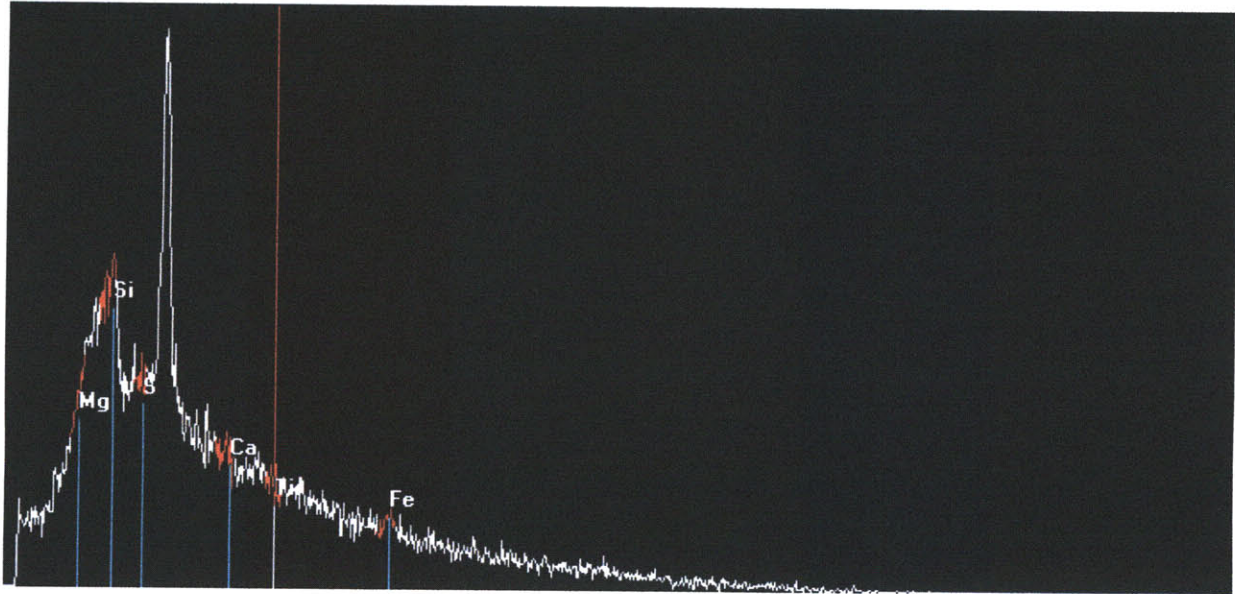
Figure 65. EDS spectrum for 22.3.1. Chlorine and silica are major constituents.
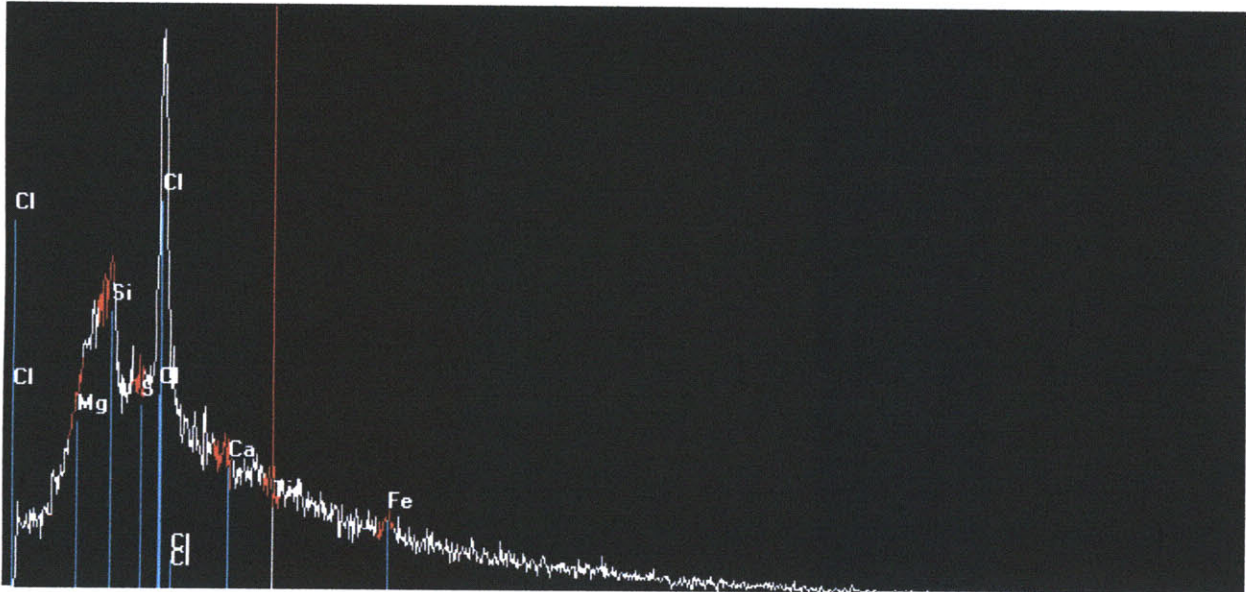
Figure 66. EDS spectrum for point 22.3.1 with characteristic chlorine peaks identified.
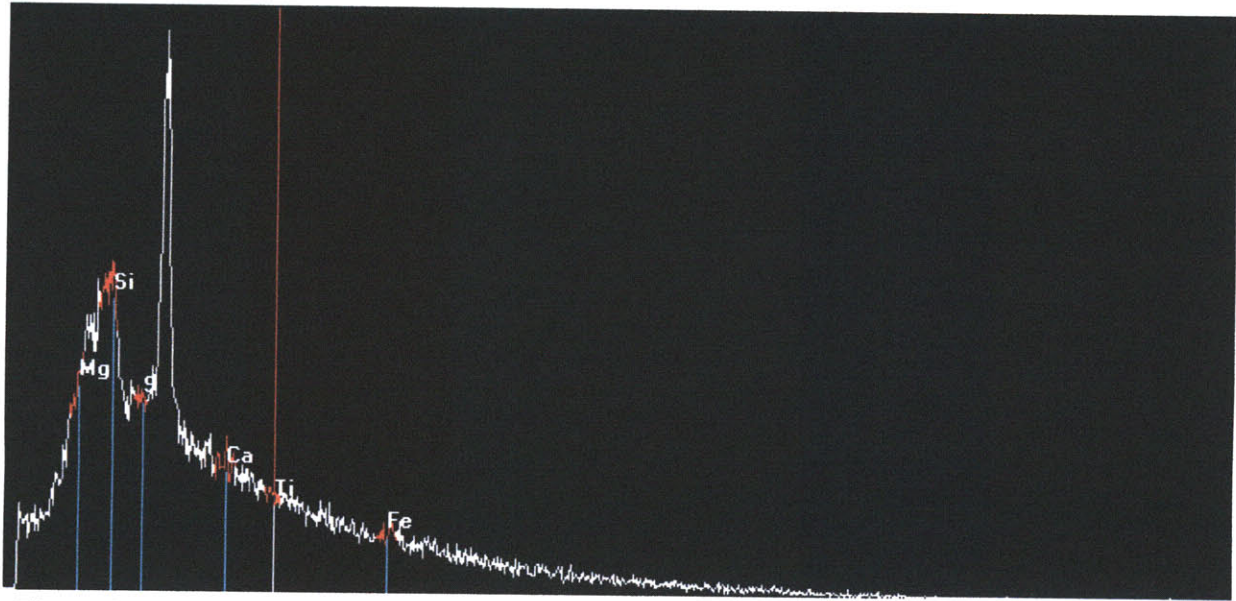
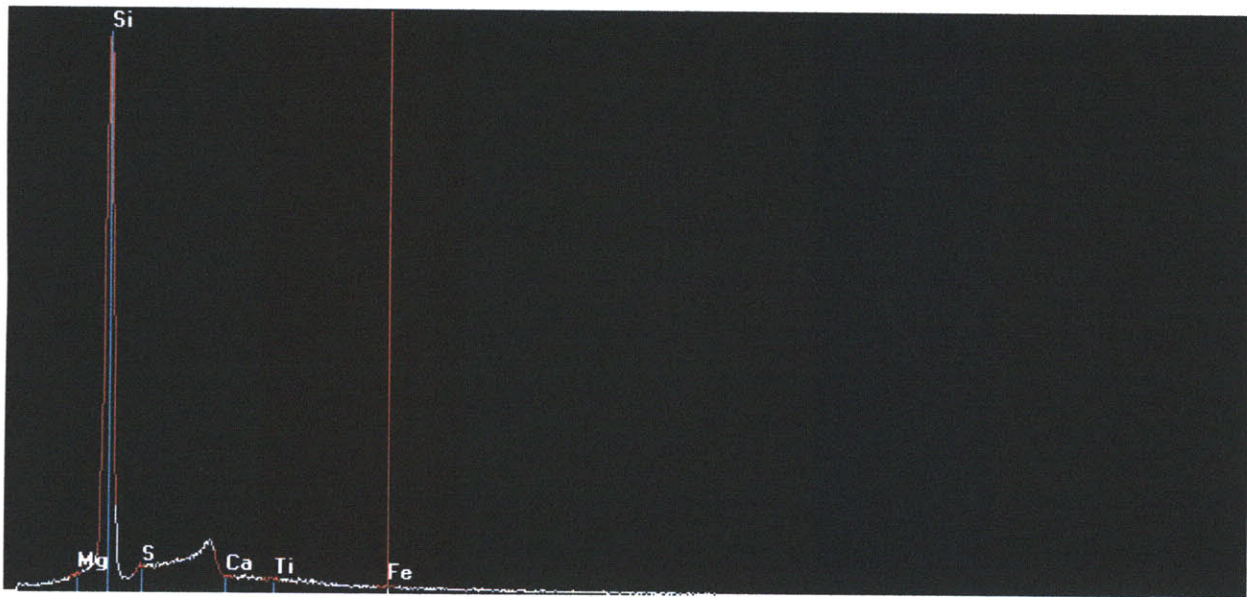Figure 67. EDS spectrum of point 22.3.2. The major constituents are chlorine and silica.
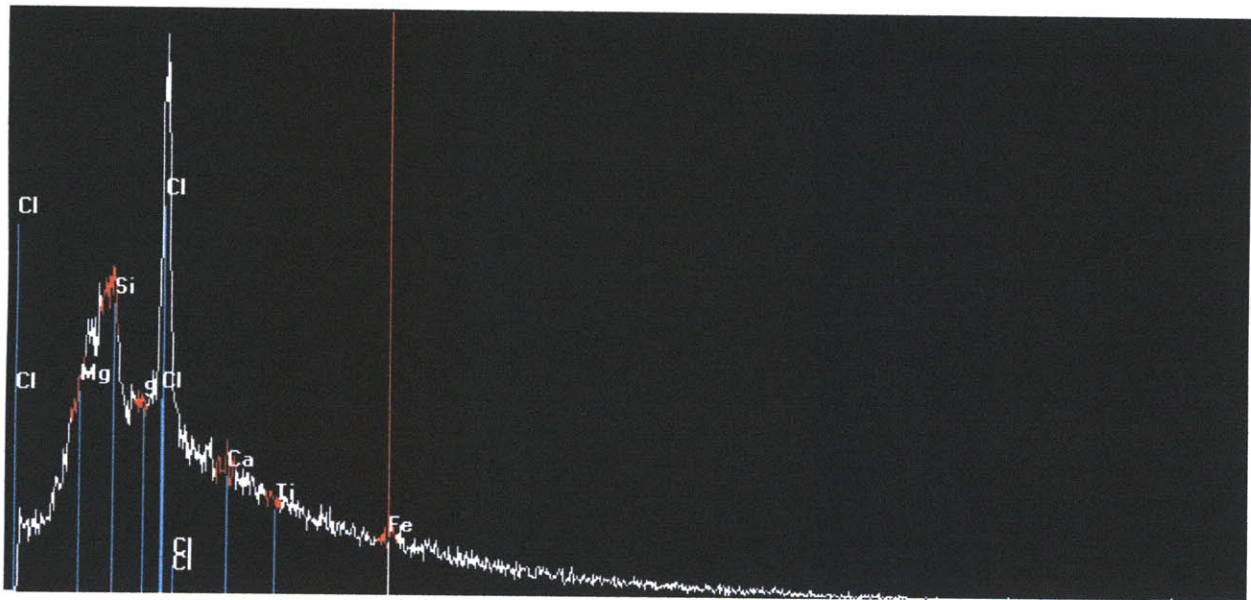
Figure 68. EDS spectrum of point 22.3.2 with characteristic chlorine peaks.
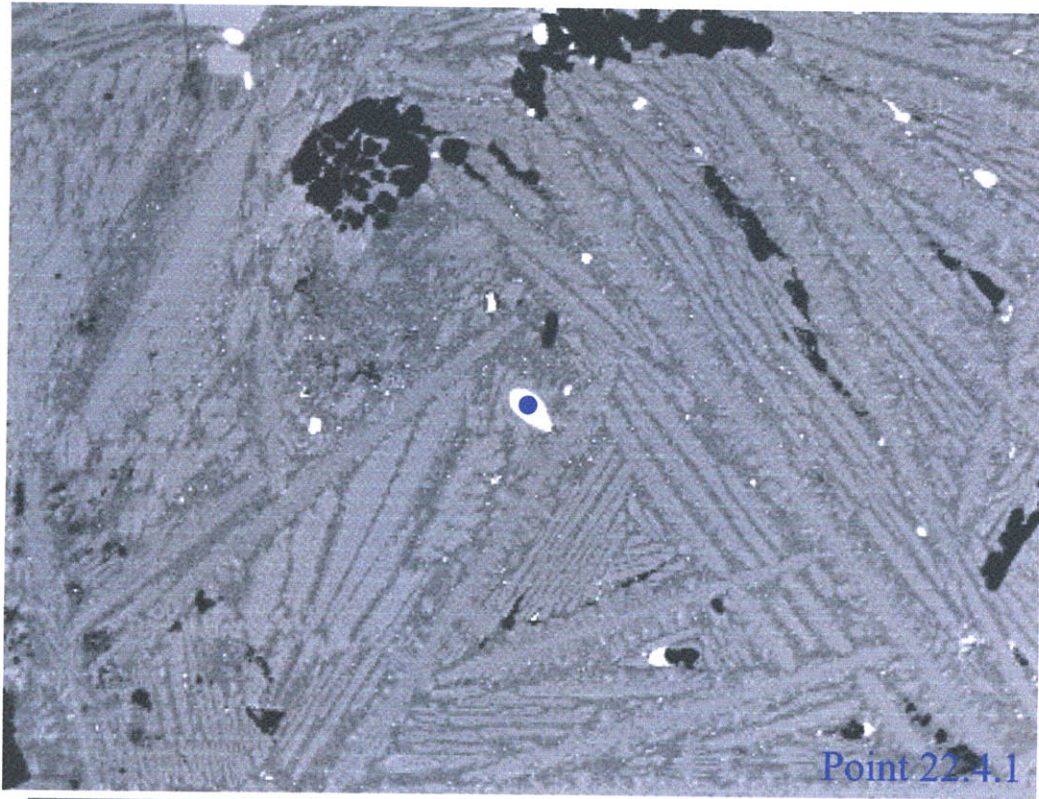
Figure 69. Photomicrograph of Sample 22, frame 4. Copper-iron-sulfide phase identified by blue point.
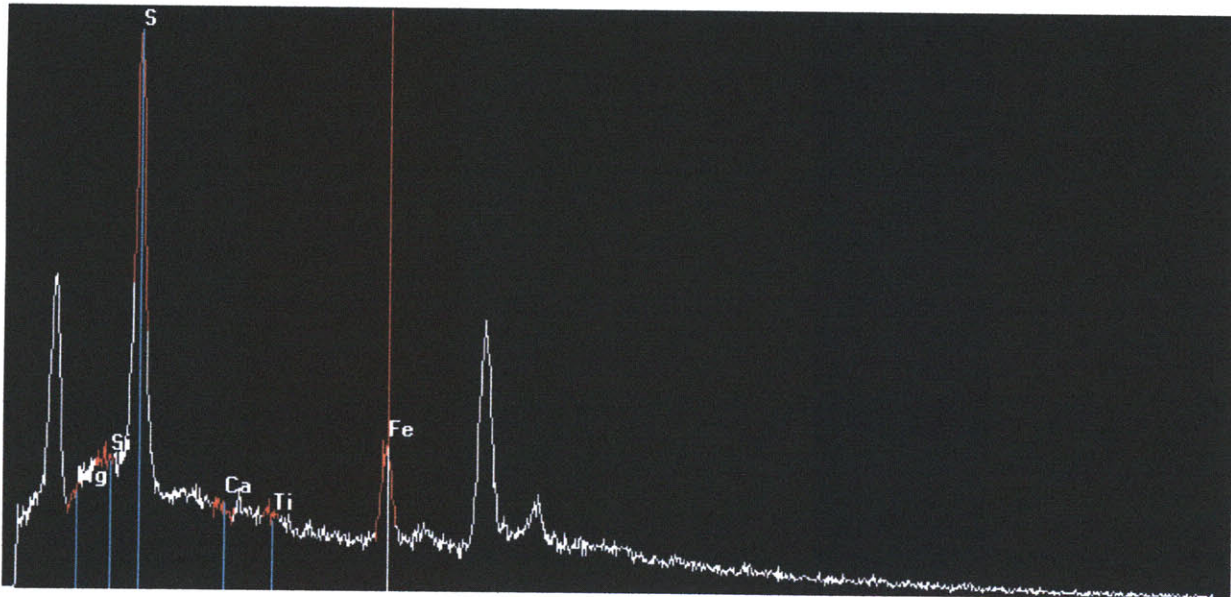
Figure 70. EDS spectrum for point 22.2.4. Copper, iron, and sulfur are the main constituents.
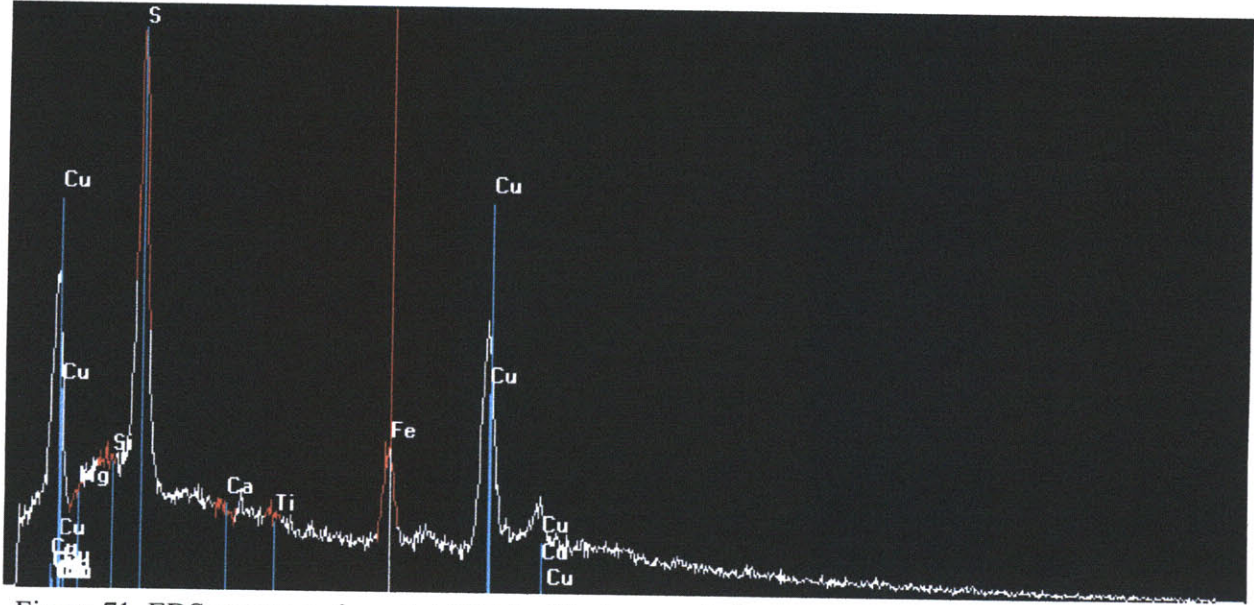
Figure 71. EDS spectrum for point 22.2.4 with characteristic copper peaks identified.

BSE spot22p5
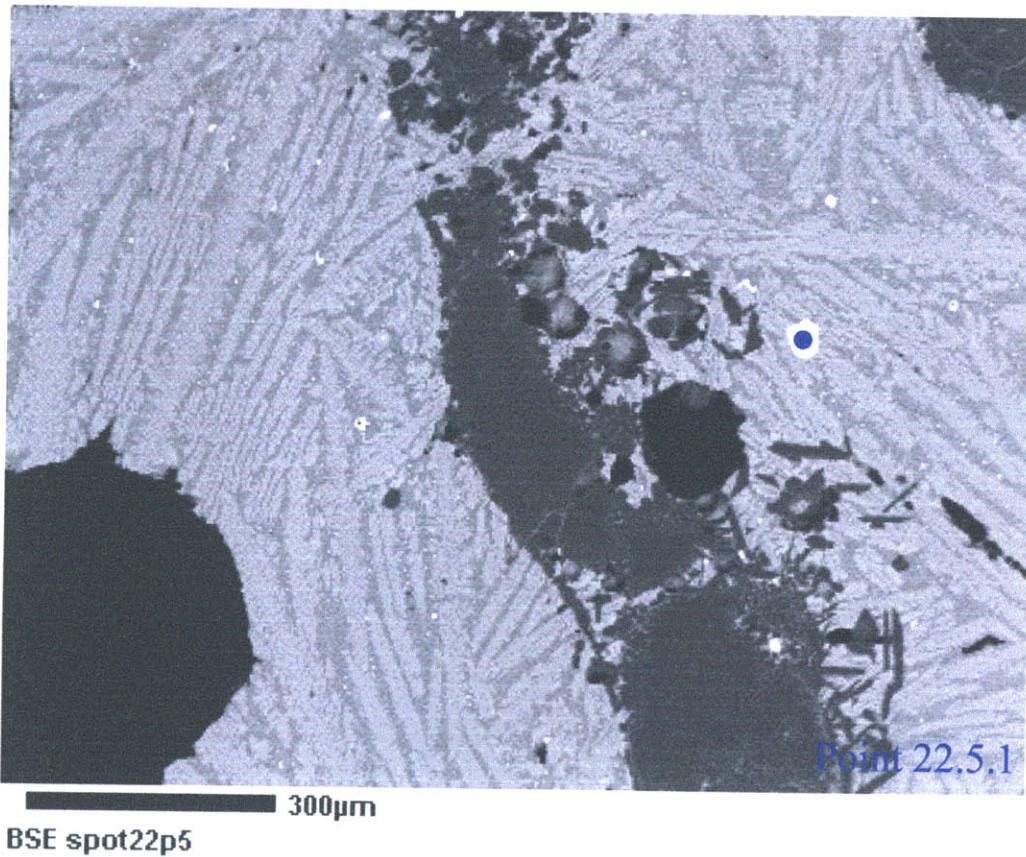
Figure 72. A photomicrograph of Sample 22, frame 5. Copper-iron-sulfide phase identified by blue point.
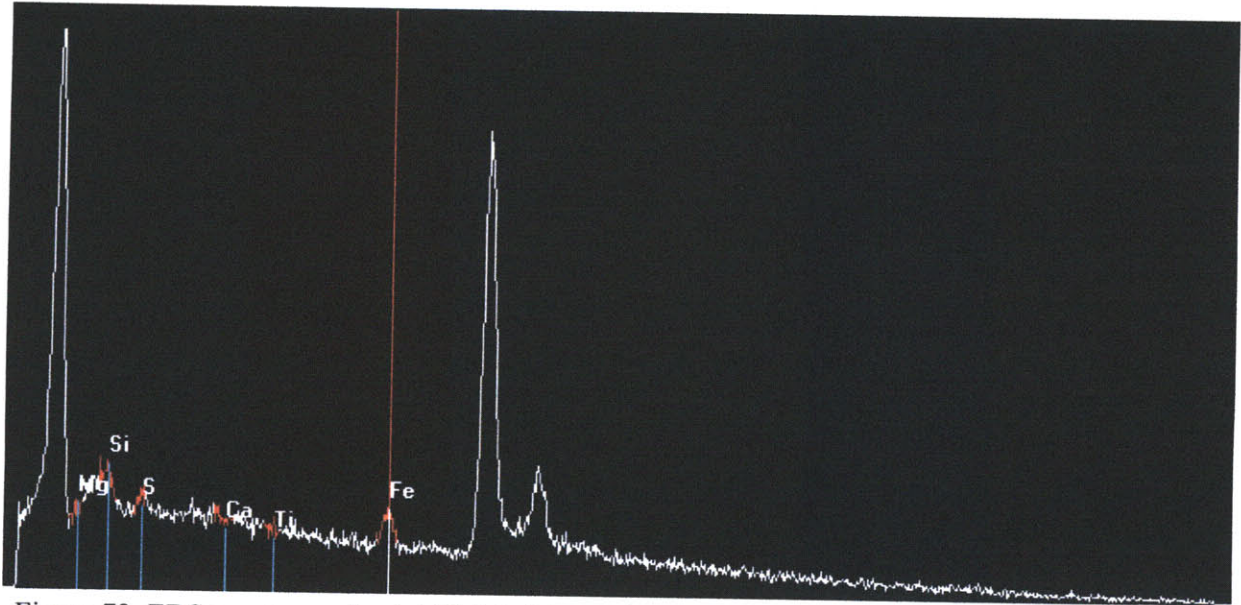
Figure 73. EDS spectrum of point 22.5.1. The main constituents are iron, silica, and copper.
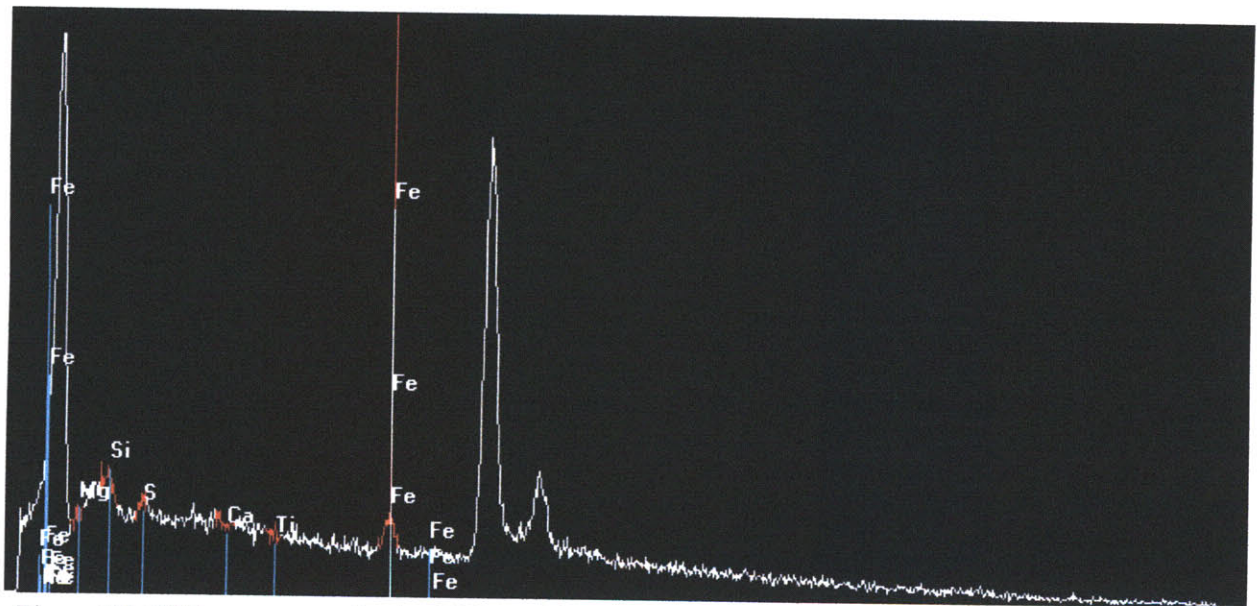
Figure 74. EDS spectrum of point 22.5.1 with characteristic iron peaks identified.
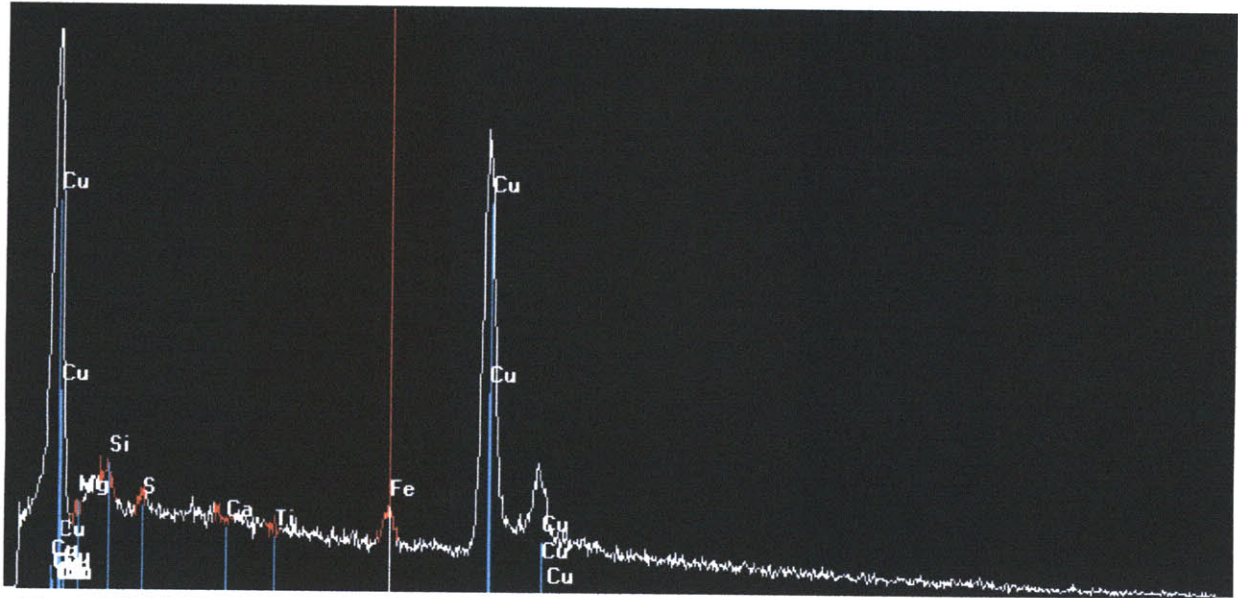
Figure 75. EDS spectrum for point 22.5.1 with characteristic copper peaks identified.
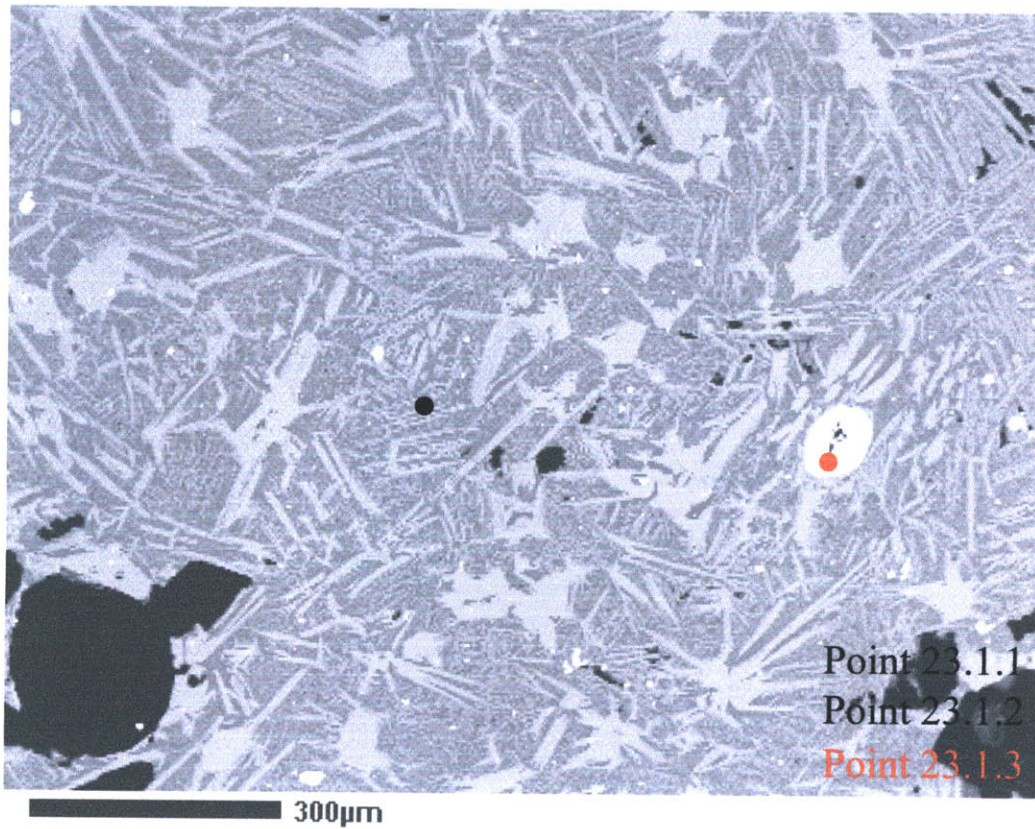
BSE spot23p1

Figure 76. Photomicrograph of Sample 23, frame 1. Silica-melt phase identified by black dot. Copper-iron-sulfide phase identified by red dot.
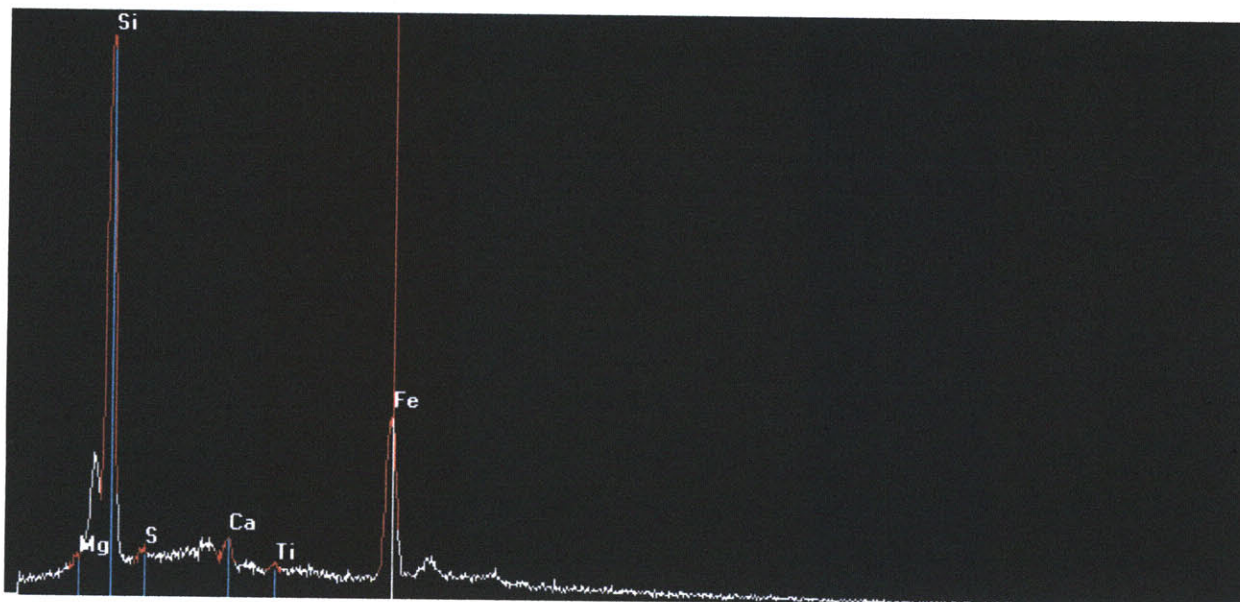
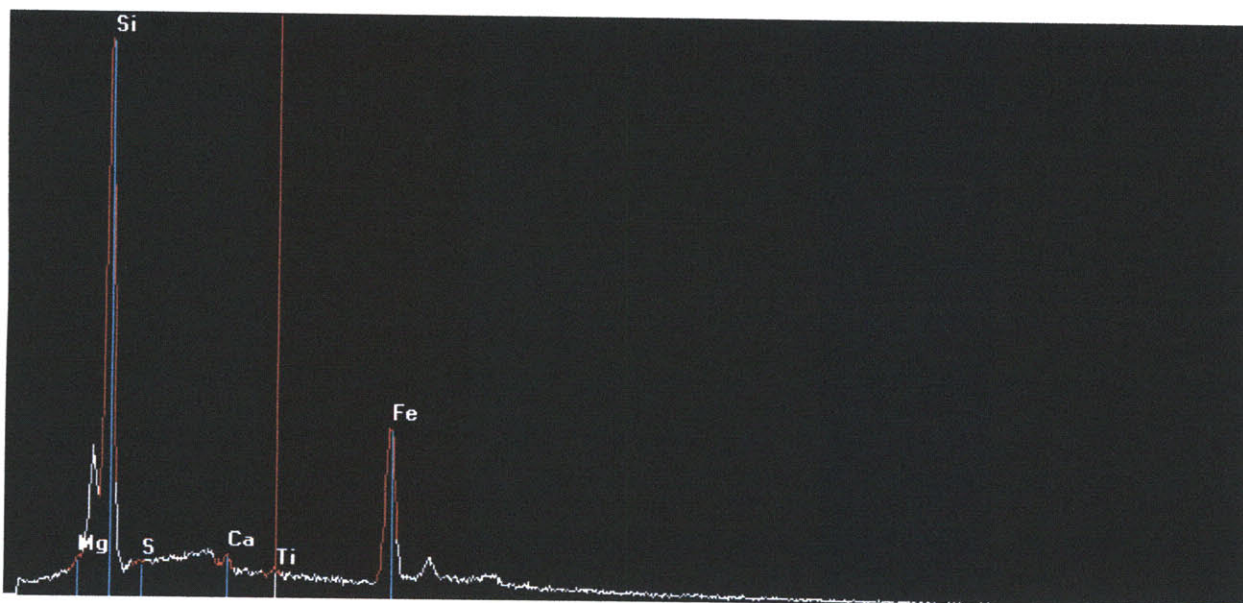Figure 77. EDS spectrum of point 23.1.1. Iron and silica are the main constituents.
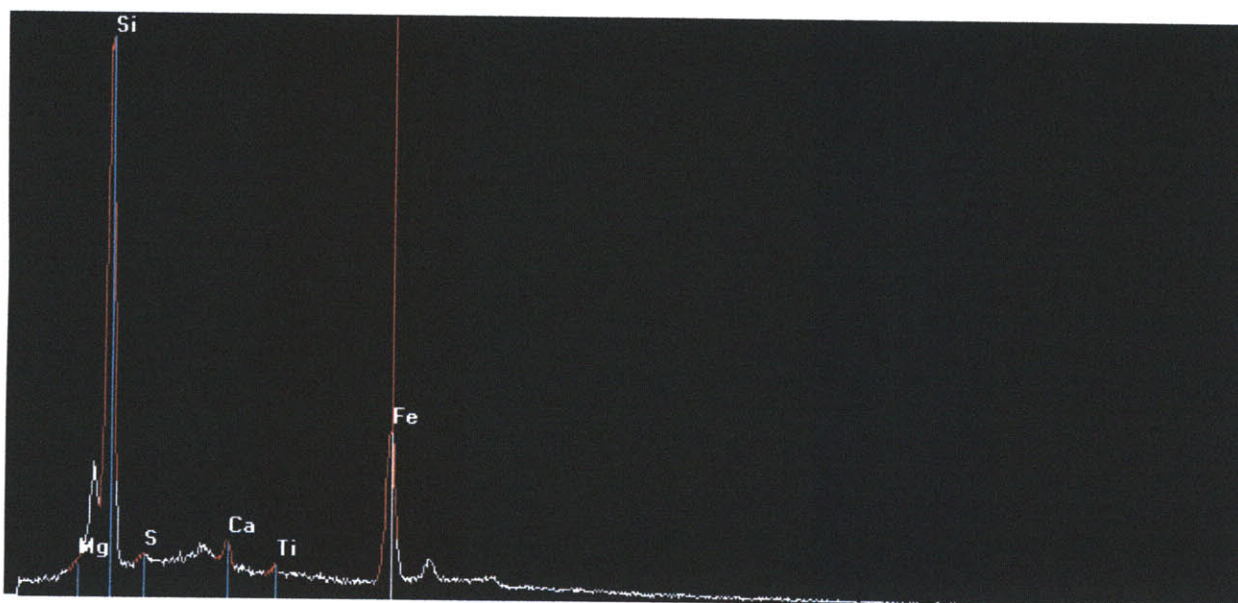
Figure 78. EDS spectrum of point 23.1.2. The main constituents are iron and silica.
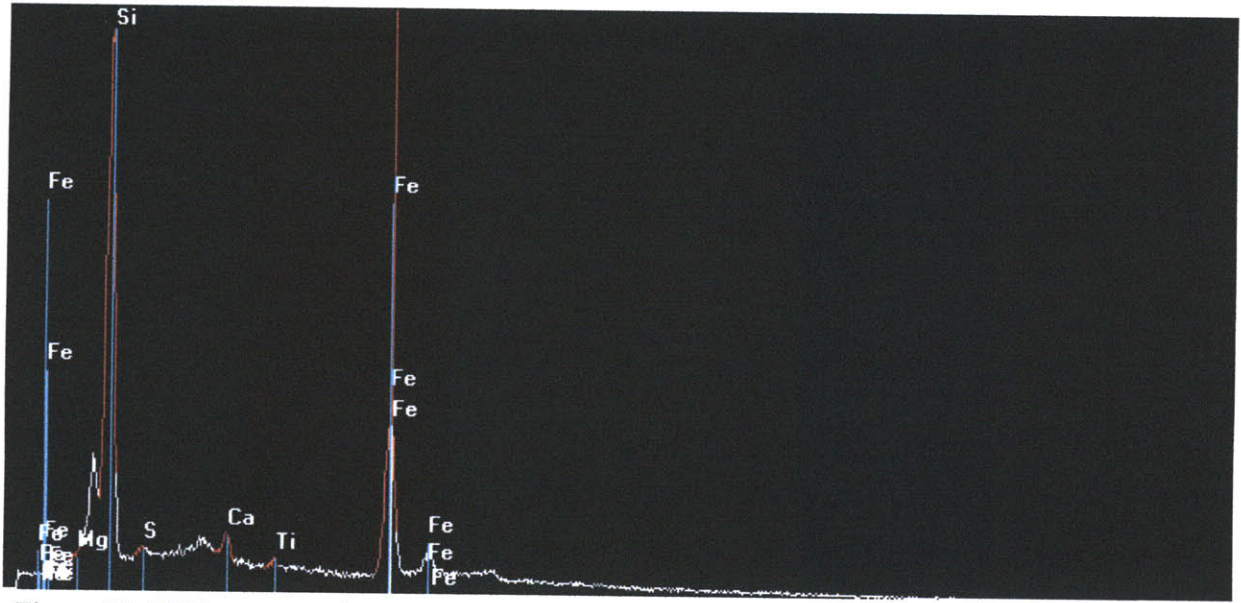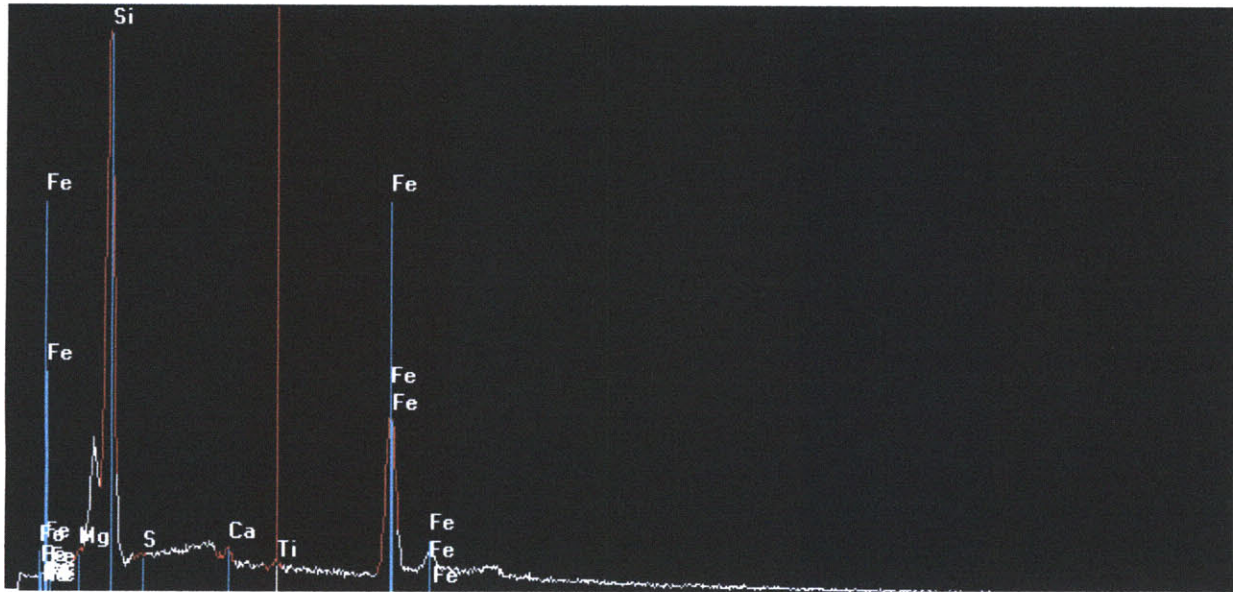
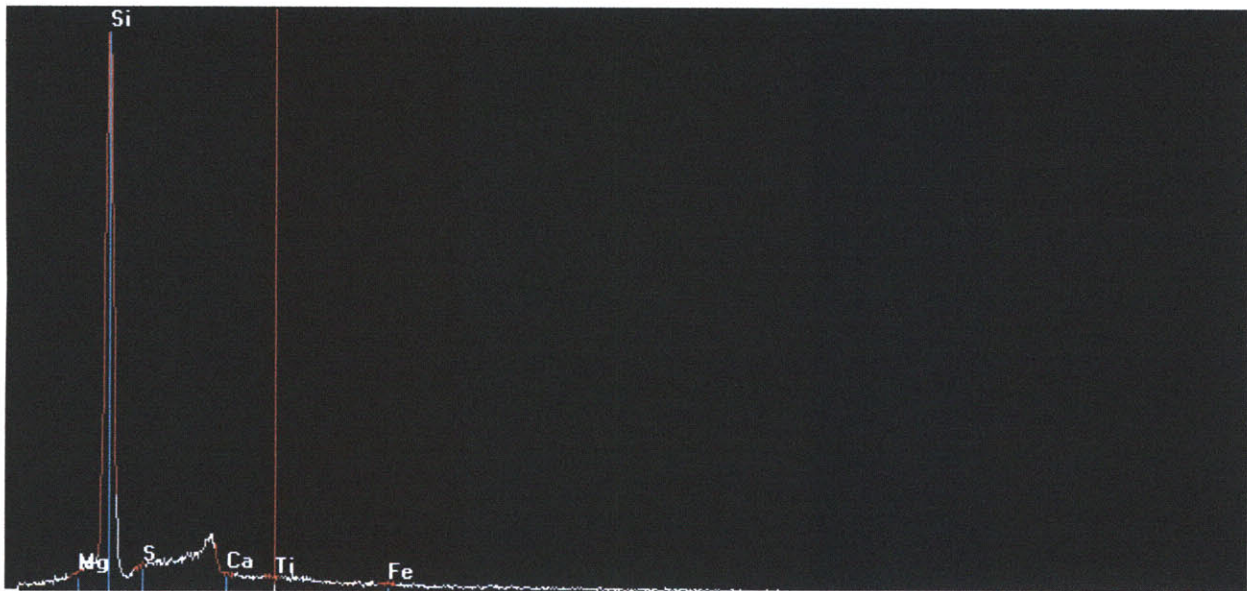Figure 79. EDS spectrum for point 23.1.2 with characteristic iron peaks identified.
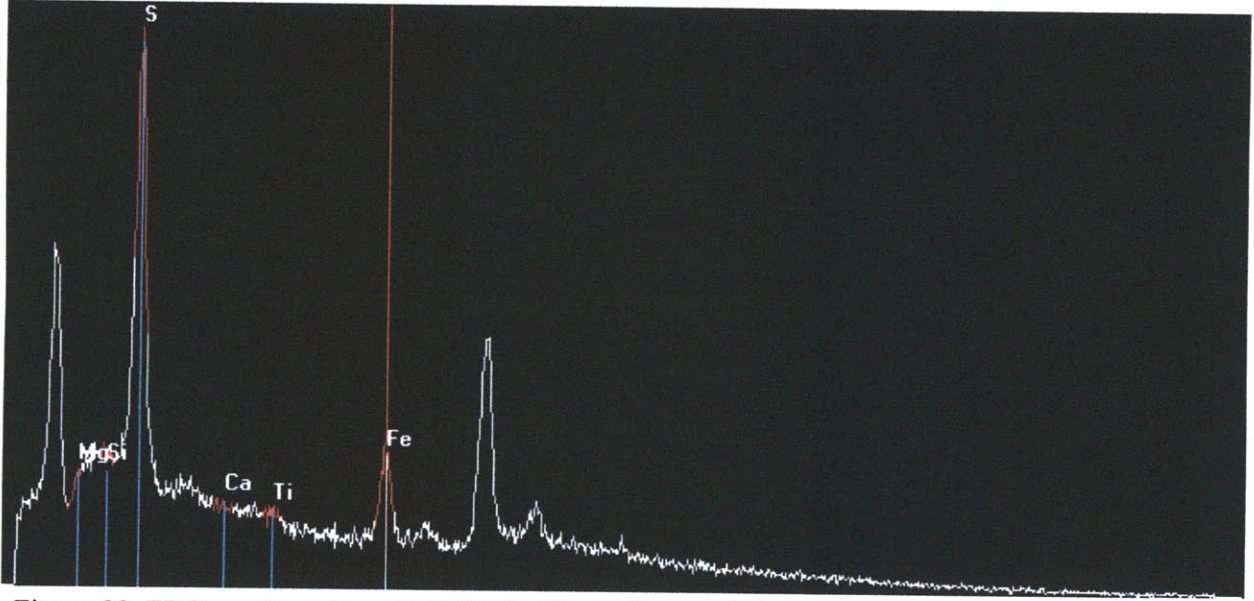
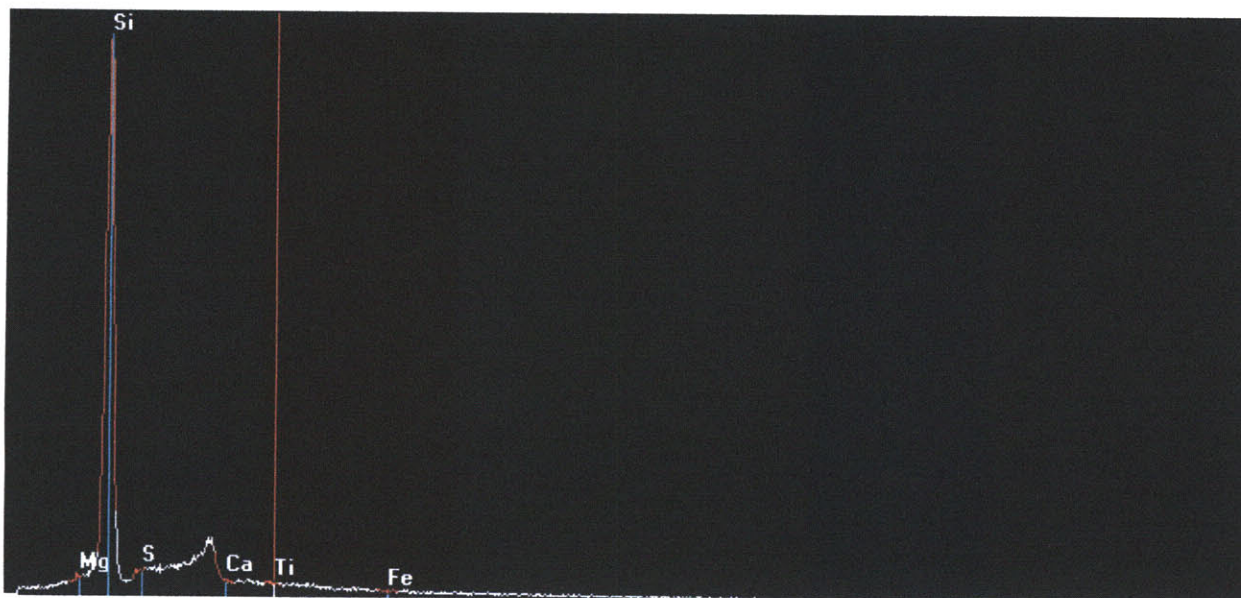Figure 80. EDS spectrum for point 23.1.3. The main constituents are iron, copper, and sulfur.

Figure 81. EDS spectrum for point 23.1.3 with characteristic iron peaks identified.
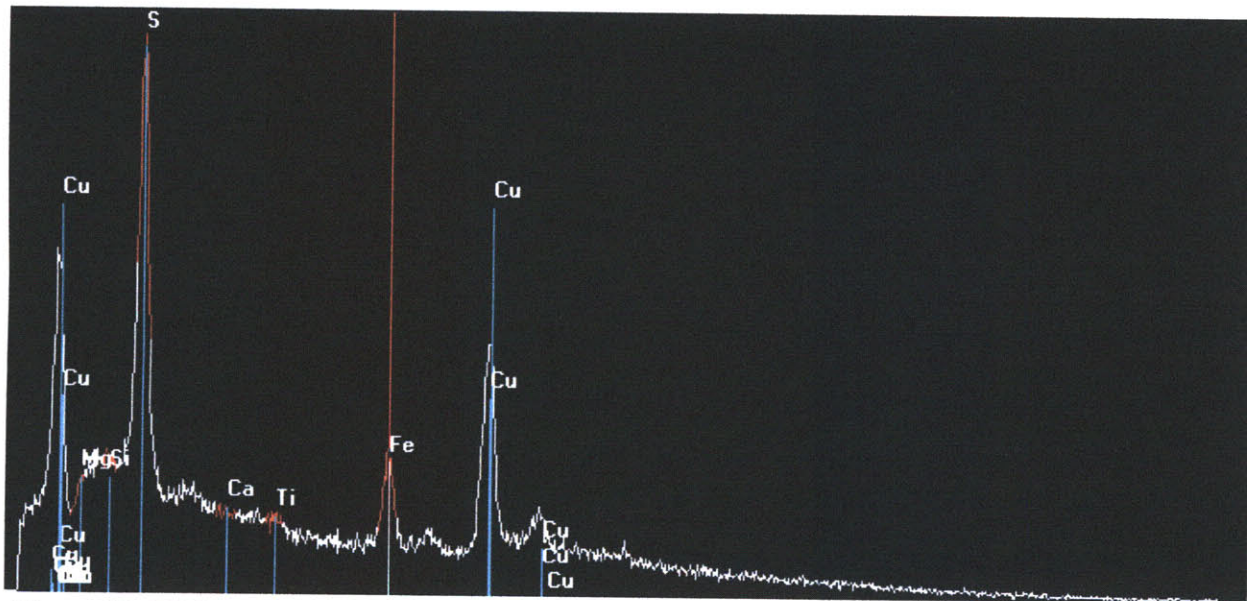
Figure 82. EDS spectrum of point 23.1.3 with characteristic copper peaks identified.

90

Point 23.2.1
Point 23.2.2
Point 23.2.3

300μm

BSE spot23p2

Figure 83. Photomicrograph of Sample 23, frame 2. Copper-iron-sulfide phase identified by black point. Quartz-like phase identified by blue point.

Figure 84. EDS spectrum of point 23.2.1. The major constituents are iron, sulfur, and copper.

Figure 85. EDS spectrum for point 23.2.1 with characteristic iron peaks identified.

Figure 86. EDS spectrum for point 23.2.1 with characteristic copper peaks identified.

Figure 87. EDS spectrum of point 23.2.2. The major constituent is silica.

Figure 88. EDS spectrum of point 23.2.3. The major constituent is silica.

BSE spot24p1
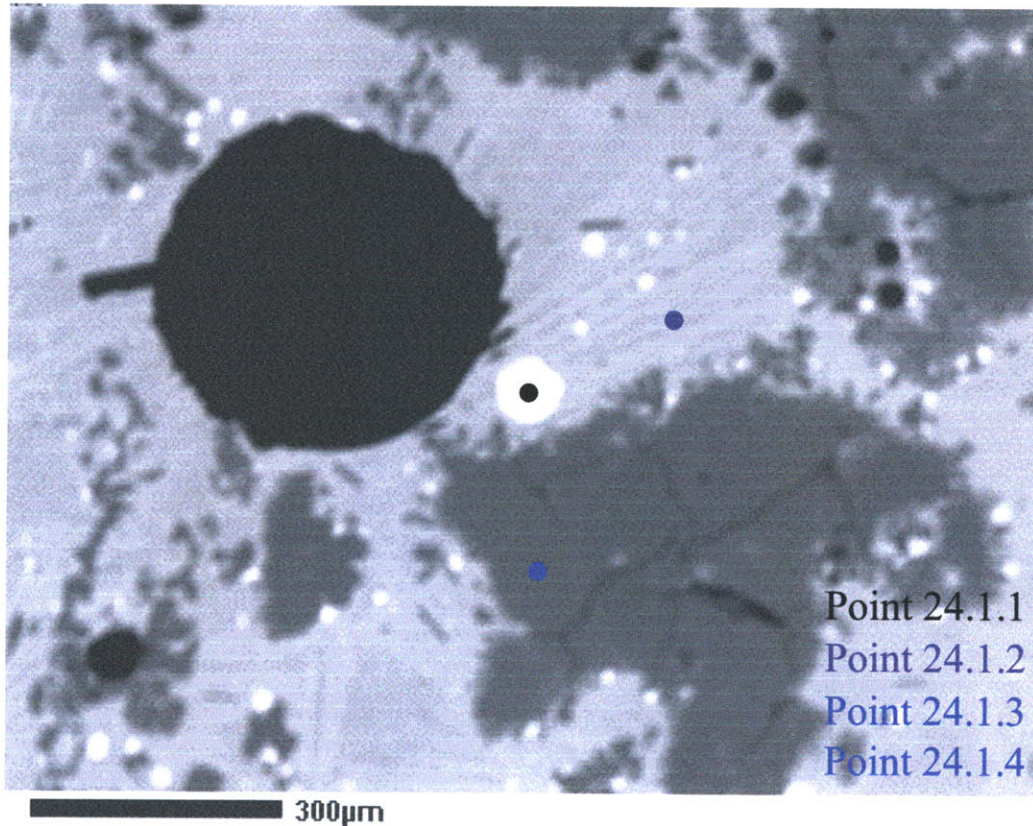
Figure 89. Photomicrograph of Sample 24, frame 1. Copper phase identified by black point. Silica-melt phase identified by purple point. Quartz-like phase identified by blue point.
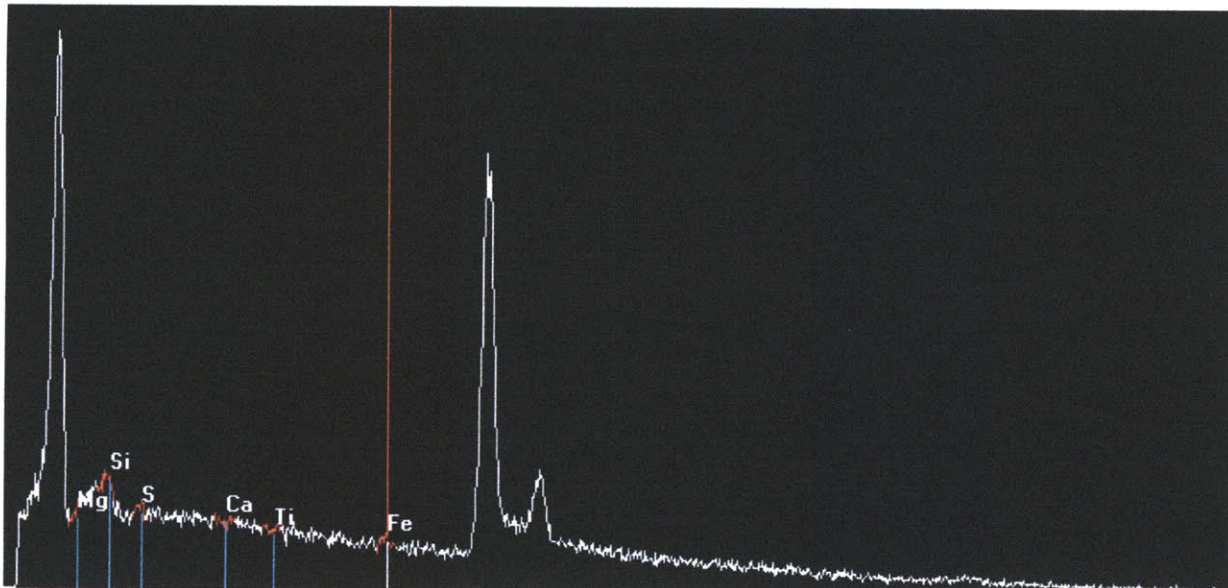
Figure 90. EDS spectrum of point 24.1.1. The main constituent is copper.
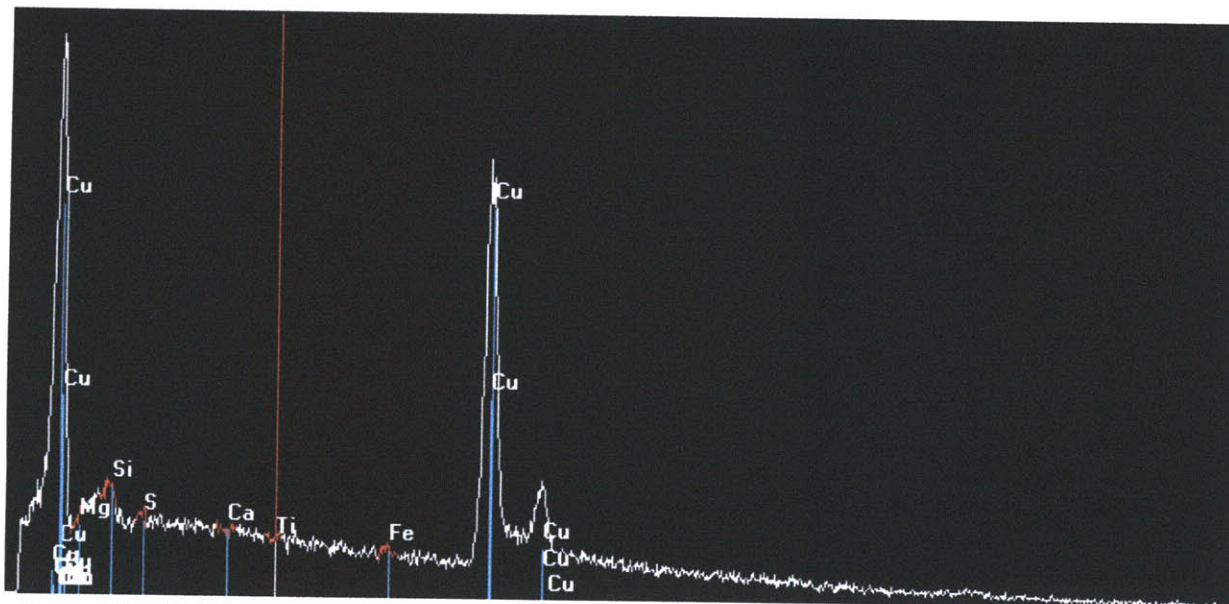
Figure 91. EDS spectrum for point 24.1.1 with characteristic copper peaks identified.

Figure 92. EDS spectrum of point 24.1.2. The major constituents are iron and silica.

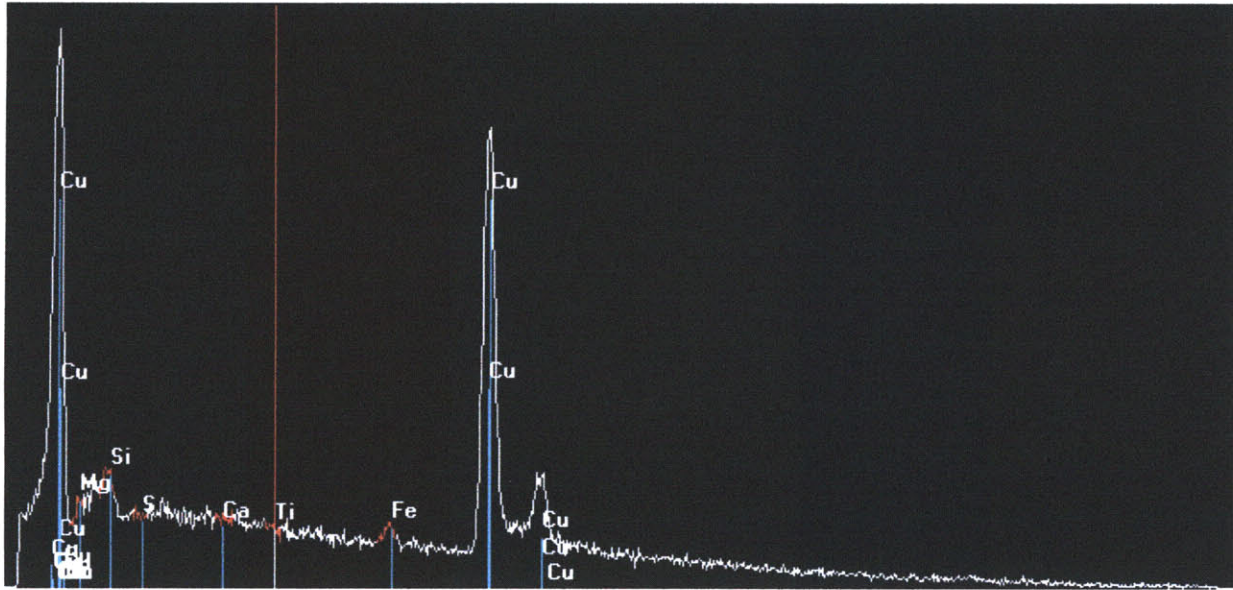Figure 93. EDS spectrum for point 24.1.2 with characteristic iron peaks identified.

Figure 94. EDS spectrum for point 24.1.3. The major constituent is silica.

Figure 95. EDS spectrum of point 24.1.4. The major constituent is silica.
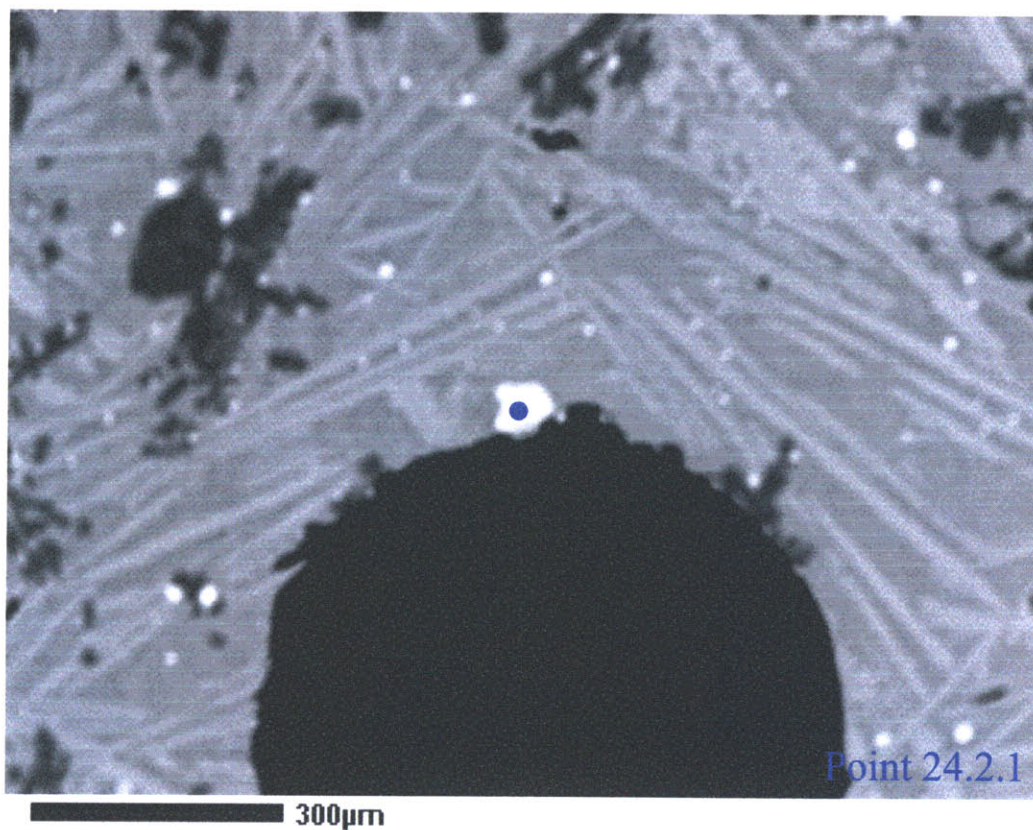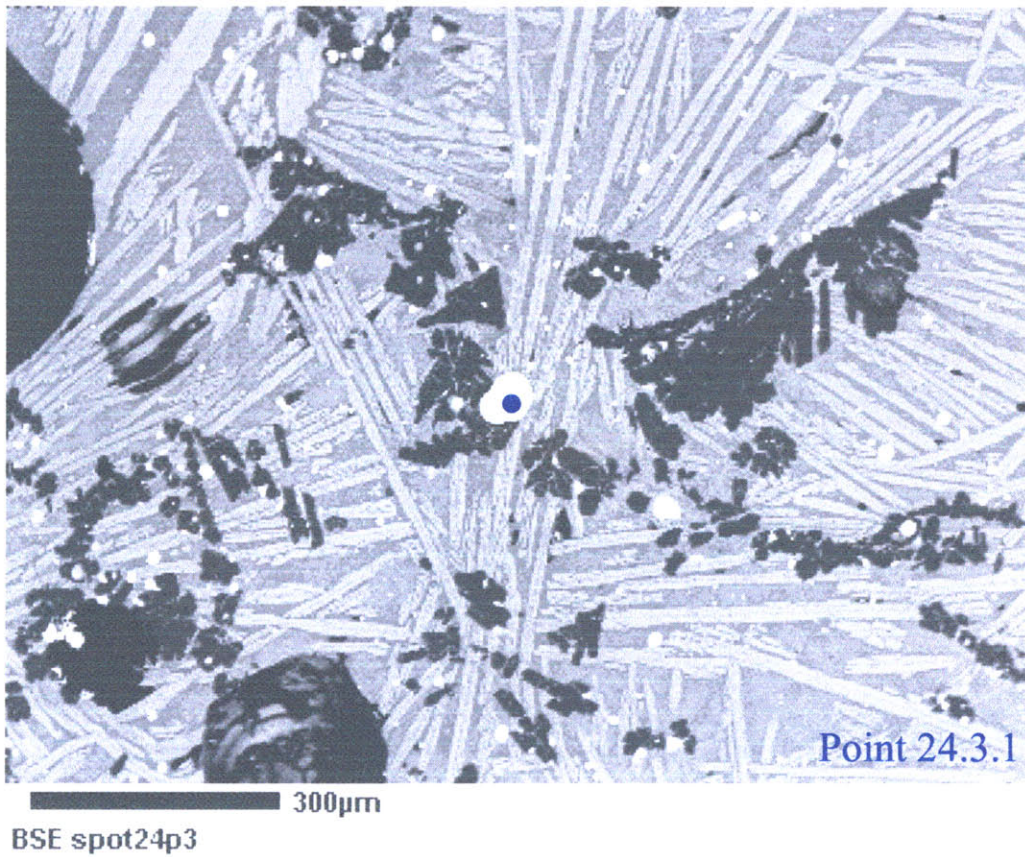

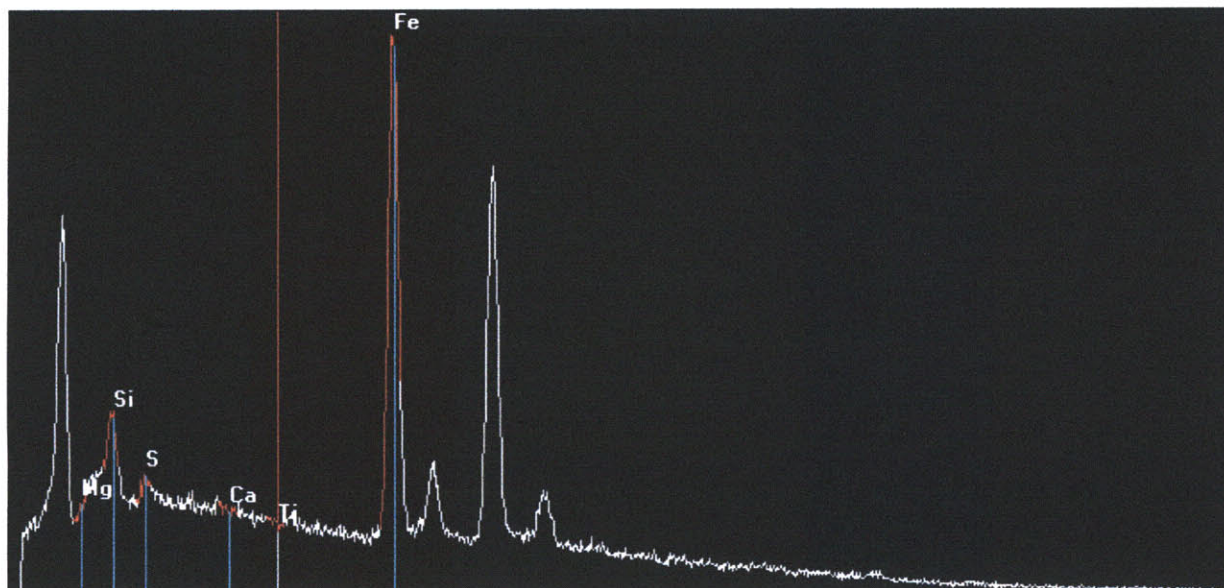Figure 96. Photomicrograph of Sample 24, frame 2. Copper-iron-sulfide phase identified by blue point.
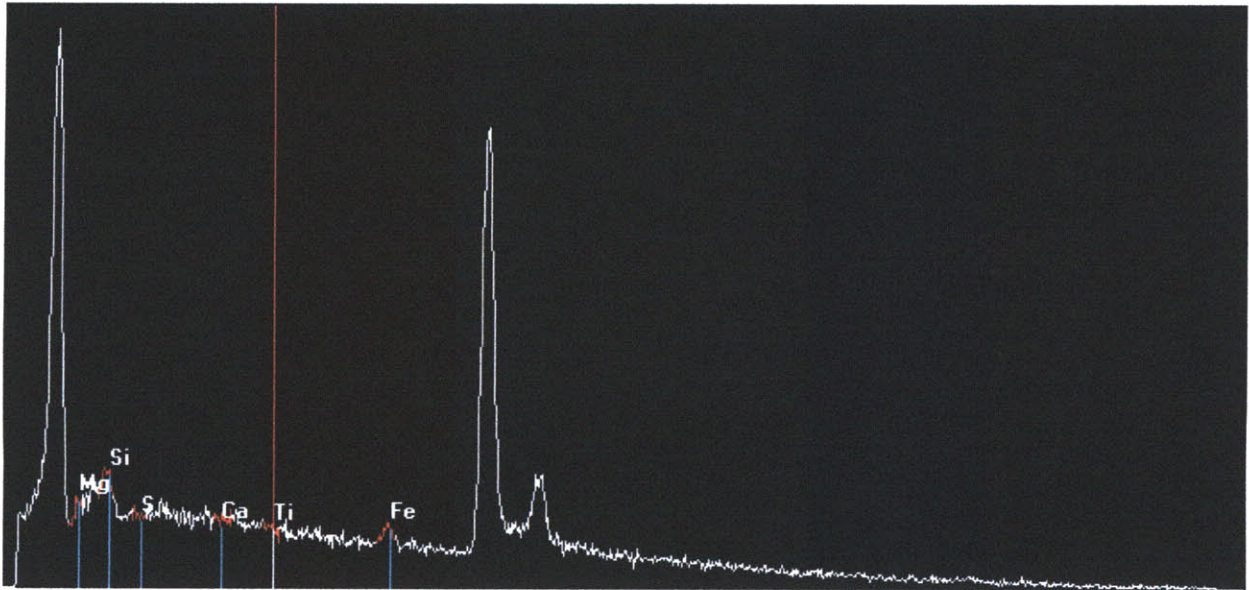
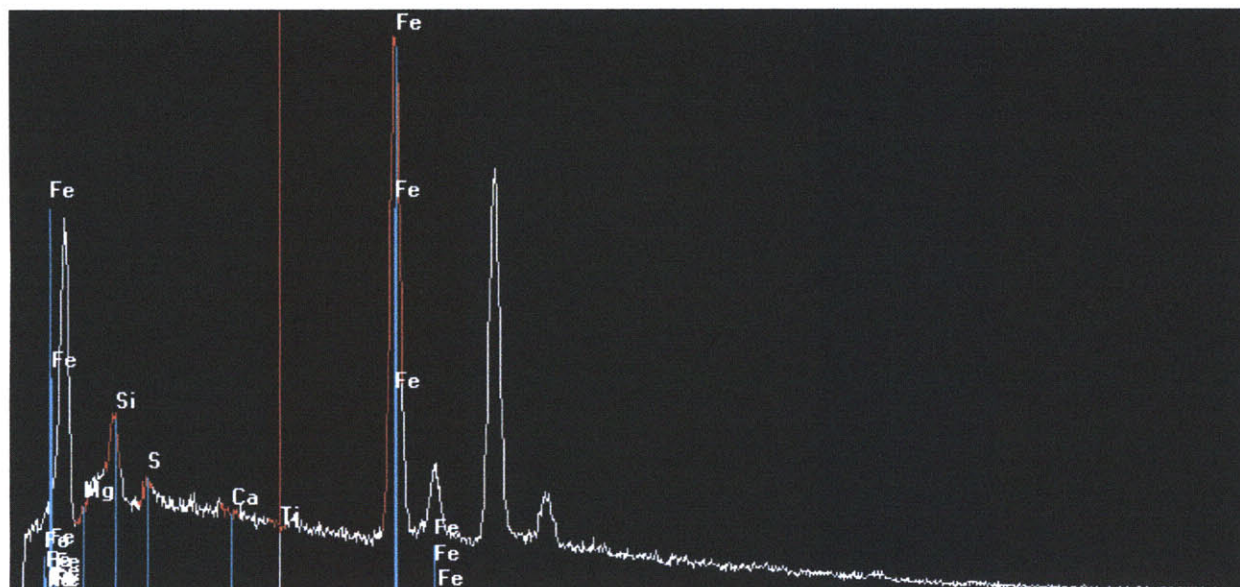Figure 97. EDS spectrum of point 24.2.1. The main constituents are iron, copper, and sulfur.
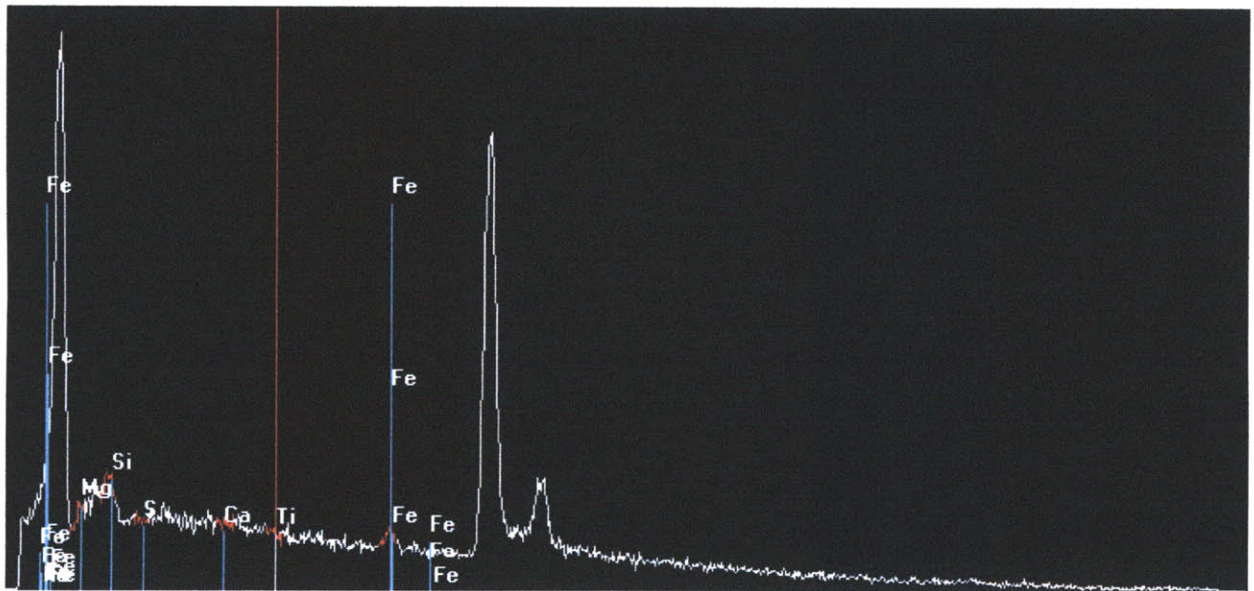
Figure 98. EDS spectrum for point 24.2.1 with characteristic iron peaks identified.

Figure 99. EDS spectrum for point 24.2.1 with characteristic copper peaks identified.

Figure 100. Photomicrograph of Sample 24, frame 3. Copper-iron-sulfide phase identified by blue point.

Figure 101. EDS spectrum for point 24.3.1. The major constituents are iron, copper, and sulfur.

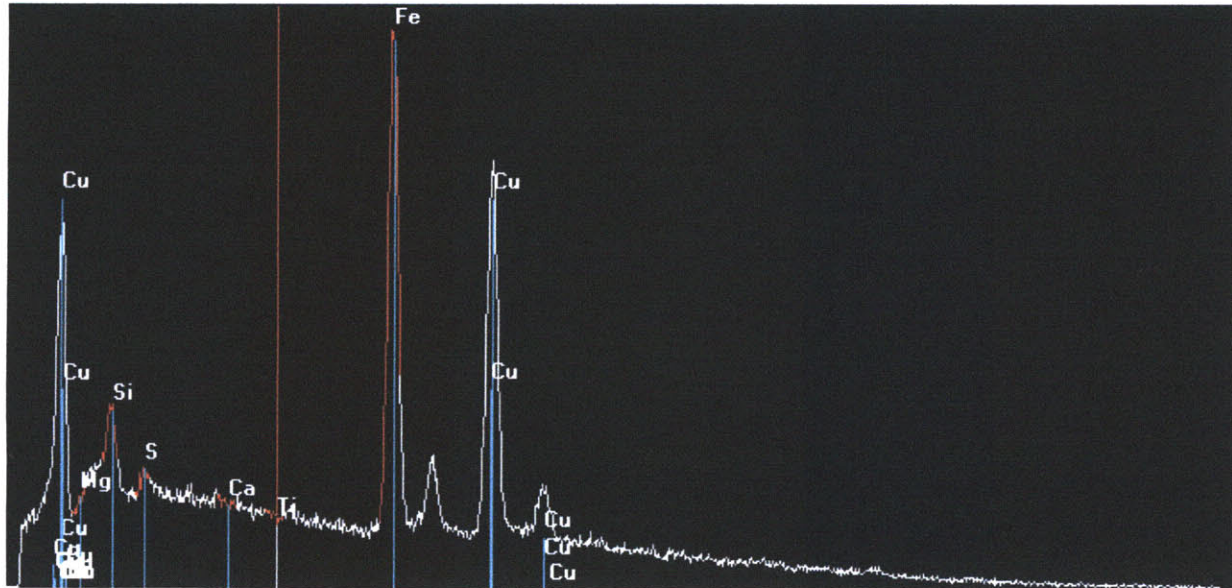Figure 102. EDS spectrum for point 24.3.1 with characteristic iron peaks identified.

Figure 103. EDS spectrum for point 24.3.1 with characteristic copper peaks identified.
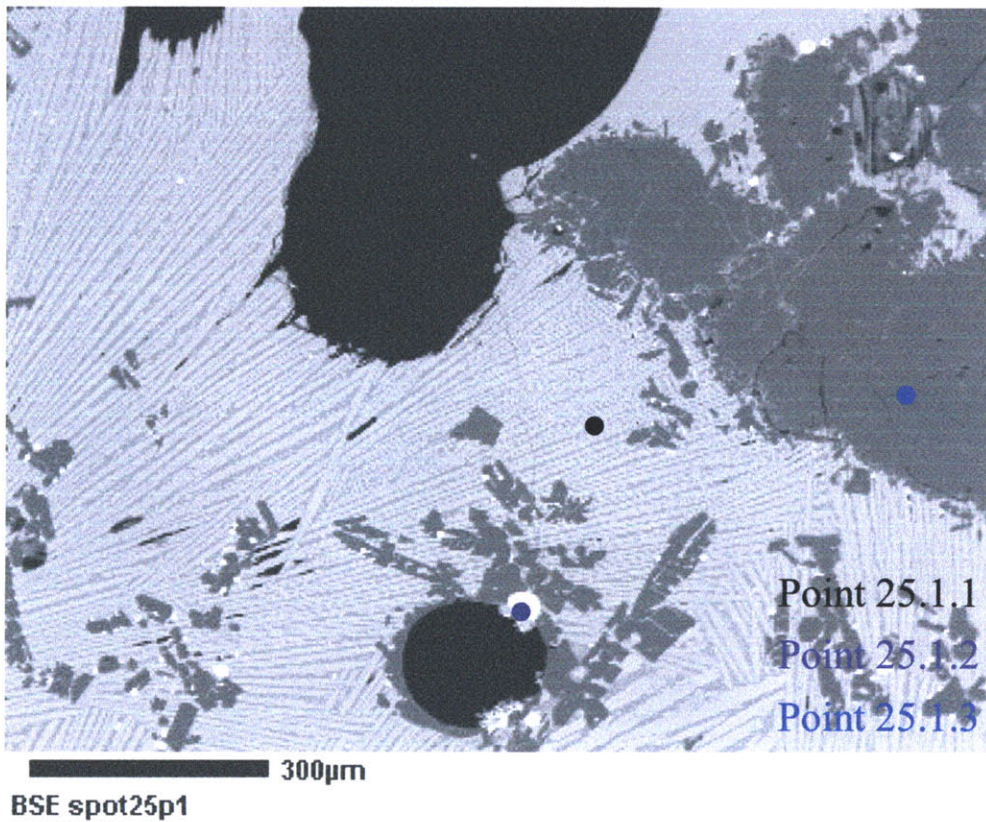

BSE spot25p1

Figure 104. Photomicrograph of Sample 25, frame 1. Silica-melt phase identified by the black point. Copper phase identified by the purple point. Quartz-like phase identified by the blue point.
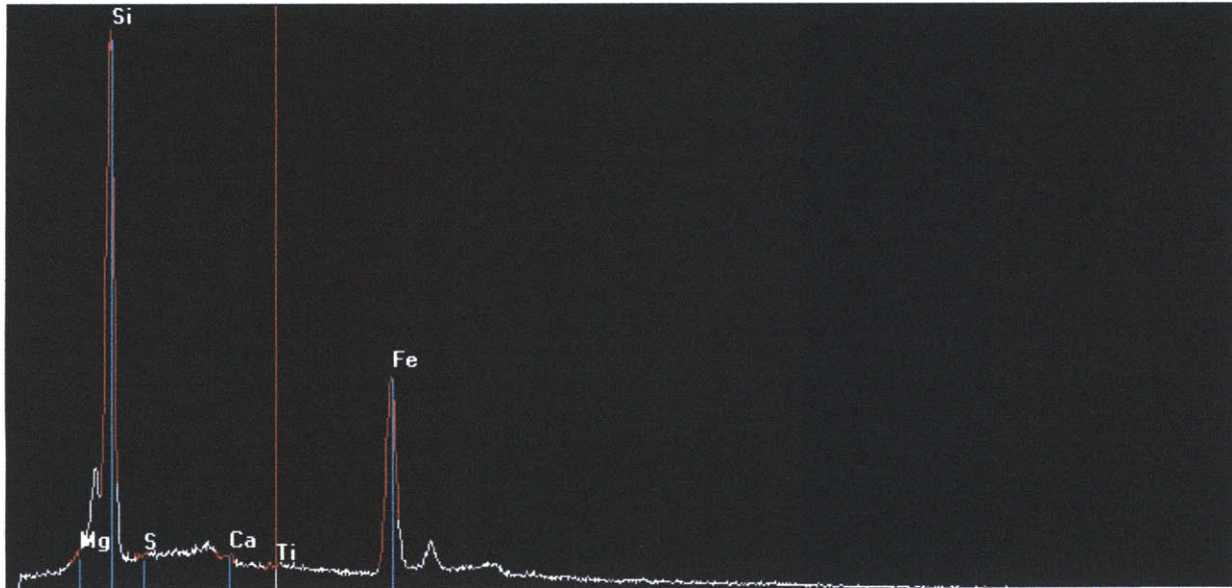
Figure 105. EDS spectrum of point 25.1.1. The major constituents are silica and iron.
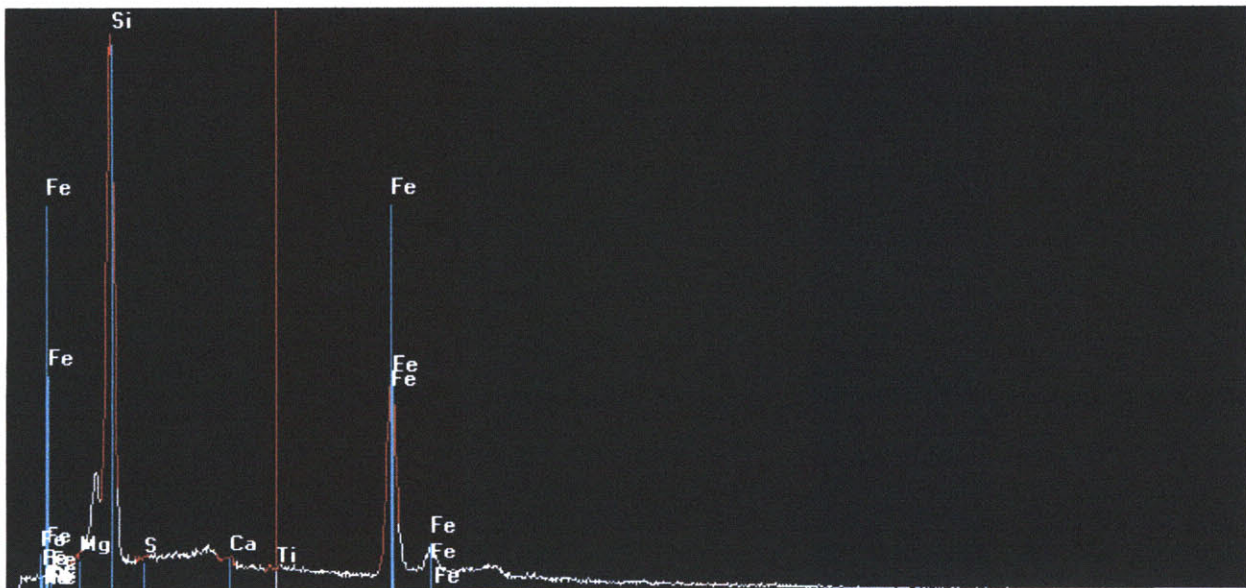

Figure 106. EDS spectrum for point 25.1.1 with characteristic iron peaks identified.
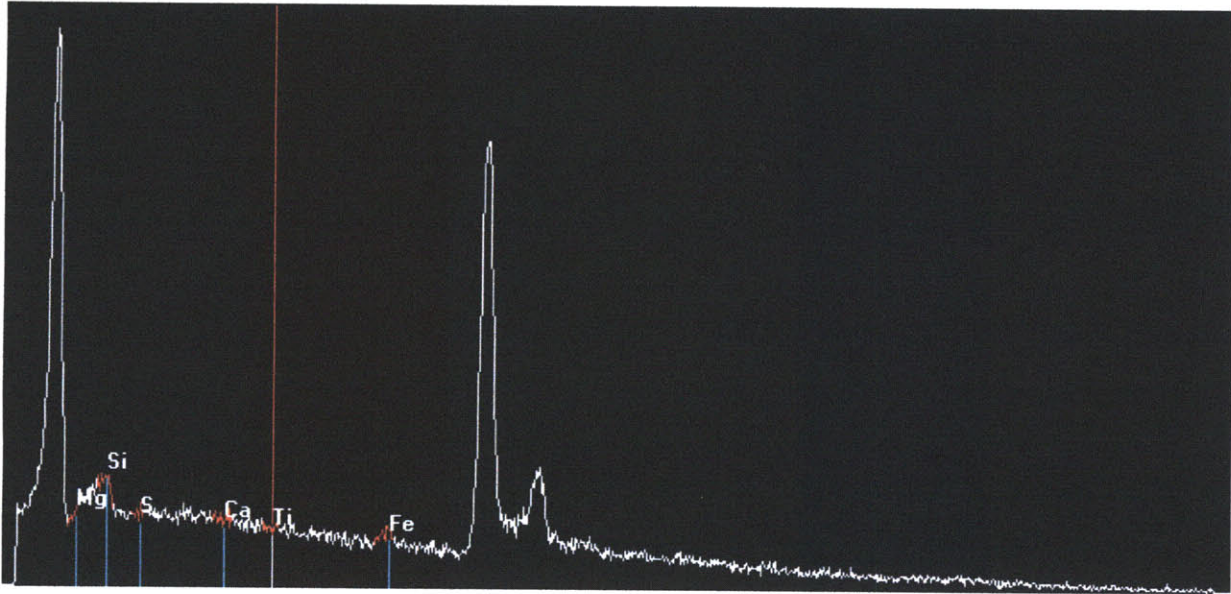
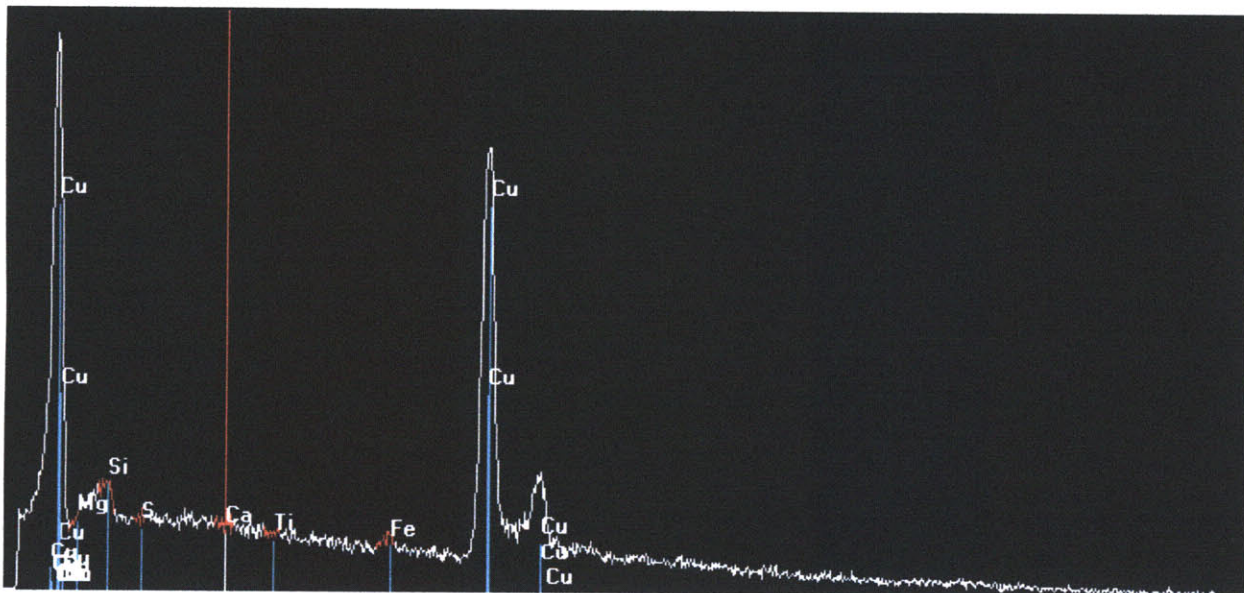Figure 107. EDS spectrum for point 25.1.2. The main constituent is copper.

Figure 108. EDS spectrum of 25.1.2 with characteristic copper peaks identified.
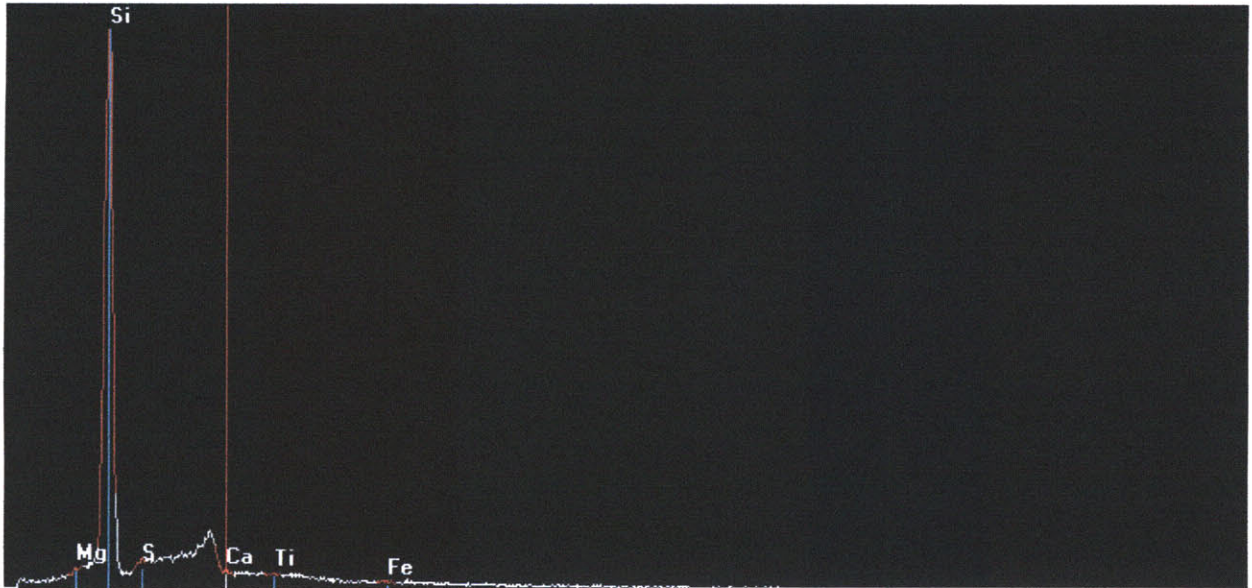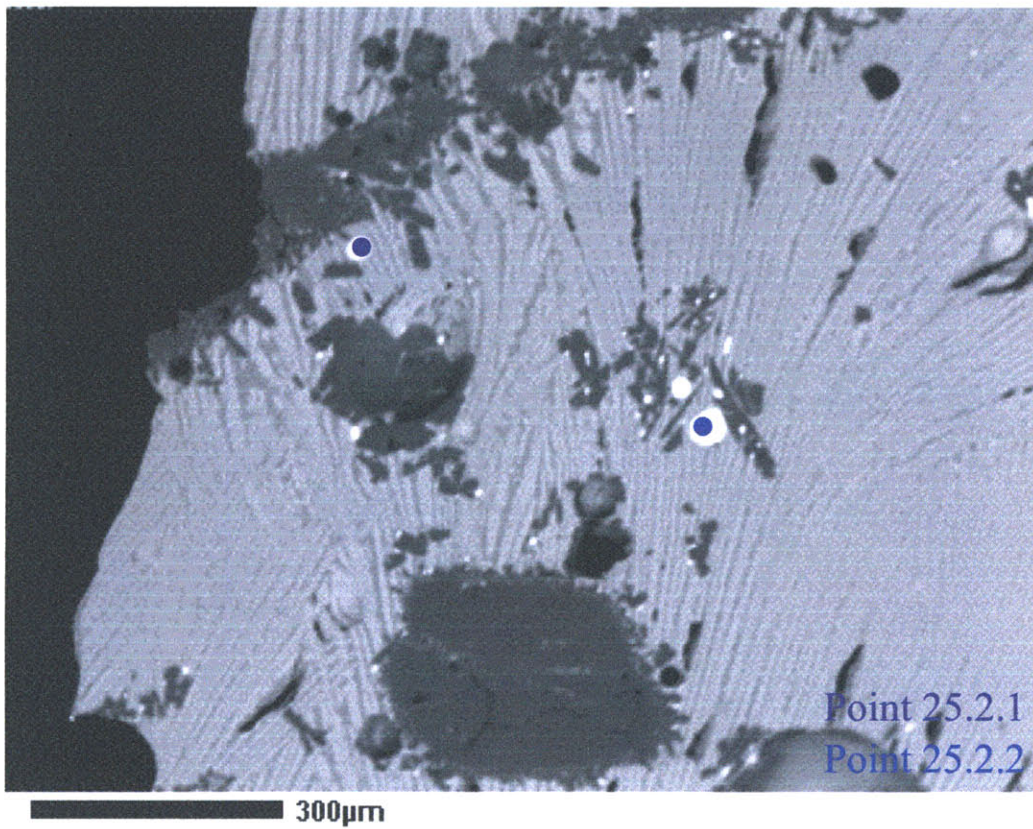
Figure 109. EDS spectrum for point 25.1.3. The main constituent is silica.

BSE spot25p2

Figure 110. Photomicrograph of Sample 25, frame 2. Copper-iron-sulfide phase identified by purple point. Copper phase identified by blue point.

Figure 111. EDS spectrum for point 25.2.1. The major constituents are copper, iron, and sulfur.

Figure 112. EDS spectrum for point 25.2.1 with characteristic iron peaks identified.

Figure 113. EDS spectrum for point 25.2.1 with characteristic copper peaks identified
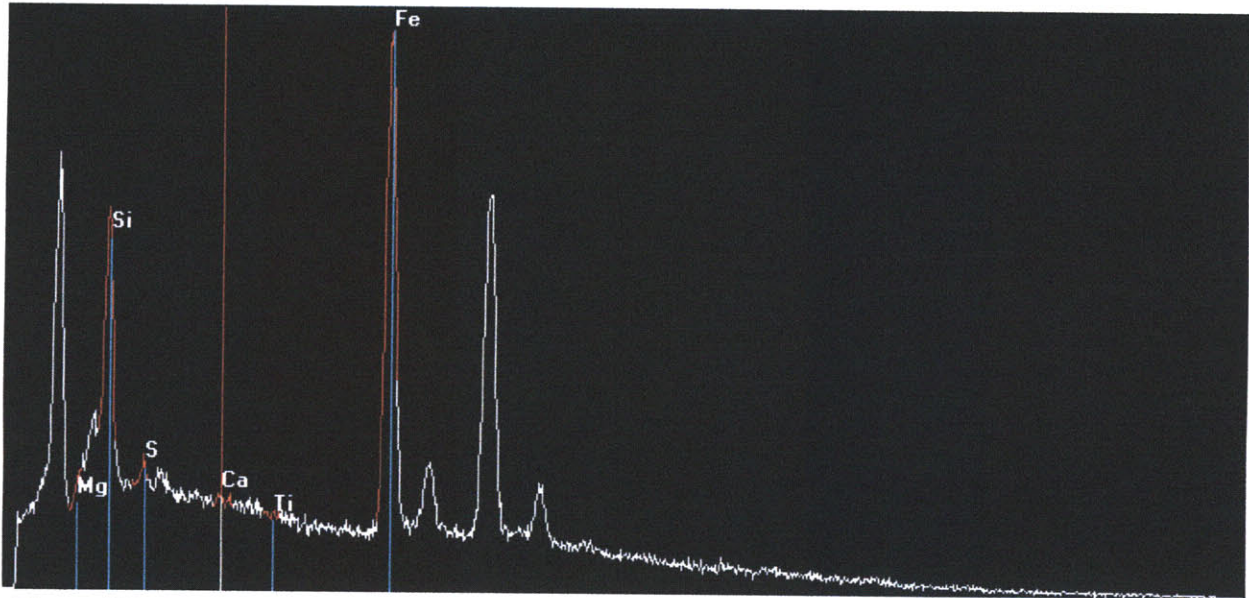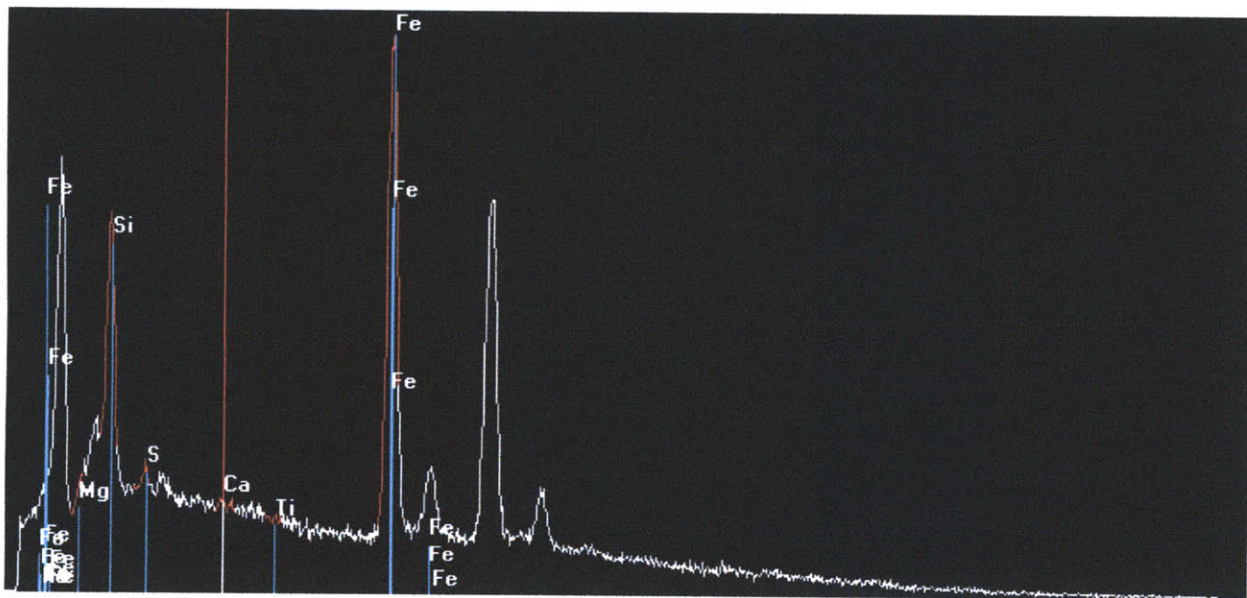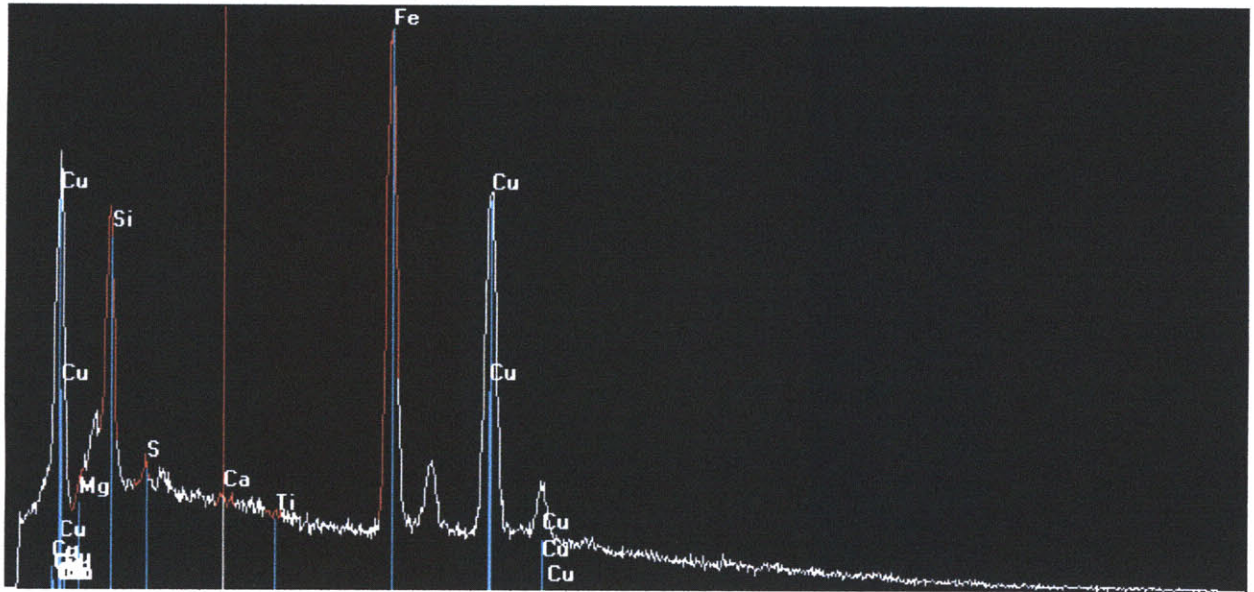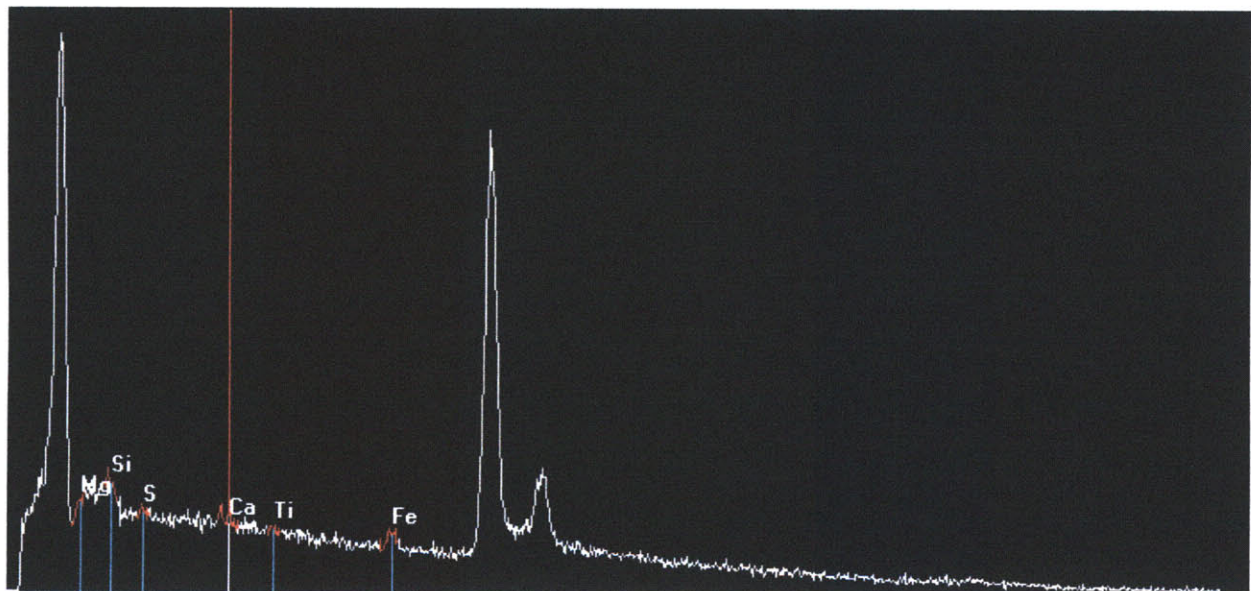
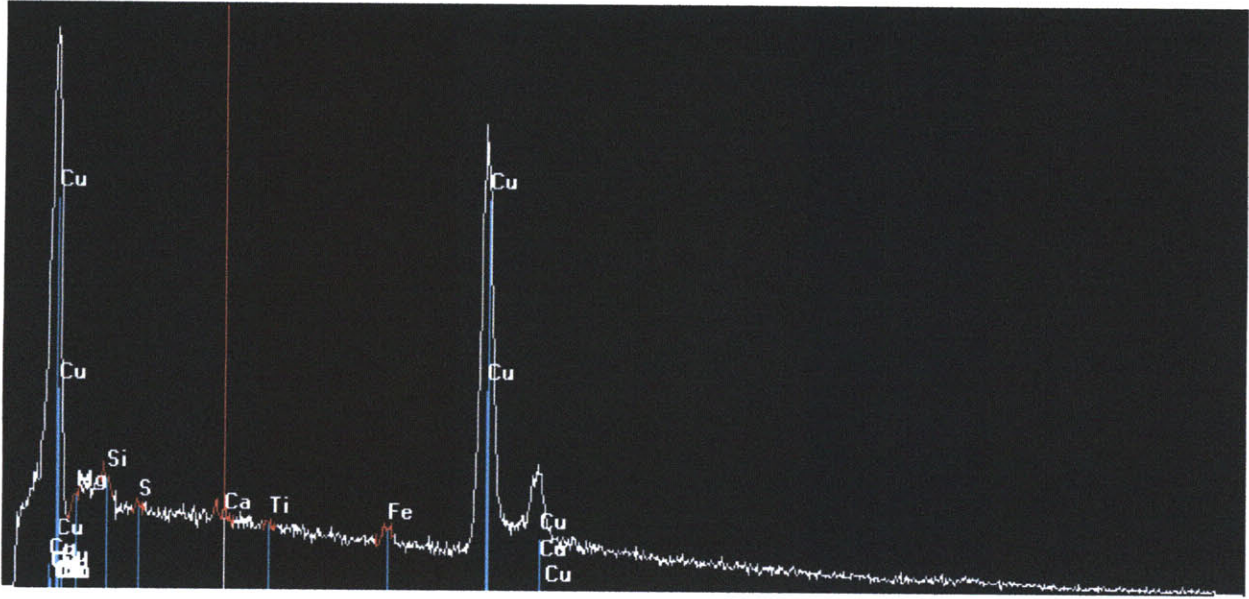Figure 114. EDS spectrum for point 25.2.2. The main constituent is copper.

Figure 115. EDS spectrum for point 25.2.2 with characteristic copper peaks identified.

Acknowledgements

I would like to thank first and foremost my thesis advisor, Professor Dorothy Hosler (DMSE/MIT) for giving me the opportunity to work on this project and arranging for me to carry out research at the Woods Hole Oceanographic Institute (WHOI). The idea of using the uranium series for dating archaeological slags was suggested to Prof. Hosler by Dr. Andrew Macfarlane (Department of Earth Science/Florida International University).
I would also like to thank Dr. Kenneth Sims (Geology & Geophysics/WHOI), my direct supervisor at WHOI.

I would like to thank Prof. Heather Lechtman (DMSE/MIT) and Dr. Sidney Carter (CMRAE/MIT) for editorial suggestions during the writing process.

<div align="center">I would also like to thank</div>

Dr. Nilanjan Chatterjee (EAPS/MIT)

Dr. Glenn Gaetani (Geol. & Geophys./WHOI)

Dr. Nobumichi Shimizu (Geol. & Geophys./WHOI)

Dr. Bernhard Peucker-Ehrenbrink (Geol. & Geophys./WHOI)

Mr. Jerzy Blusztajn (Plasma Mass Spectrometer Facility/WHOI)

Ms. Jennifer Meanwell (DMSE-CMRAE/MIT)

<div align="center">and</div>

Mr. Christian Miller (Geol. & Geophys./WHOI)

Ms. Hannah Reitzel (DMSE/MIT)

Mr. Christopher Waters (Geol. & Geophys./WHOI)

Ms. Evelyn Mervine (Geol. & Geophys./WHOI)

Ms. Malima Wolf (Mechanical Engineering/MIT)

I would like the Undergraduate Research Opportunities Program for financial support during the summer of 2007.

References Cited

Bachmann, Hans-Gert
    1982   *The Identification of Slags from Archaeological Sites*. The Institute of
            Archaeology, Occasional Publication No. 6, London, England.

Cooper, Kari M., Steven J. Goldstein, Kenneth W.W. Sims, and Michael T. Murrell
    2003   Uranium-series chronology of Gorda Ridge volcanism: new evidence from the
            1996 erruption. Earth and Planetary Science Letters 206, No. 3: 459-475.

Faure, Gunter and Teresa M. Mensing
    2005   *Isotopes Principles and Applications*. 3rd Ed. John Wiley & Sons, Inc., Hoboken,
            New Jersey.

Hedman, Matthew
    2007   *The Age of Everything: How Science Explores the Past*. The University of
            Chicago Press, Chicago, IL.

Hosler, Dorothy
    2004   Nuevos datos sobre la producción del metal en el occidente en la época
            prehispánica. *Bienes Regionales del antiguo Occidente de México: Producción y
            Intercambio*. Colegio de Michoacán, pp. 335-354.
    2003a "Metal Production," Chapter 21 in *The Postclassic Mesoamerican World*.
            University of Utah Press: 159–171.
    2003b Nuevos hallazgos sobre la metalurgia antigua de Guerrero. *El Pasado
            Arqueológico de Guerrero*. Instituto Nacional de Antropologiá y Historia.
            México D.F., pp. 225-241.
    1994   *The Sounds and Colors of Power: The Sacred Metallurgical Technology of
            Ancient West Mexico*. MIT Press, Cambridge, MA.
    1988a Ancient West Mexican Metallurgy: A Technological Chronology. *Journal of
            Field Archaeology* 15, No. 2: 91-217.
    1988b Ancient West Mexican Metallurgy: South and Central American Origins and
            West Mexican Transformations. *American Anthropologist* 90, No. 4: 32-855.

Ivanovich, M. and R.S. Harmon, eds.
    1982   *Uranium Series Disequilibrium : Applications to Environmental Problems*.
            Clarendon Press, Oxford, UK.

Sharp, Rachel
    2001   *Analysis of Copper Slags from the Archaeological Site of El Manchon, Guerrero,
            Mexico*. Bachelor of Science Thesis, Massachusetts Institute of Technology.